NTNU

Norwegian University of
Science and Technology

# The Effects of Numerical Modeling Assumptions in Seismic Design

Jørgen Rosmo Roven

Master of Science in Civil and Environmental Engineering
Submission date: June 2018
Supervisor: Amir Kaynia, KT
Co-supervisor: Emrah Erduran, Rambøll

Norwegian University of Science and Technology
Department of Structural Engineering

**Department of Structural Engineering**
Faculty of Engineering
**NTNU- Norwegian University of Science and Technology**

ACCESSIBILITY

Open

# MASTER THESIS 2018

| SUBJECT AREA: Computational Mechanics | DATE: 17.06.2018 | NO. OF PAGES: 143 |
|---|---|---|

TITLE:
**The Effects of Numerical Modeling Assumptions in Seismic Design**

Effekten av Modelleringsantagelser i Seismisk Design

BY:

Jørgen Rosmo Roven

SUMMARY:
Complex numerical models have been developed during the last decades. They are able to model complex phenomena that may occur in a structure when subjected to seismic excitations, including nonlinear material response and the effects of localization. Correct calibration of the numerical model is essential in order to take advantage of new methods of analysis. As the models become more complex, more knowledge is required to make the right assumptions. These assumptions have a large impact on the end results of analyses, which can lead to inaccurate assessment of damage.

The objective of this work was to investigate the effect of modeling assumptions. This has been achieved through analysis of a reinforced concrete moment resisting frame. Both nonlinear time-history analysis (NTHA) and static pushover analysis (SPO) have been performed, as these methods complement each other. Different model configurations have been used for these analyses to investigate the effect of their differences. The analyzed structure is a low-rise building with a high degree of regularity, which legitimize an analysis of one of its substructures. Hence, all analyses have been carried out on a 2D frame. Distributed inelasticity elements with fiber sections and complex material models were used. Results from models using both stiffness and flexibility based beam-column elements were compared. Along with these models, the novel beam with hinges (BwH) beam-column element model was used. The OpenSees framework was used as it posses the necessary capabilities for this kind of study.

Both global and local responses were assessed. The results showed that the modeling
assumptions do have a significant impact on the response. This was observed on both global and local levels. The resulting response histories of the roof drifts showed that for the force based (FB) elements, when more integration points (IP) were used, the response histories approached a stable solution. The same could be seen in the inter-story drift ratio (IDR) profiles sampled when maximum roof drifts occurred. For the BwH model, varying the hinge lengths resulted in different response histories with sometimes extreme variations. Importantly, significant differences in the curvature response, which is an important measure of damage, were also observed for different model configurations.

Among the conclusions drawn from these results, is that six or more IPs should be used for flexibility based element models when they are being used in a NTHA. Also, it is clear that measured curvatures are highly sensitive to modeling assumptions. So much in fact, that assumptions resulting mildly imprecise models may lead to unfortunate assessment of damage. The results show that attention to detail is important when a numerical model is to be constructed and that the analyst must have knowledge of the numerical issues that may arise in order to arrive at a correct assessment. Further work is necessary to quantify the effects of modeling assumptions.

RESPONSIBLE TEACHER: Amir M. Kaynia

SUPERVISOR(S): Emrah Erduran

CARRIED OUT AT: NTNU, KT

# Preface

This master thesis entitled «The Effects of Numerical Modeling Assumptions in Seismic Design» is written during the spring of 2018 at the Department of Structural Engineering, Norwegian University of Science and Technology (NTNU). The work finalizes the 2-year Master's degree program Civil and Environmental Engineering. The work is a collaboration project between NTNU and Rambøll, Oslo. It builds on work by Nina Øystad-Larsen (Rambøll) and others. Supervision has been given primarily by Emrah Erduran (Rambøll).

Trondheim, June 2018
Jørgen Rosmo Roven

# Acknowledgement

Acknowledgements are directed towards my supervisors Emrah Erduran [1] and Amir M. Kaynia [2] for their guidance. I want to thank Nina Øystad-Larsen [3] whose help resulted in insight in important concepts as well as knowledge of possible pitfalls associated with OpenSees.

A special thanks is directed towards Emrah Erduran. His interest, helpful remarks and knowledge on the subject has been tremendously helpful.

[1] Rambøll, Oslo
[2] Department of Structural Engineering, NTNU, Trondheim
[3] Rambøll, Oslo

# Abstract

Complex numerical models have been developed during the last decades. They are able to model complex phenomena that may occur in a structure when subjected to seismic excitations, including nonlinear material response and the effects of localization. Correct calibration of the numerical model is essential in order to take advantage of new methods of analysis. As the models become more complex, more knowledge is required to make the right assumptions. These assumptions have a large impact on the end results of analyses, which can lead to inaccurate assessment of damage.

The objective of this work was to investigate the effect of modeling assumptions. This has been achieved through analysis of a reinforced concrete moment resisting frame. Both nonlinear time-history analysis (NTHA) and static pushover analysis (SPO) have been performed, as these methods complement each other. Different model configurations have been used for these analyses to investigate the effect of their differences. The analyzed structure is a low-rise building with a high degree of regularity, which legitimize an analysis of one of its substructures. Hence, all analyses have been carried out on a 2D frame. Distributed inelasticity elements with fiber sections and complex material models were used. Results from models using both stiffness and flexibility based beam-column elements were compared. Along with these models, the novel beam with hinges (BwH) beam-column element model was used. The OpenSees framework was used as it posses the necessary capabilities for this kind of study.

Both global and local responses were assessed. The results showed that the modeling assumptions do have a significant impact on the response. This was observed on both global and local levels. The resulting response histories of the roof drifts showed that for the force based (FB) elements, when more integration points (IP) were used, the response histories approached a stable solution. The same could be seen in the inter-story drift ratio (IDR) profiles sampled when maximum roof drifts occurred. For the BwH model, varying the hinge lengths resulted in different response histories with sometimes extreme variations. Importantly, significant differences in the curvature response, which is an important measure of damage, were also observed for different model configurations.

Among the conclusions drawn from these results, is that six or more IPs should be used for flexibility based element models when they are being used in a NTHA. Also, it is clear that measured curvatures are highly sensitive to modeling assumptions. So much in fact, that assumptions resulting mildly imprecise models may lead to unfortunate assessment of damage. The results show that attention to detail is important when a numerical model is to be constructed and that the analyst must have knowledge of the numerical issues that may arise in order to arrive at a correct assessment. Further work is necessary to quantify the effects of modeling assumptions.

# Sammendrag

I løpet av de siste tiårene har det blitt utviklet komplekse numeriske modeller. De kan beskrive komplekse fenomener som er vanlige under jordskjelv, som for eksempel ikke-lineær materialrespons og effekter av lokalisering. Korrekt kalibrering av den numeriske modellen er avgjørende for å utnytte nye analytiske metoder. Etter hvert som modellene blir mer komplekse, kreves mer kunnskap for å gjøre riktige antagelser. Disse antagelsene har stor betydning for resultatet av analysene og kan føre til unøyaktig skadeanalyse.

Målet med denne oppgaven var å undersøke effekten av antagelser i modellene gjennom analyser av en rammekonstruksjon av armert betong. Både ikke-lineære dynamiske analyser og statiske analyser har blitt gjennomført ettersom disse metodene komplimenterer hverandre. Ulike modellkonfigurasjoner har blitt brukt for å undersøke effekten av forskjellene i modellene. Den analyserte bygningen har få etasjer med høy grad av regularitet, noe som legitimerer analyser av en substruktur. Alle analyser har derfor blitt utført på en 2D-ramme.

Både globale og lokale responser ble vurdert. Resultatene viste at modellantagelsene har en betydelig påvirkning på responsen. Dette ble observert på både globalt og lokalt nivå. De resulterende responshistoriene av takets forskyvninger viste at for FB elementer, førte økende antall integrasjonspunkter til at responshistoriene nærmet seg en stabil løsning. Det samme gjelder i IDR-profilene beregnet ved maksimal takforskyvning. For BwH-modellen førte varierende flyteleddslengde til variasjon, og delvis ekstreme variasjoner, i responshistoriene. Store forskjeller i kurvaturresponsen, som er viktig i skadeanalyse, ble også observert for forskjellige modellkonfigurasjoner.

Blant konklusjonene som kan trekkes fra disse resultatene, er at seks eller fler integrasjonspunkter bør brukes for fleksibilitetsbaserte elementmodeller i ikke-lineære dynamiske analyser. Resultatene tydeliggjør også at målte kurvaturer er meget sensitive for modellantagelser, faktisk i så stor grad at antagelser som fører til noe upresise modeller kan føre til uheldig vurdering av skade. Dette viser at fokus på detaljer er viktig når numeriske modeller blir laget, og at analytikeren må ha kunnskap om numeriske utfordringer som kan oppstå for å unngå feilvurderinger. Videre arbeid kreves for å kvantifisere modellantagelsenes påvirkning på modellene.

# Contents

# List of abbreviations

**BIM** building information modeling

**BwH** beam with hinges

**DB** displacement based

**DM** damage measure

**DOF** degree of freedom

**FB** force based

**FE** finite element

**GUI** graphical user interface

**IDA** incremental dynamic analysis

**IDR** inter-story drift ratio

**IM** intensity measure

**IP** integration point

**MAF** mean annual frequency

**MMPA** modified modal pushover analysis

**MPA** modal pushover analysis

**MRF** moment resisting frame

**NSP** nonlinear static procedure

**NTHA** nonlinear time-history analysis

**OpenSees** the open system for earthquake engineering simulation

**PBSD** performance-based seismic design

**PEER** the pacific earthquake engineering research center

**RDR** roof drift ratio

**SCWB** strong column-weak beam

**SMRF** steel moment resisting frame

**SPO** static pushover analysis

# Chapter 1

# Introduction

## 1.1 Background

Designing structures that are able to withstand seismic loads is important. Although no structure can be fail-proof for earthquakes of all magnitudes, they should be able to ensure public safety. The consequences of structural damage caused by earthquakes are so severe that it cannot be overstated how important it is with good design in this regard. As pointed out in the literature [1–3], the damage and loss of life due to recent earthquakes have led to extensive research on the subject of seismic design during the last decades, spawning new methods of analysis. Structures complying to modern building codes show good resilience to earthquakes compared to non-complying structures [4]. As the building codes include new ways to asses this resilience, new methods are introduced.

The most common way of analyzing the seismic strength of structures has been to do linear static analysis using gradually increasing lateral forces to assess the lateral stiffness. These analyses fail to take into account the complex behaviour of earthquake response, which is dynamic and nonlinear in nature. A newer way of designing a structure is by performance-based seismic design (PBSD), where the performance of the structure is assessed. Performance is not solely synonymous with strength. When doing PBSD, it becomes evident that increasing strength not necessarily gives increased safety in this context. Ensuring that the response of a building is such a way that public safety is maintained, is the primary goal.

As new and more advanced procedures and analyses are used in seismic design, the numerical models become more complex. Inelastic material behaviour, cyclic degradation, geometric nonlineareties and localization must be modeled in a sufficient manner and the research community is finding new ways to do so [5–7]. The assumptions made in the making of a numerical model, can have severe implications for the results of the analyses in which they are used [5, 8–10]. Plastic rotations and curvatures of beams are important measures for the assessment of the structural state in seismic design [5]. They are used in building codes and have been shown to be sensitive to differences in numerical modeling [11]. These facts highlight the importance for understanding of such sensitivities. As the complexity of the analyses increases, the analyst must know which numerical tools to use and how modeling assumptions regarding them affects the results.

## 1.2 Objective

The objective of this thesis is to investigate how different numerical modeling techniques compare and how the modeling assumptions associated with them affect their results. Plastic rotations and roof drifts will be of primary focus. This will be done evaluating a reinforced concrete moment resisting frame (MRF) using two different methods of analysis; static pushover analysis (SPO) and a nonlinear time-history analysis (NTHA). Both methods are used as tools in methodologies which are frequently used by engineers today. The analyses are performed primarily using the open system for earthquake engineering simulation (OpenSees), which is an advanced computational tool frequently used in the literature [5, 12].

# Chapter 2

# Literature review

## 2.1 OpenSees and Robot

OpenSees is an open-source software framework developed at the Pacific Earthquake Engineering Research Center (PEER). It is used for simulating the response of structural and geotechnical systems to earthquake loading [13]. OpenSees interprets input written in the tcl programming language, which is extended with special commands native to the OpenSees framework. Such commands define objects as nodes and elements or choose algorithms and integrators for the analysis. A graphical user interface (GUI) using the OpenSees software framework do exist (The OpenSees Navigator). This was not used however, because the author was not aware of such an application when starting out. For anyone that want to use the OpenSees framework, this is worth looking into. The author suspects, with a very limited knowledge about such applications, that some of the flexibility that lies in writing scripts ”by hand” may be lost.

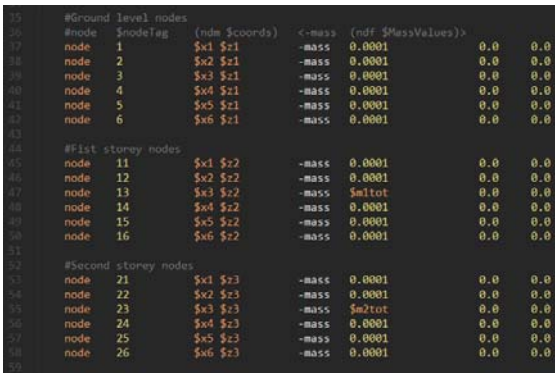


**(a)** Defining nodes.

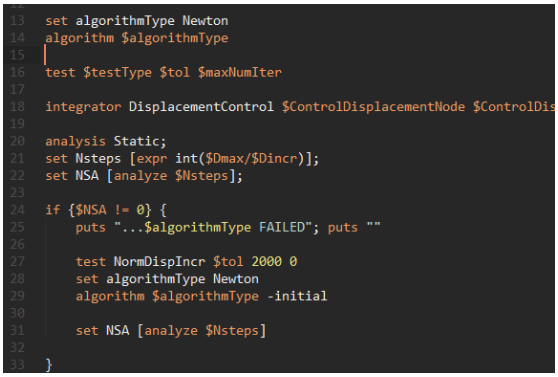


**(b)** Establishing first-mode static pushover procedure.

**Figure 2.1:** Screen captures of tcl-files written using the OpenSees framework.

When programming using OpenSees and tcl, the user has many possibilities; it is flexible and there are many material models, algorithms and integrators. It is easy to run several analyses in loops and changing one parameter at a time, while data is being recorded and neatly put into output files. This enables the user to easily perform parametric studies.

Building a finite element (FE) model and running a nonlinear analysis using OpenSees is tedious work. Each node in the model must be individually defined with its unique coordinates. Elements and their settings must be defined with its properties and nodes. The

model building process can be made more efficient by using for-loops and lists, but still, it is time consuming. Another downside with OpenSees is that discovering sources of error requires a lot of experience. Some of the scripts used in this thesis can be found in Appendix H and the reader is recommended to take a look at these at this stage.

A wiki-style documentation is available through the the OpenSees website [13]. Additional information and documentation can be found here. The wiki does not only explain how different commands work, but sometimes points to articles explaining the relevant theory as well.

#### Robot

Robot is a commercial structural analysis software developed for professional engineers. It has a conventional GUI and has advanced building information modeling (BIM) capabilities. A more thorough introduction to the software is not needed due to the extent it is used in this work.

## 2.2 Performance-based design and the numerical model

### 2.2.1 Outline

Performance based design is no novelty. To design a structure based on its performance under realistic and unsimplified conditions is necessary when building codes do not offer the necessary tools. Seismic design is special in the sense that when a structure is subjected to large earthquake loading, the main goal is to prevent loss of life. Obviously, for many earthquakes that a structure is expected to experience, prevention of damage is essential and the structure should resist the forces without yielding. But, in order to prevent loss of life during larger earthquakes, the full capacity of the structure must be utilized, that is the post-yield capacity. Because of this, novel analyses and techniques have been developed in the recent decades. Methods considering the large differences between earthquakes and effects like structural damping and cyclic degradation are being deployed [14–16].

A focus on the strength of the structure, that is its ability to resist lateral displacement, has dominated the seismic design of low-rise buildings in past decades [1]. This is also reflected in the design codes [14]. The reason for this is that the analyses used are simple, and most importantly quick. Although lateral stiffness is essential, the seismic response of a structure is more nuanced. This is because of its dynamic nature. Under earthquake loading, repeated stress reversals and high stresses are the main source of damage [16]. Static analyses only consider the latter.

No matter what kind of analysis is performed, it is naturally done using a FE program. The structure must be modeled numerically in its entirety or in a simplified way. A part of the structure may possess enough information to depict the response of the entire structure. In this thesis, a numerical model of a structure or a representative substructure will be referred

to as ”the numerical model”. This distinction is necessary since sections or elements in the numerical model are by definition numerical models themselves.

The Norwegian seismic design code, NS-EN 1998-1, hereby referred to as EN 1998, is the governing code for seismic design in Norway [17]. In the context of PBSD, EN 1998 demands that regions where plastic hinges is expected to occur should be able to undergo large plastic rotations (sub-clause 5.2.3.4 (1)P). Subsequently, the numerical model must be able to describe these phenomena as well.

### 2.2.2 Assessing damage

The structural performance is measured using what is called damage measures (DM) or response indicators. A number of DMs are used: inter-story drift ratios (IDR), plastic rotations and capacity curves [8]. Capacity curves usually describe the base shear as a function of the roof drift. Assessing collapse mechanisms are also useful. Doing so can help identify adverse design that lead to an undesired mechanism. The sought after collapse mechanism is one where the beams yield before the columns, taking advantage of the full capacity of the beams before global instability occurs. Adhering to the strong column-weak beam (SCWB) principle is to design columns such a way that they can resist the largest possible moment imposed on them by adjacent beams while remaining elastic, which lead to the desired mechanism.

According to the principle in NS 1998 sub-clause 5.2.2.4 (2), sufficient curvature ductility must be provided in critical regions. This is to prevent unacceptable damage. The compliance with this principle is evaluated using a demand based on a curvature ductility factor $\mu$. This factor is the ratio ” ...of the post-ultimate strength curvature at 85 percent of the moment resistance, to the curvature at yield...” [17]. NS 1998 define strain limits that are not to be exceeded. The importance of proper modeling becomes apparent. These measures have been shown to be greatly affected by the element models applied in the numerical model [11].

Zeris et al. [8] found that DMs can easily be underestimated due to the numerical model. It was also stated that for both static and dynamic analysis, there were significant uncertainties related to the prediction of seismic performance due to the numerical model. Even when using widely adopted modeling assumptions, DMs and collapse mechanisms varied significantly. They further argued that the numerical model should be considered in standardized PBSD procedures.

## 2.3 Methodologies and procedures

The different analytic procedures available to an analyst give different insights to the performance of the structure. The procedures that are about to be presented are only steps in larger methodologies.

### 2.3.1 Static pushover analysis - SPO

The pushover analysis, or static pushover analysis (SPO), is a nonlinear static procedure (NSP) serving as a tool for seismic performance assessment. There are several different ways of conducting a pushover analysis ranging from simpler to advanced and more precise methods. However, they are all static and nonlinear in nature. Whichever is conducted, the idea is to subject a structure to a pattern of monotonically increasing loads until a control node has reached a critical displacement (control displacement). Gravity loads are applied first and held constant throughout [14, 18]. Pushover analysis methods should not be confused with lateral force methods which deal with elastic systems. These will not be discussed.

The simplest of the SPOs are the triangular pushover analysis and the first-mode pushover analysis (Figure 2.2). Modal pushover analysis (MPA) and modified modal pushover analysis (MMPA) are advanced methods [9]. The first-mode pushover analysis uses the first eigenvector as a load pattern and pushes the structure to the limit value. This method has the obvious disadvantage that it does not consider any mode but the first. Since the first-mode pushover analysis is so simple, and therefore quick, it has been the preferred method for professional engineers [1]. This is also the simplest nonlinear analysis method used in EN 1998 [17]. The MPA uses several modal pushover analyses and combines their result, allowing higher mode effects to be captures. The MMPA modifies this approach considering the effects of higher modes.

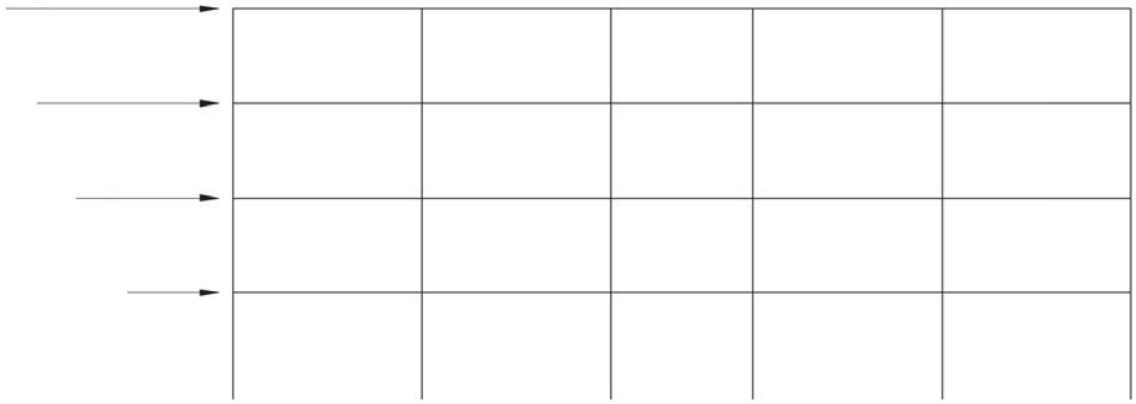

**Figure 2.2:** Force distribution in a first-mode SPO.

SPOs are used to gain understanding of how a given structure will behave when subjected to seismic loads. The pushover analyses are useful to find overstrength inherent in the structure and to estimate plastic mechanisms and damage distributions [17, 19]. Although the method can be seen as simple, it gives a clear picture of the lateral stiffness of any system. Results can be visualized in different ways. IDRs show the inter-story drift normalized using the height of that story. Local behaviour is usually displayed using moment-curvature relationships. The capacity curve however, sometimes called the pushover curve, is the most important. It is the base shear plotted against the control displacement and gives a clear picture of the lateral stiffness of the structure [14].

Pushover analyses are tools in a larger methodology for seismic analysis. NS 1998 gives such a methodology [17]. In this code the target displacement is determined by using the elastic ground acceleration response spectrum which takes damping, natural frequency and soil conditions into account. A textbook example of a MPA procedure can be found in Chopra's *Dynamics of Structures* [14].

SPO is most suitable for symmetric low-rise buildings with short natural periods [15]. Common moment resisting frame (MRF) falls in this category. Dynamic effects as damping, inertia effects and degradation are not captured by the SPOs alone [9], nor do they include effect of earthquake duration. These shortcomings give reasons to perform more advanced dynamic analyses.

### 2.3.2 Nonlinear time history analysis - NTHA

Nonlinear time-history analysis (NTHA) is a nonlinear dynamic method. In this method, a structure is subjected to a (oftentimes scaled) ground motion acceleration and the structural response is calculated as a function of time [14]. It gives direct insight to cyclic degradation and other dynamic effects. The calculated response is naturally highly sensitive to the ground motion acceleration used to excite the structure. This requires the analyst to choose records carefully. The records chosen for a specific structure should reflect the on-site soil conditions, distance from fault and the seismic hazard level [20]. The duration of the record can also be decisive depending on the ductility and the energy-dissipating characteristics of the structures [21, 22]. Since repeated stress reversals and high stresses are the main source of damage [16], this may seem natural. There are different conclusions regarding the importance of duration, and this may be due to the use of different DMs [21].

Due to the sensitivity of the calculated response to the ground acceleration record, several different records are necessary to adequately map the seismic performance [15, 23]. The seismic code states that in order to use the average response quantities, at least seven (code complying) records must be used [17]. A higher number of records are common in the literature, generally a range between 10 to 30 [24]. The selection of records can be a daunting task, and using a large ensemble can be time consuming. Therefore some research have been done to limit the number of records [25].

In NTHA, the records used must be of the sort and magnitude expected at the location of the structure. Guidelines for this important selection process can be found in FEMA (P695) [26]. Since there will be a limited number of records that can be used for a certain site, and the fact that they may not be intense enough, scaling of records is almost always necessary. How they are scaled differs, but the usual method is to scale the record so that its response spectrum match a sought after response spectrum. Such spectra can be found in EN 1998 and in other design codes.

For a thorough assessment of the seismic resistance of a structure, IDA may be used. Incremental dynamic analysis (IDA) is a method of analyzing seismic response using an ensemble of NTHAs. The name implies a procedure similar to NTHA, but refer to a methodology used for performance-based seismic design. An IDA study involves analyzing the results of the ensemble of NTHAs, producing curves showing a DM versus an intensity

measure (IM) [24, 27]. Unsurprisingly, these curves are called IDA curves. The DM is any parameter that describes the state of the structure, for example roof displacement or base shear. IMs are also called monotonic scalable ground motion intensity measure, to reflect that they are monotonically increasing functions of the base record and a scale factor $\lambda$ [27].

Probabilistic methods enable a summary of IDA curves [27]. Using either parametric or non-parametric methods, the response spectra can be summarized and the corresponding IDA curves may subsequently be defined. This summary ”smooths over” the problematic input sensitivity of the NTHA methods giving a more general insight. This can be used to estimate the mean annual frequency (MAF) of exceeding a certain limit-state, based on an IM- or DM-based demand [24].

Numerical non-convergence signals global instability and could be used in IDA and NTHA studies to describe the state of the system [27]. The numerical model has obviously a big effect on the overall results of any IDA study. It has been shown that not considering effects of uncertainties regarding the model, almost always lead to an unconservative estimation [28].

It is obvious that the NTHA gives the most insight to the seismic response of the building compared to a SPO. The NTHA subjects the numerical structure to realistic, unsimplified design effects, but it does not give a clear picture of the lateral stiffness of the structure. This can be seen as incentives to perform both analyses. More advanced SPOs than those discussed here have been developed. However, they do not provide enough insight to make the NTHA redundant [29].

## 2.4 Element models

There exist many different approaches to modeling plastic behaviour. The discrete (lumped) plasticity models assign inelastic behaviour rules to member ends, using some kind of rotational spring. The discrete models separate element behaviours, and thus axial-moment interaction will not be captured [5], which is a disadvantage. The upside to these models is their numerical efficiency. The structure may also be modeled using the FE method, meshing the structure into extremely small FEs. Doing so enables the capturing of complex constitutive behaviour with high accuracy, but this comes with an equally high computational demand. This is often so high that it makes this type of model unpractical. There are many models that lie in between these two extreme levels of refinement, one of which is the distributed plasticity models.

#### Distributed plasticity models

Distributed plasticity models allow plastic behaviour to occur over an entire element length and can be implemented using FEs based on either the stiffness formulation or the flexibility formulation. The latter will be elaborated on shortly. Inelastic properties are defined at integration sections along the FE, each contributing to the global inelasticity of the FE [11]. These sections are usually divided into finite areas, or fibers, which are assigned a

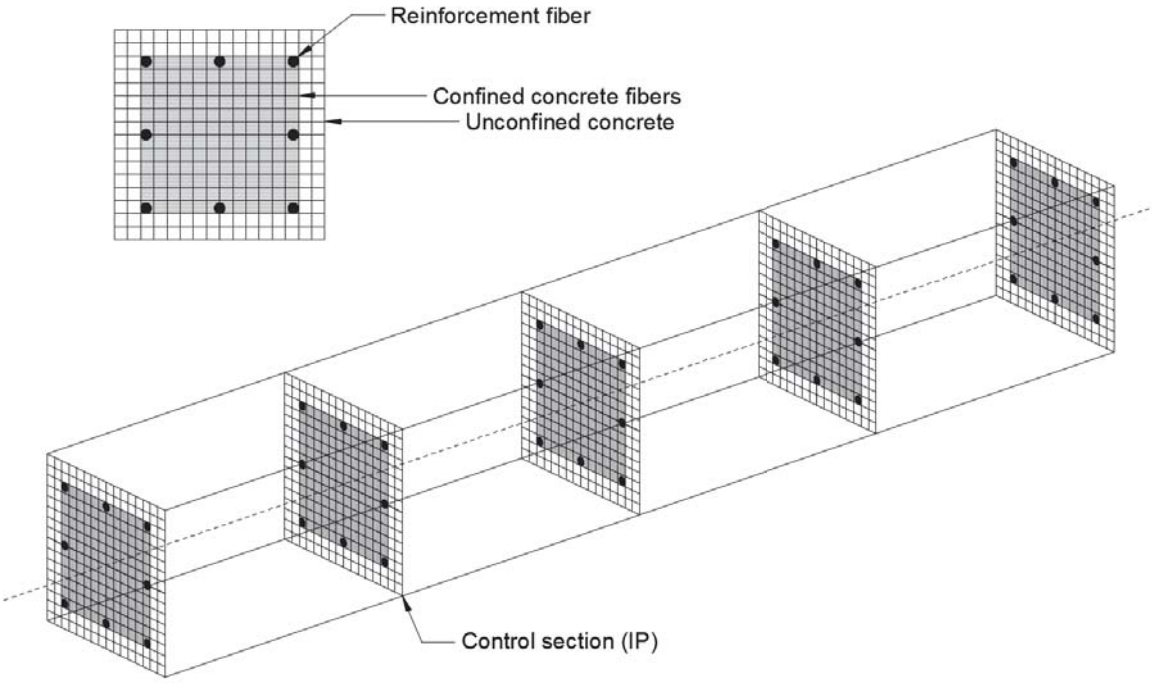


**Figure 2.3:** Illustration of the distributed plasticity model. One FE with five integration sections.

material uni-axial inelastic relationship. Figure 2.3 illustrates this model. When representing the integration section using too few fibers, the section capacity is underestimated [30]. Increasing the number of fibers beyond what is strictly necessary does not affect the objectivity of the result [31, 32]. Increasing the number of fibers does, however, require more computational effort. Integration sections go by several names in the literature: integration point (IP), control section and integration section.

The author failed to find any literature that gave a simple rule for choosing the number of fibers. Increasing the number of fibers obviously affects computational time spent, but any quantification of this was not found. In the literature, different number of fibers are used [30, 32, 33], ranging between around a 100 to 500 for the entire section. In a paper by Capone, Filippou and Taucer [30] a reference is made to a PhD thesis which deals with this issue. The author was not able to find it.

Distributed plasticity models have two big advantages. They allow plastic hinges to form throughout the element and do not require any prior calibration or pre-defined hysteresis response. They also allow direct modeling of N-M interactions and allow for modeling of softening behaviour, which lumped plasticity models do not [34]. Many of the initial limitations with this model have been sorted out. For example, Ceresa et al. [6] have addressed shear-flexure coupling under cyclic loading.

One numerical issue that must be addressed using this model is localization. Experiments have shown that when a specimen is subjected to axial compression, the global response does not only depend on the material properties, but the size of the specimen as well. The collapse of a specimen is due to localization of stresses in the whole body causing a local

mechanism [11]. Therefore this issue is mainly of concern for softening response. This makes it more acute for RC structures as steel structures usually display hardening response under earthquake loads [35].

The term localization describes both a physical and a numerical phenomenon. Stresses tend to localize in the most stressed IPs in the most stressed element. Numerical localization leads to nonobjective response for different reasons depending on the FE formulation. To restore an objective response, regularization techniques are required. Calabrese, Almeida and Pinho have addressed numerical issues and regularization techniques for RC frame elements in their 2010 paper [11]. This paper has been an important source of information. Before presenting some of the techniques, additional information about each FE formulation is required.

### The stiffness formulation - displacement based elements

The classical FEs are formulated using the stiffness formulation. For these elements, interpolation functions are used to describe a displacement field along the element satisfying equilibrium in an integral sense only. Element forces are found by energy considerations. These types of elements will be referred to as DB elements (displacement based elements).

Since the curvature field can become highly nonlinear when plastic hinges occur, the DB elements with their imposed displacement field cannot capture the real deformed shape. This formulation necessitates meshing. DB elements must have a refined mesh to model the the inelastic curvatures. The analyst can try to predict where the inelastic behaviour will take place and refine the mesh at that location, but risks more discretization errors. Refining the mesh uniformly will demand more computational effort.

The Gauss-Legendre integration rule is commonly used for the DB elements as it is the most accurate one [36]. Calabrese et al. [11] show that there is no reason to use more than two IPs using this rule. This rule has no IPs at the element ends where moments usually are largest. This error is reduced when the number of FEs increases since the distance between the ends and the extremal IPs gets shorter.

When it comes to modeling softening behaviour, the stresses localize in the most strained IP in the most strained element [11]. As the FE mesh is refined, larger and larger stresses are required inside an element to produce same values of displacement, making the response nonobjective. In other words, as the mesh is refined, the solution will not converge. According to Calabrese et al. [11] there are limited regularization techniques for the DB element, but one way is to set the extremity elements lengths equal to twice the length of plastification. By doing this, the IP where localization occurs, integrate over the entire area of plastification and thereby capturing the objective response.

### The flexibility formulation - force based elements

The flexibility formulation uses force interpolation functions for the variation of internal forces over the element length which represent the exact solution to the governing equations

[37, 38]. Even for nonlinear material response, it satisfies equilibrium [30]. Elements using this formulation have been shown to capture inelastic behaviour more accurately than DB elements [33]. This allows a one-to-one correspondence between structural members and the FEs, hence, no discretization error occurs. This formulation does not restrain the development of inelastic deformations in a member as the DB element does, making it ideal for analyses where inelastic deformations occur. These types of elements will be referred to as FB elements (force based elements).

The most common integration rule for this element is the Gauss-Lobatto integration rule because it puts the IPs at the ends of the element. This is where internal moment is largest for typical frame elements and elements without internal forces. Four to six IPs are necessary to accurately represent nonlinear material response [37]. As for all the other quadrature rules, weights and locations are usually tabulated in handbooks. They can also be found online [39].

When modeling softening behaviour, stresses localize in the most stressed IP in the force based element. No convergence is obtained in this situation, and post-peak results are in fact without physical meaning [11]. The mechanism is explained as follows. The total rotation in the element is sampled over the characteristic length of the ctitical IP. This rotation must always be the same to satesfy the equilibrium imposed in the flexibility formulation. When the number of IPs increase, the characteristic length shortens. Thus, in the IP, increasing curvatures are required to achieve the same prescribed displacement. The characteristic length of the IP is, in essence, the plastic hinge length (length of plasticity) for any FB FE where curvatures localize in this IP.

One regularization technique modifies the concrete so that a constant fracture energy is maintained. This was proposed by Coleman and Spacone [35]. Another results in the plastic hinge element, which uses integration methods which specify the length of plastification, $l_p$. This makes it possible to determine a length of plastification that maintains a constant fracture energy [5]. As will shortly be presented, simpler methods are available.

### Plastic hinge elements

The plastic hinge element used is a force-based element that uses the plastic hinge integration method suggested by Scott and Fenves [5]. The model is a regularization technique that address the nonobjective response of FB elements that experience strain softening behaviour. As with other plastic hinge methods, plastic hinge zones are defined at each end. The lengths of these zones, $l_p$, are determined so that they cover the parts of the element where it is expected that material nonlineareties might occur. There are different approaches to determine $l_p$, one of which is using empirical equations. One example is the equation suggested by Paulay and Priestley [40], see equation 2.1. To clarify, this element is regarded as a lumped plasticity element model in parts of the literature. This is because it in its original form confines nonlineareties to the hinge lengths. This categorization is not made here in order to distinguish it from the lumped plasticity models that use rotational springs.

$$l_p = 0.08L + 0.022 f_y d_b \tag{2.1}$$

In equation 2.1, $L$ is the element length in millimeters, $f_y$ is the yield strength of reinforcing bars in MPa and $d_b$ is the diameter of reinforcing bars, also in millimeters. This is a simple equation that is used in the literature [5, 11]. Paulay and Priestly state in their book [40] that, for frame elements with normal proportions, this equation usually yields $l_p$ = 0.5 h, where h is the depth of the cross section. However, it should be noted that the normal proportions of today may not be the same as the normal proportions of 1992 (year of publication).

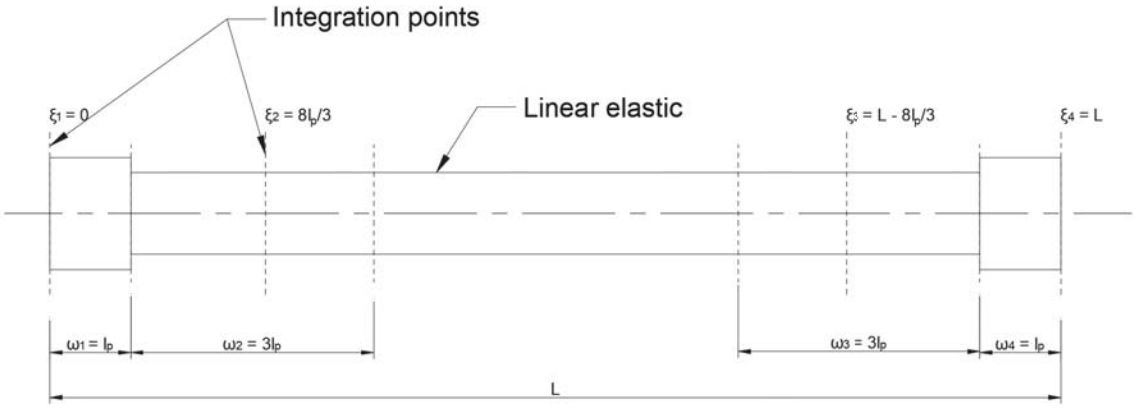


**Figure 2.4:** Beam with hinges element using the modified Gauss-Radeu integration rule.

In OpenSees, the element originally had an elastic zone between the two plastic zones, limiting the development of plastic hinges to the two end zones consistent with the model of Scott and Fenves. The rule used in this element is the modified Gauss-Radau integration rule. This method of integration uses a two-point Gauss-Radau rule over a length of four times the plastic hinge length. The positions ($\xi$) and weights ($\omega$) are as shown below and illustrated in Figure 2.4. Originally, the IPs on the interior were linear elastic and thus inelastic response was limited to IPs at the ends.

$$\xi = \{0, 8l_p/3, L - 8l_p/3, L\} \qquad \omega = \{l_p, 3l_p, 3l_p, l_p\}$$

Equation 2.2 is the equation for the element flexibility presented by Scott and Fenves [5].

$$\boldsymbol{f} = \sum_{i=1}^{N_p} (\boldsymbol{b}^T \boldsymbol{f}_s \boldsymbol{b}|_{x=\xi_i})\omega_i + \boldsymbol{f}_{int}^e \tag{2.2}$$

Here, the first part captures the contribution of the numerical integration of the plastic hinge regions and $\boldsymbol{f}_{int}^e$ is the flexibility of the interior. This quantity is, for the modified Gauss-Radau used in the beam with hinges (BwH) element, given by equation 2.3.

$$\boldsymbol{f}_{int}^e = (\boldsymbol{b}^T \boldsymbol{f}_s^e \boldsymbol{b}|_{x=8/3l_{pi}})3l_{pi} + \int_{4l_{pi}}^{L-4l_{pj}} \boldsymbol{b}^T \boldsymbol{f}_s^e \boldsymbol{b} dx + (\boldsymbol{b}^T \boldsymbol{f}_s^e \boldsymbol{b}|_{x=L-8/3l_{pj}})3l_{pj} \tag{2.3}$$

In this equation, the contribution for the two IPs at $x = 8/3l_{pi}$ and $x = L - 8/3l_{pj}$ is included together with an integral that captures the elastic behavior of the interior not captured by these sections.

The BwH element has been further developed. When constructing a BwH element, the analyst can use any type of section in the interior in OpenSees [41]. For example, a fiber section model with a nonlinear material model can be used to enable plastic hinges to form in the interior or assign hysteresis rules to it. Any type of section available in OpenSees can be used. In the interior, a two-point Gauss rule is used to calculate the flexibility. In total, there are six IPs in the BwH element, and the rules associated with the sections displayed in Figure 2.4 (i.e. $4l_p$ regions) are well documented. However, the rules associated with the two IPs in the interior are not. In this literature review, no such documentation was found.

The BwH element is a force based element as it is formulated using the flexibility formulation. It should therefore be considered as an element in the FB family of elements. But in order to distinguish this element from the pure distributed plasticity FB element (using Gauss-Lobatto), it will be referred to as the beam with hinges element (BwH element). Also, the global numerical models using the different element models will be referred to as FB model, BwH model etc.

The BwH element has shown to give good results for nonlinear analysis where softening or degradation occurs [5]. Incorrect calibration of the BwH element may lead to overestimating the lateral load capacity for a planar frame structure [42]. This was observed when strain hardening occurred in the structure. Not only does this demonstrate how significant the calibration of the elements is, but it also shows that any analyst must have knowledge of such behaviour.

Recent work on the subject of frame elements which develop plastic hinges is worth mentioning. Feng and Ren have proposed a new FB element enriched with evolutionary plastic hinges which seemed to perform well for both softening and hardening response [7]. Other elements have also been proposed [33, 43–45]. These works are mentioned to give a picture of the state of the art and will not be used. They also show that these kinds of frame elements are of interest to the engineering community.

## 2.5 Material model

The material models used in any analyses must be able to describe the expected material behaviour. For linear static problems this is quite simple - it has to describe the classical stress-strain relationship for the material. For nonlinear dynamic problems there are more complicated effects taking place. Plastic hinges may occur during violent oscillations. The most important factors for the concrete behaviour under these circumcises are confinement and strain rate. Material nonlinearity is crucial for the dynamic response of low- and mid-rise structures [1].

The effect on confinement by means of transverse reinforcement is known to be significant. This has been documented by, among others, Larsen et al. [46] who documented that

the collapse probability for a given structure was 1.2% when considering confinement in compliance with the code and 12% when confinement was not considered. This illustrates the importance of modeling confinement properly.

According to Mander, Priestley and Park [47], tests have shown that confinement gives a significant increase in both ductility and strength for concrete in compression. They state that this strength enhancement together with the concrete stress-strain relationship greatly influence the strength and ductility of a member. In their 1988 paper, they define a theoretical stress-strain relationship for confined concrete which includes the effects of confinement, strain rate and cyclic loading.

The formulation proposed by Mander, Priestley and Park [47] builds on the relationship presented by Popovics in 1973 [48], and the model is used in much of the literature on the subject of numerical simulation of RC structures. It is able to model the material behaviour expected in elements of any RC MRF.

Figure 2.5 was recited by Mander, Priestley and Park from prior work [10]. The figure shows a proposed stress-strain model for monotonic loading based on one of Popovics equations [48]. It shows how big effect correct modeling of confined concrete will have on the performance of the modeled structure. A member with confined concrete modeled in this way will be much more ductile and reach significantly larger deformations.

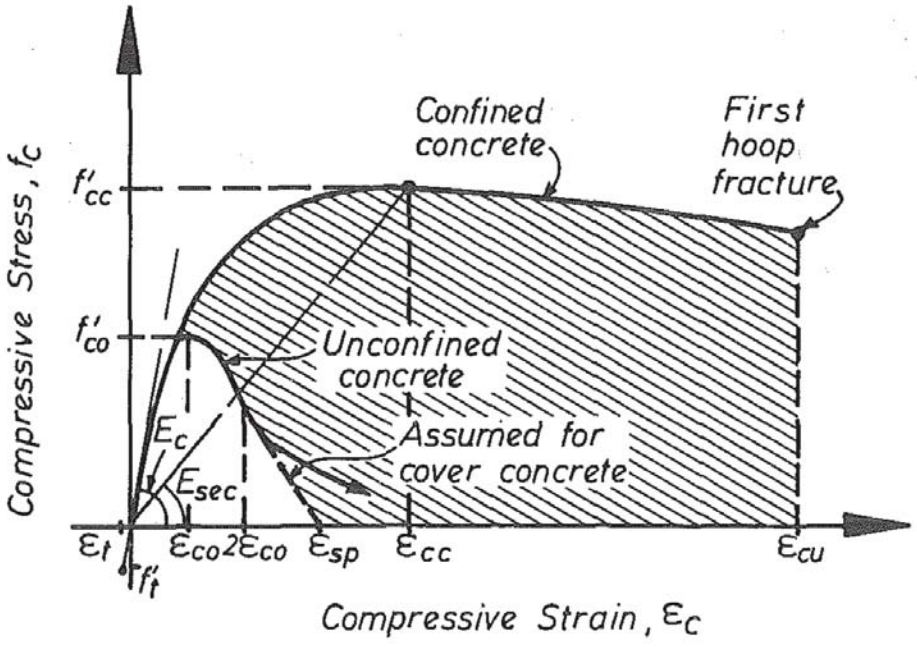


**Figure 2.5:** Stress-strain model proposed for monotonic loading of confined and unconfined concrete [47].

It is not just the confinement the material model by Mander, Priestley and Park considered - strain rate was also accounted for. Higher strain rates are known to give stiffer response. They also result in larger peak stresses and lower strains at these peak stresses [47]. These effects were accounted for in the model by multiplying the compressive strength, modulus

of elasticity and strain at peak stress with respective dynamic magnification factors. For example, the dynamic strength is $f'_{co.dyn} = D_f f'_{co}$. The respective dynamic magnification factors presented by Mander, Priestley and Park are given in equation 2.4. Dynamic magnification factors $D_f$ and $D_E$ usually range from 1 to 1.6 and 2 respectively.

$$D_f = \frac{1 + \left(\frac{\epsilon_c}{0.035 {f'_{co}}^2}\right)^{\frac{1}{6}}}{1 + \left(\frac{0.00001}{0.035 {f'_{co}}^2}\right)^{\frac{1}{6}}}, \quad D_E = \frac{1 + \left(\frac{\epsilon_c}{0.035 {f'_{co}}^3}\right)^{\frac{1}{6}}}{1 + \left(\frac{0.00001}{0.035 {f'_{co}}^3}\right)^{\frac{1}{6}}}, \quad D_\epsilon = \frac{1}{3D_f}\left(1 + \sqrt{1 + \frac{3D_f^2}{D_E}}\right) \tag{2.4}$$

Typically, the strain rate varies from $10^{-3}$ $s^{-1}$ to $10^{-2}$ $s^{-1}$ for earthquakes [49]. A strain rate of 0.0167 $s^{-1}$ was used by Scott et al. [50] while Mander, Priestley and Park [51] used 0.013 $s^{-1}$.

Mander, Priestley and Park also present a method based on energy considerations for determining the ultimate strain for the confined concrete [47]. The confined concrete looses all its strength when the first transverse reinforcement breaks, and it is the energy in this reinforcement that is considered. An alternative is equation 2.5 which is found in Paulay and Priestley's textbook [40] which is considered to be conservative.

$$\epsilon_{cu} = 0.004 + 1.4\rho_s\epsilon_{sm}\frac{f_{yh}}{f'_{co}} \tag{2.5}$$

Here, $\epsilon_{cu}$ is the ultimate strain, $\rho_s$ is the ratio of the area of transverse reinforcement to area of the section, which is followed by the steel strain $\epsilon_{sm}$ which corresponds to peak stress. The yield stress of the steel and confined concrete are $f_{yh}$ and $f'_{co}$ respectively. For the unconfined concrete, the ultimate strain can be taken as 0.006 [40].

All in all, the model proposed by Mander, Priestley and Park is a solid and viable one. An effort should be made to map possible phenomena the model should be able to describe for the structure in question. This is because other models than this model can be more descriptive in certain cases. For simulation of flexural-dominated members, the Mander model has been used throughout the literature [5, 11], and is recommended [3].

## 2.6 Damping

Damping in structures are due to energy dissipating mechanisms; mechanisms such as hysteretic behaviour of the structural materials, dry friction due to slippage in joints and air displacement [52]. The contributions from these phenomena are difficult to quantify. A damping matrix cannot be defined in the same manner as mass and stiffness matrices in the design procedure. Consequently, modal damping ratios are often chosen from experimental/recorded data for structures similar to the one being assessed. If such data does not exist, one option is to turn to tabulated recommendations [14]. Most building codes, including the EN 1998, assume a viscous damping ratio of 5% and does not consider the variation of damping with structural materials.

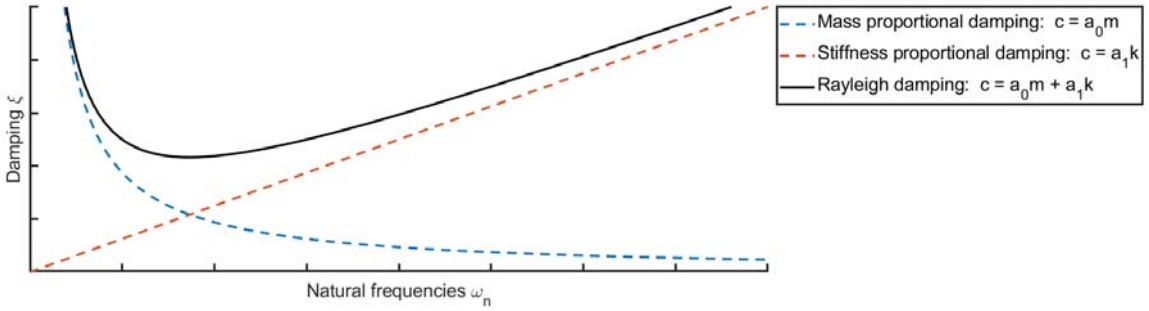


**Figure 2.6:** Rayleigh damping model.

When similar damping mechanisms are evenly distributed throughout the structure, classical damping models are applicable. One such model that have been shown to give satisfactory results is the Rayleigh Damping model. In this model, mass and stiffness proportional damping are both considered using two coefficients, $a_0$ and $a_1$ corresponding to mass and stiffness respectively. Their values are determined by equation 2.7, assuming the same modal damping $\xi$ for the two modes with natural frequencies $\omega_i$ $\omega_j$. The damping matrix $\boldsymbol{c}$ is then determined by equation 2.6. An illustration of the concept is provided in Figure 2.6.

$$\boldsymbol{c} = a_0\boldsymbol{m} + a_1\boldsymbol{k} \tag{2.6}$$

$$a_0 = \xi\frac{2\omega_i\omega_j}{\omega_i + \omega_j} \qquad a_1 = \xi\frac{2}{\omega_i + \omega_j} \tag{2.7}$$

The condition that similar damping mechanisms must be evenly distributed throughout the structure excludes systems with soil-structure interaction, and more importantly, nonlinear models [14]. Thus, it would be natural to assume that representing the damping for inelastic systems would have been the subject of many studies. This problem however seem to be given little consideration in much of the literature. Studies suggest that when establishing a Rayleigh damping model, the tangent stiffness should be used instead of the initial stiffness. This suggestion was made based on observations of unrealistically large damping forces after yielding of members. These studies did not show in detail how the damping model affected demand parameters as explained in a paper by Erduran [53]. Here, these effects are investigated by analyses of a three-story steel moment resisting frame (SMRF) and a nine-story SMRF. It is shown that story-drift demands are not significantly affected by the applied damping model. Moreover, neither mass nor stiffness proportional damping alone gave satisfactory results. The Rayleigh damping model was deemed to be the best alternative, with a cautious recommendation of anchoring it at the reduced first mode frequency and T = 0.2 s, resulting in $\omega_i$ = 0.707$\omega_1$ and $\omega_j$ = 31.4 rad/s.

In a more recent study, Chopra and McKenna [54] provide data showing that a viscous damping matrix constructed by superposition of modal damping matrices eliminates the issues associated with the Rayleigh damping model for nonlinear systems. It was recommended to use this method for nonlinear response history analyses. As in other studies, it

was found that a Rayleigh model using the initial stiffness was inferior to one using the tangent stiffness. But, it was also found that when using a distributed plasticity model, the Rayleigh model leads to acceptable results: "...When the element plasticity model is more sophisticated — in that a fiber model is used to represent structural elements, allowing distributed plasticity — the structural response is not sensitive to the damping model. Even the Rayleigh damping model leads to acceptable results. Thus, there is no intrinsic problem with this damping model, provided that plasticity is modeled properly. This is yet another reason to abandon concentrated plasticity models..." [54].

## 2.7 P-delta effects

Gravity loads produce additional overturning moments when a structure is displaced horizontally. These effects introduce geometrical nonlinearity and are called P-$\delta$ effects. They are always present when a structure undergo lateral displacement, but only become significant for tall or flexible structures, or in structures that is deformed significantly [1].

## 2.8 The NGA-West2 database

Ground motion records have been selected from the NGA-West2 database [55]. This database is a part of the NGA-West2 project at the Pacific Earthquake Engineering Research Center (PEER). The database consists of a large number of ground motions recorded around the world.

## 2.9 Noteworthy

This section introduces some important articles and remarks to this literature review.

The article *Numerical Issues in Distributed Inelasticity Modeling of RC Frame Elements for Seismic Analysis* by Calabrese et al. [11] investigates the effect of element formulations and sectional constitutive behaviour, making this a basis of comparison.

Another noteworthy article presents a thorough overview of the wide subject of seismic engineering: *Seismic assessment of structures and lifelines* by Fragiadakis et al. [1]. With its over 250 references it is a recommended read for anyone new to the subject.

#### Earlier work on structure to be analyzed

The structure which is to be analyzed has been used in previous work [12, 56–58]. In one of these, investigation of over-strength of dual systems has been performed [12].

# Chapter 3

# Analyzed structure

The structure which has been analyzed is a RC structure. Designed as a residential building in southern Europe, it complies with the eurocodes NS-EN 1992-1-1 [59] and NS-EN 1998-1 [17]. It has been designed with ductility class DCM using the lateral force method. The design was performed by Nina Øystad-Larsen. All drawings of the structure and its structural members in this chapter have been made solely by Øystad-Larsen.

All structural elements belong to XC3, M60. The concrete chosen is C30/37 using a 35 mm cover. The reinforcement is of quality B500C with a modulus of elasticity of 200 GPa.

Throughout the design, one notable principle that was adhered to was the SCWB principle. This ensures that the full moment capacity of the beams is utilized before global instability is reached. In the design, the slabs contribution to the beam stiffness was included, giving them an effective flange width and a higher moment capacity. This effective width however will be disregarded throughout this work.

## 3.1 Building layout

The structure is a four-story RC MRF with five bays. It is doubly symmetric in the horizontal plane, making torsional effects due to ground motion negligible. Figure 3.1 shows the plan of the structure. Floor slabs are present in all stories.

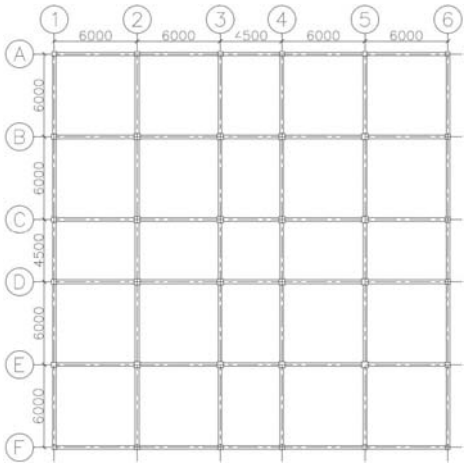


**Figure 3.1:** Plan view of the structure. A larger version is available in Appendix A.

Figure 3.2 shows a vertical projection of the 2D frame along axis B. It is this 2D frame that will be used in the analyses. This frame is representative for the response of the whole structure due to its regularity. The structure satisfies the criterion of regularity set by EN 1998 clause 4.2.3 [17].

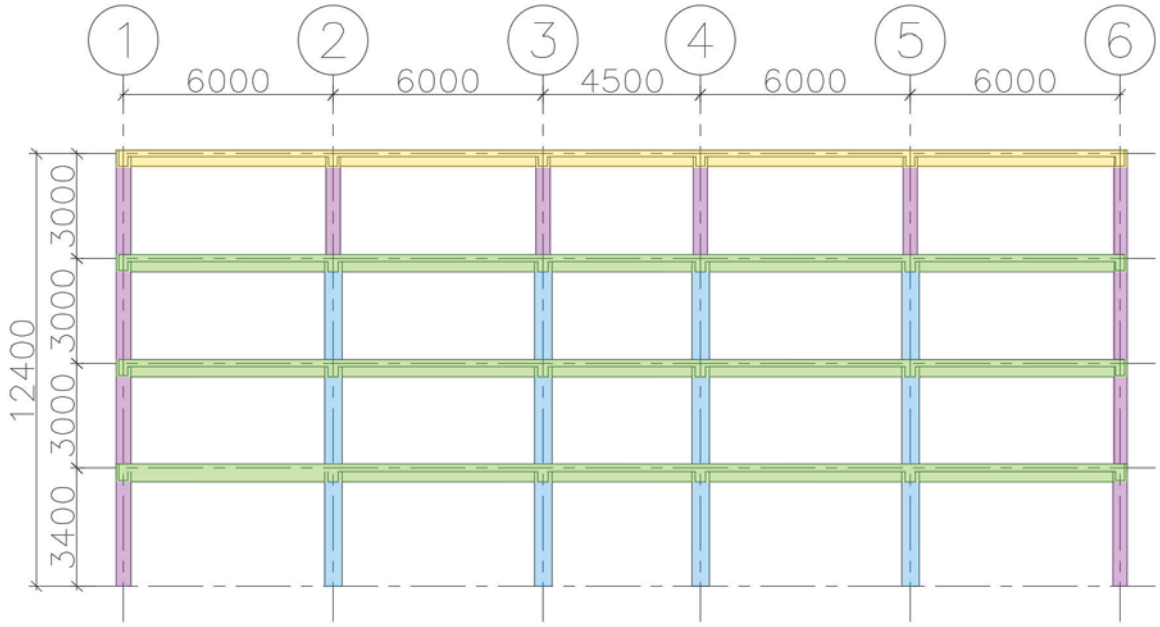


**Figure 3.2:** Vertical projection of 2D frame along axis B. This figure has been provided by Øystad-Larsen.

The cross sectional dimensions and reinforcement layout are given in Appendix A. MN interaction curves for the different structural elements of interest have been plotted in Figure 3.3. Note that the colors correspond to a specific structural member, using the same colors as in Figure 3.2.

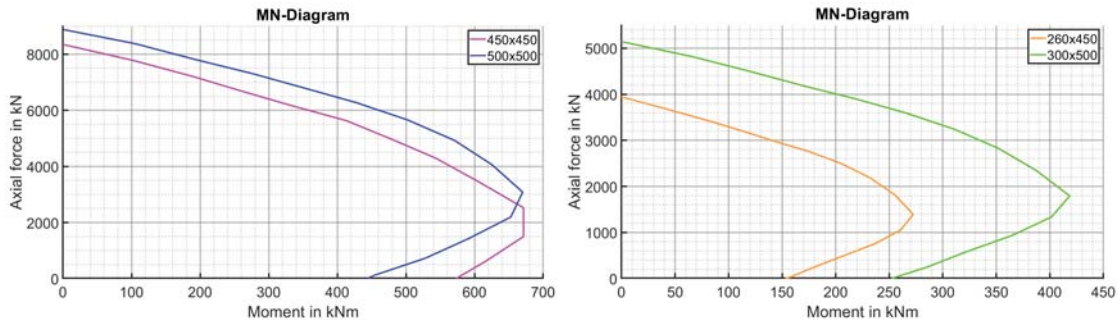


**(a)** Columns **(b)** Beams

**Figure 3.3:** Moment and axial load interaction curves. Calculated using Response 2000.

## 3.2 Mass and loads

The mass of the entire structure is 2 024 tons. First story weighs 531 tons, second 527 tons, third 524 tons and roof 441 tons. The total mass associated with the 2D frame which is to be analyzed (along axis B) is 490 tons. This includes self weight of in-plane structural members as well as self weight of out-of-plane members (beams and slabs) and the loads they are subjected to. These masses were calculated according to EN 1998 clause 3.2.4 and 4.2.4 [17]. Figure 3.4 shows the vertical loads due to the self weight of the out-of-plane plane members (beams and slabs) and their loading.

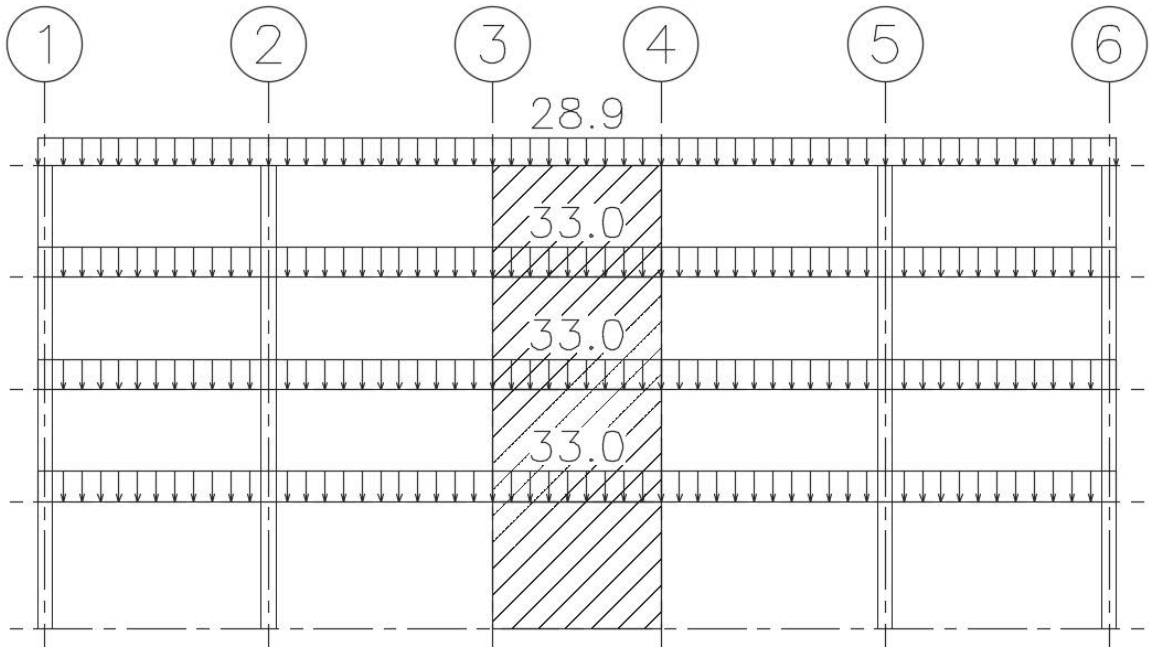


**Figure 3.4:** Vertical loads on 2D model in kN/m. This figure has been provided by Øystad-Larsen.

# Chapter 4

# Numerical model

The basis of the numerical models used in this work are the same for all analyses, with the exception of changing some parameters of interest. They model the 2D frame shown in the previous chapter and thus have the same geometry and cross sectional dimensions. The settings of the parameters that are going to be varied will be presented here. What is common among all the models are the vertical loads, seismic mass and other structural "realities". All sections are formulated in the same way with the same material behaviour.

## 4.1 Concrete material model

The concrete material model should be able to describe all material behaviours expected to occur before collapse during static and dynamic analyses. This includes, among other phenomena, strain softening and hardening, the effects of strain rates and confinement. As stated in section 2.5, the model described by Mander, Priestley and Park [47], which was based on Popovics model [48], describe these phenomena. This model is referred to as the Mander model. The model is also used in much of the relevant literature [5, 7, 11]. As it is able to describe expected behaviour, and also is popular, Mander's concrete model is used in all analyses in this work.

The concrete parameters for the confined concrete are presented in Table 4.1. These were calculated by Øystad-Larsen using the formulas presented by Mander, Priestley and Park. The strain rate used in the calculations was 0.013 $s^{-1}$ as this rate was used in the Mander model. [51]. The parameters shown in the table are the input parameters for the CONCRETE04 (C04) material model in OpenSees. The reinforcement steel was modeled using the simplest model provided in OpenSees for steel, STEEL01. The input parameters for this model were $F_{yk}$ = 500 MPa, $E_s$ = 200 GPa and with a strain hardening ratio of b = 0.005.

| **Name** | $f_c$ | $\epsilon_c$ | $\epsilon_{cu}$ | $E_c$ | $\epsilon_{ct}$ | $\epsilon_t$ |
|---|---|---|---|---|---|---|
| Unconfined concrete | -38.6 | -0.00199 | -0.0060 | 33.916 | 2.9 | 0.0855 |
| 50x50 Conf. concrete | -47.9 | -0.00420 | -0.0142 | - | - | - |
| 45x45 Conf. concrete | -47.1 | -0.00400 | -0.0141 | - | - | - |
| 30x50 Conf. concrete | -42.5 | -0.00300 | -0.0148 | - | - | - |
| 26x45 Conf. concrete | -43.3 | -0.00320 | -0.0199 | - | - | - |

**Table 4.1:** Concrete material parameters.

The C04 material model in OpenSees is presented in the OpenSees wiki as Popovics model [60], but with a modification; its envelope curve corresponds to that of the Mander model. Furthermore, the wiki states that the C04 material has "...a degraded linear unloading/reloading stiffness according to the work of Karsan-Jirsa and tensile strength with exponential decay..." [60].

## 4.2 Fiber sections

The sections in the numerical model are modeled as fiber sections. The number of fibers was selected after some trial and error, resulting in the somewhat odd subdivision shown in Figure 4.1. Each of the five regions in the figure enclosed by thick, black borders is subdivided into 20x20 fibers, resulting in 2000 fibers in total for the entire cross section. This is more fibers than necessary, and a section with less fibers would be more efficient computation-wise. Initially, seemingly reasonable numbers by the standards of the literature were used. However, analyses where these sections were used failed to converge. To avoid further work, the subdivision was chosen so that the number of fibers was well above the required minimum. As will be shown, this section gave reasonable results.

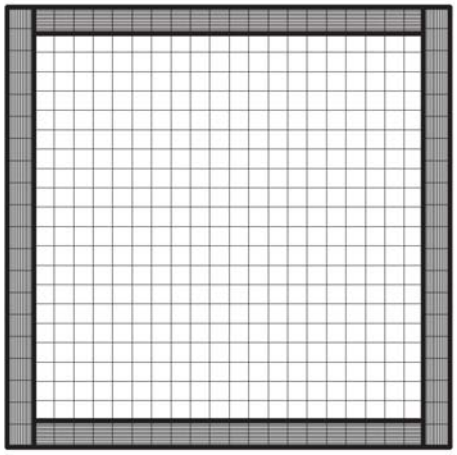

**Figure 4.1:** Cross sectional fiber discretization for 500x500 columns. All other sections are discretized this way.

## 4.3 Finite elements and mesh

Different FEs have been used for analyses, and some of their parameters have been varied. Table 4.2 shows all the different configurations that were used. Because the different elements have been discussed in detail in Chapter 2, their description here will be brief.

| Element | Number of IPs | Special |
|---|---|---|
| **DB Beam-Column** | 2, 5 and 8 | nFE = 4<br>nFE = 8<br>nFE = 18<br>nFE = 24 |
| **FB Beam-Column** | 3 to 8 | - |
| **FB Beam with hinges** | Standard | $l_p$ = 1.0 h<br>$l_p$ = 1.5 h<br>$l_p$ = 2.0 h |
| **FB Beam with hinges with inelastic interior** | Standard | $l_p$ = 1.0 h<br>$l_p$ = 1.5 h<br>$l_p$ = 2.0 h |

**Table 4.2:** Different parameter settings used in analyses.

The first element used is the classical FE - the displacement based (DB) element. The Gauss-Legendre quadrature rule was chosen because it is the most effective [36]. This rule does not assign IPs at the element ends where the moments are largest. This introduce an error, but this error is considered to become insignificant as the FE mesh is made finer. As seen in Table 4.2, analyses of the DB model are performed using different numbers of FEs (nFE). Meshing the model in OpenSees was not a trivial task. The scripts for this process is presented in Appendix H. Figure 4.2 shows the DB model mesh using 4 FEs per structural member. Blue lines depict elements, and node numbers are displayed at the respective node location.

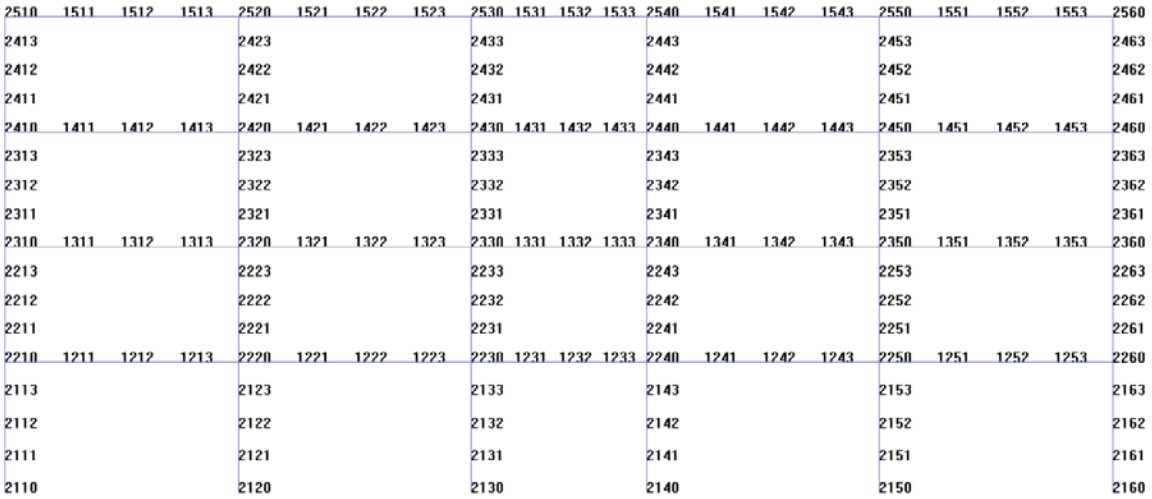


**Figure 4.2:** FE mesh for the DB model with four FEs per structural member.

For the force based (FB) element, the Gauss-Lobatto integration rule was chosen. One of the big advantages of the FB elements is that they allow one-to-one correspondence between the structural members and the FEs (i.e. no meshing is required). Since the members are

modeled with one FE, it is necessary to use a rule that defines IPs at the element ends where moments are largest. This is the reason for choosing the Gauss-Lobatto rule. The numbers of IPs per element used in analyses are presented in Table 4.2 as it is one of the parameters that will be investigated.

For the beam with hinges (BwH) element, the chosen integration rule is the modified Gauss-Radau rule outlined in section 2.4. Both the effects of the hinge lengths and the use of different interior sections will be investigated. The different configurations for the BwH model are also presented in the above table.

When modeling the BwH interior as elastic, the integration rule is as the one outlined in section 2.4. Here the interior sections are represented by simple elastic sections. Only area, second moment of inertia and the Young's modulus are defined. These input values were calculated using Response 2000 and controlled with hand calculations. When an inelastic interior is used, the interior sections are modeled using fiber sections. These fiber sections are the same as those used in the DB model, the FB model and the plastic hinge regions of the BwH model. In this case, specific information on how the interior is integrated numerically was not found. The OpenSees wiki does not provide any additional guide in this regard [41] and it is assumed that no other changes are necessary except for changing the interior sections.

## 4.4 Constraints, loads and global settings

The frame is restricted from any out-of-plane movements. All of the nodes at ground level are fixed, restricting rotation and all displacements at these nodes.

The seismic mass consists of the self weight of the columns, beams and out-of-plane members (beams and slabs). The vertical loads are also applied according to the recommendations in EN 1998. These masses are lumped in their respective vertical level in nodes along axis 3 and act only in the horizontal plane. In other words, they do not contribute to the vertical loads on the structure.

The vertical loads are applied as load patterns in OpenSees. The self weight of the beams, slabs and live loads are uniformly distributed over the beam elements, and the self weight of the columns are distributed over their length. Before any of the main analyses are performed, the vertical loads are applied to the structure. They increase monotonically until they reach their full effect. After this gravity analysis, the vertical loads are set as constant and will remain constant in subsequent analyses.

The validity of the numerical model was tested by considering the natural periods of the structure, calculated using OpenSees and Robot. This was done to verify that the numerical model's initial elastic stiffness was reasonable. As is seen in Table 4.3, it was. The table shows the four first natural periods for three different models. One analysis of the whole structure (3D), as well as an analysis of the simplified 2D frame was done in Robot. The former model was made by Øystad-Larsen while the latter was made by the author. Only the four first in-plane modes of the 3D model were extracted. The results show that the model

in OpenSees was reasonably defined. The periods were calculated using every combination of parameters and element formulations, but only one of these combinations is given in the table. This is because the results were so similar that no interesting conclusions could be drawn from them.

| **Model** | $T_1$ | $T_2$ | $T_3$ | $T_4$ |
|---|---|---|---|---|
| Robot 3D | 0.5100 | 0.1600 | 0.0900 | 0.0600 |
| Robot 2D | 0.5400 | 0.1800 | 0.1000 | 0.0700 |
| OpenSees | 0.5301 | 0.1736 | 0.1006 | 0.0725 |

**Table 4.3:** Natural periods for the four first modes computed using the different software.

### 4.4.1 Damping

Rayleigh damping has been chosen as damping model for the numerical model. This is because it is easily applied in OpenSees and have led to reasonable results when used together with distributed plasticity elements [53, 54]. Furthermore, anchoring at the reduced first mode frequency and T = 0.2 s was chosen, as suggested by Erduran [53]. The frequencies used to construct the coefficients in equation 2.7 are $\omega_i = 0.707\omega_1$ and $\omega_j = 31.4$ rad/s. The result is $a_0 = 0.1000$ and $a_1 = 0.00366$.

At first glance, using these suggestions which are based on results from analyzing steel structures, might seem inappropriate for concrete structures. However, these recommendations mainly tackle the issues with the mass and stiffness proportional damping. It is the damping ratio that considers material differences. In Table 11.2.1 in Chopra's book [14], it is shown that structures have much lower damping when in the elastic realm than when in the inelastic realm. The table suggests ratios from 2 to 5% for elastic concrete structures, but 7 to 8% for inelastic concrete structures. A ratio of 5% has been chosen throughout this work due to its use in both the literature and the EN 1998.

# Chapter 5

# Analyses and their results

## 5.1 Theoretical moment-curvature relationship

To establish a benchmark for moment-curvature relationships, an analysis of a zero-length element was done using the 500x500 column section. This procedure is thoroughly explained in the OpenSees wiki [61] which is the source for parts of the code used in the analysis. The procedure analyses the zero-length element under static loading. The axial load is constant and a moment is gradually applied to achieve a target ductility. All degrees of freedom (DOFs) were fixed at one element end, and only rotation and axial displacement were allowed at the other end. This analysis resulted in a moment-curvature relationship that can be used for comparisons of other results. The axial loads applied are approximately 0%, 5% and 10% of the total axial capacity. The results of this analysis are displayed in Figure 5.1.

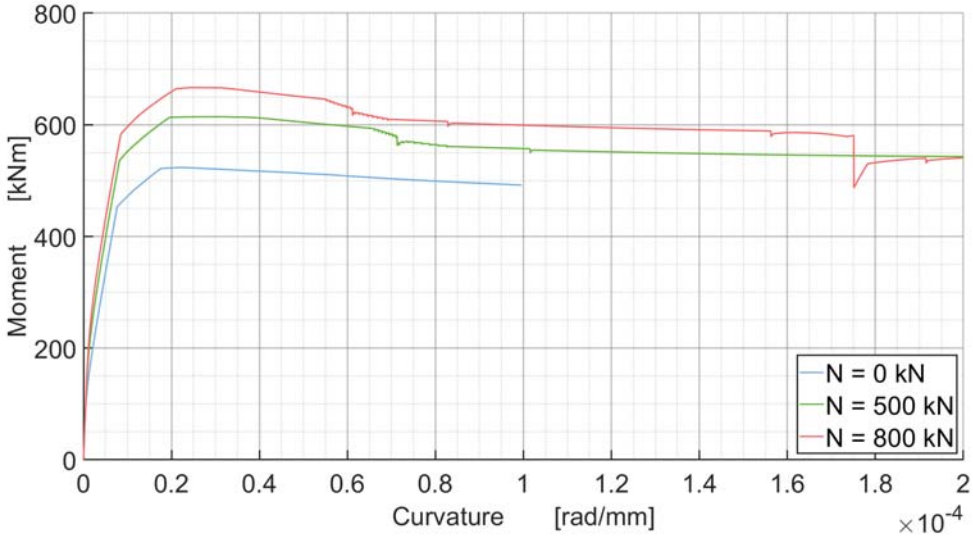


**Figure 5.1:** Theoretical moment curvature relationship for 500x500 section.

### 5.1.1 Control cantilever

Initially it was assumed that OpenSees automatically meshed each element. The results based on this assumption and the following MPA for the DB model showed unexpected results compared to other element models. To make sure that the issue was the meshing of

the elements, a simplified pushover analysis was performed on a cantilever using various numbers of DB elements with different number of IPs. The cantilever was identical in length and properties to the first-story column in axis 3. The different meshes subdivided it into 2, 4, 8, 18 and 24 FEs as shown in Figure 5.2. For each of these meshes, the number of IPs per FE was 2, 4, 8 and 10.

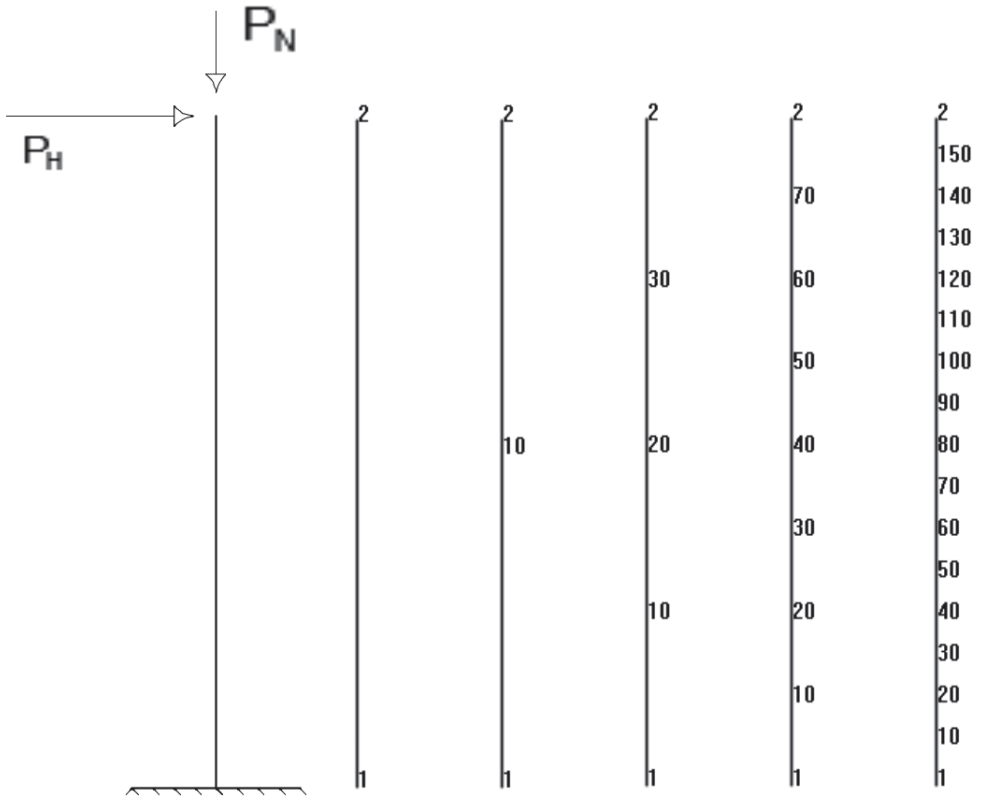


**Figure 5.2:** Control cantilever load configuration and different meshes.

The results are presented in Figure 5.3 in the form of moment curvatures for the section closest to node 1. It can be seen that the curvatures converge as the number of FEs increases. From the figure, it is evident that the results of the pushovers of the cantilevers modeled with eight or more FEs, converge. The figure also indicates that increasing the number of IPs does not produce more accurate results. The second model listed in the figure legend has more IPs than the third model. Despite of this, the third model, with more FEs, produces more accurate results than the second model.

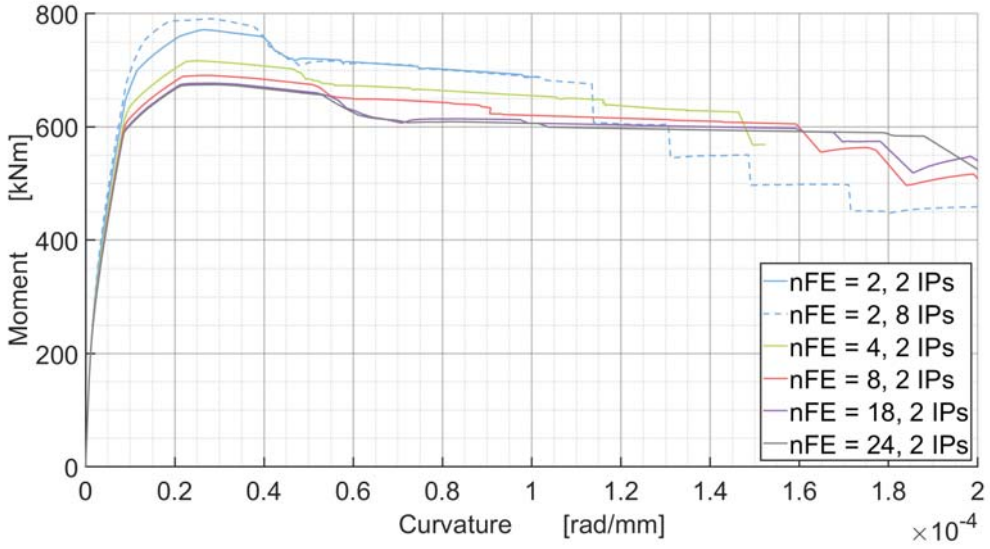


**Figure 5.3:** Moment curvature relationship for the first IP of the first FE in the control cantilever for the different number of FEs.

## 5.2 SPO

A SPO was performed to assess the behaviour of the structure and the different element formulations. The static pushover loads were applied to nodes along axis 3 in a vertical pattern based on the eigenvectors of the first mode, making this a first-mode pushover analysis (FMPA). These eigenvectors were calculated using OpenSees. P-$\delta$ effects are included in all analyses.

Analyses were done using the different element models: The DB element, the FB element and the BwH element. The numerical models using the different elements will be referred to as the DB model, FB model and BwH model respectively. Parameters were changed so that analyses were run using elements with different numbers of IPs, hinge lengths, member subdivisions and other relevant settings. Table 4.2 shows all the different element configurations that were analyzed by static pushover.

As stated in section 5.1.1, no meshing was done initially. The resulting plots showed that the element was misbehaving. After considering results from analyses of the control cantilever, it was decided that meshing was required, and analyses using different levels of mesh refinement were performed.

For simplicity, pushover loads were applied in the nodes along the center left column row (axis 3). It is also from these nodes the eigenvectors were ”sampeled”. The loads were scaled so that their relative magnitude were the same as for the eigenvectors of the first mode and so that their sum was equal to unity. The latter enabled easier interpretation of the output data because then the pseudo-time (load factor) was equal to the total base shear.

### 5.2.1 Results

Analyses of the DB model were performed using different meshes. The resulting capacity curve is shown in Figure 5.4. The results appear to converge to a stable solution as the number of FEs per member increases. As suspected from the coarsely meshed models using DB elements, the response is too stiff, apparently overestimating the peak base shear by 300 kN.

Performing the SPO using the DB element showed one of its severe disadvantages compared to the other elements - it has poor efficiency. One analysis using five IPs and 18 FEs took about five times as much time compared to the analysis of the model using FB elements. The efficiency could be improved for the DB model, but it would not be able to compete with the FB elements.

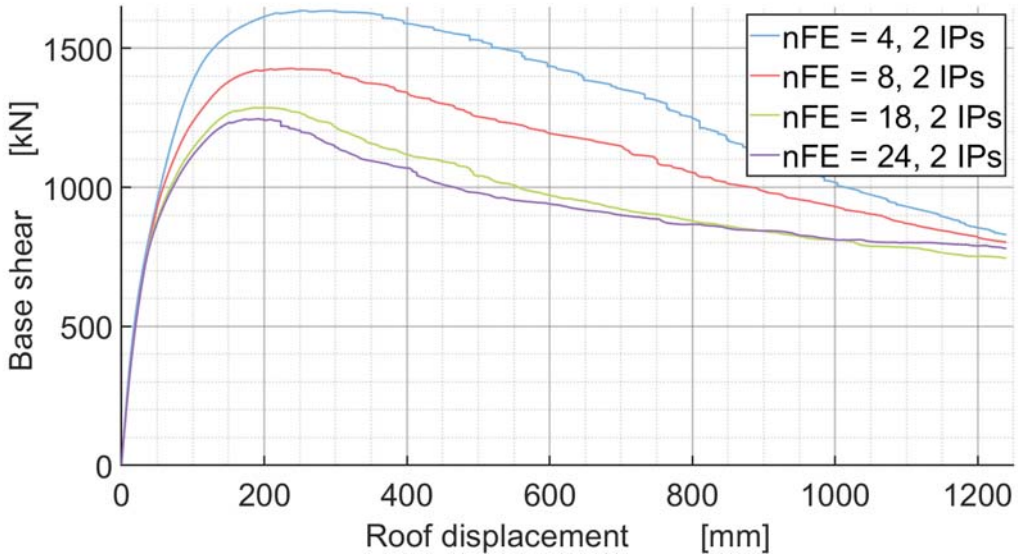


**Figure 5.4:** Base shear plotted against roof drift for different configurations of the DB model.

The response of the FB model is nonobjective (i.e. as the number of FEs increases, the different curves do not converge towards a stable solution). Figure 5.5 shows that increasing the number of IPs does not lead to a unique solution. Although it may seem like it does at first glance, the immediate post-peak response shows larger discrepancies as the number of IPs increases. Also, for the model using eight IPs, the solution fails to converge close to 700 mm.

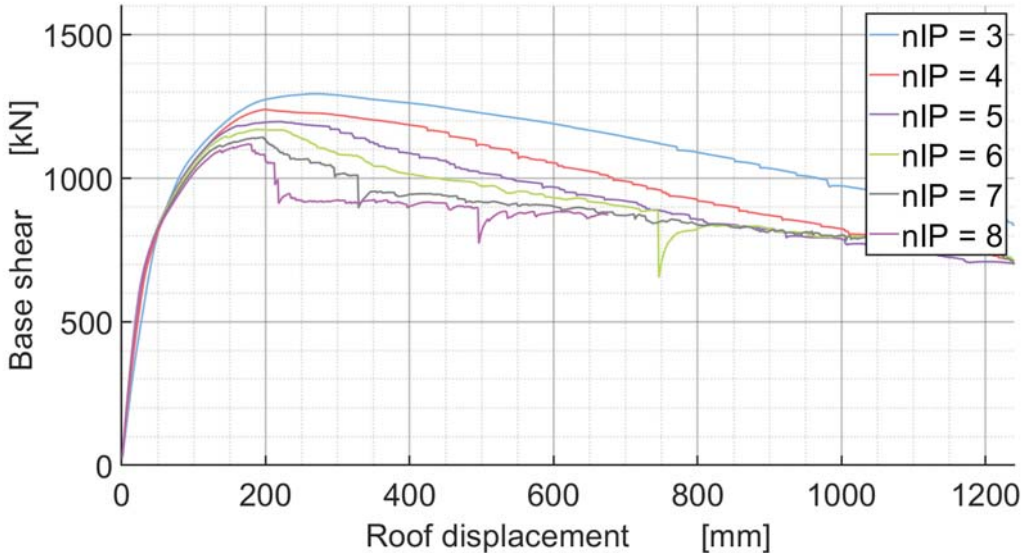


**Figure 5.5:** Base shear plotted against roof drift for different configurations of the FB model.

Using the BwH model, the results show similar responses for the different hinge lengths. This is shown in Figure 5.6. For a shorter hinge length, the peak base shear is reached sooner. It also has a softer post-peak response compared with those for larger hinge lengths. For the models where elements were defined with the inelastic fiber section in the interior, the response is generally softer. Note also that the model that used a hinge length of $l_p$ = 2.0 h with an inelastic interior, failed to converge at around 50 mm roof drift. The models using inelastic element interiors also displayed more similar pre-peak response.

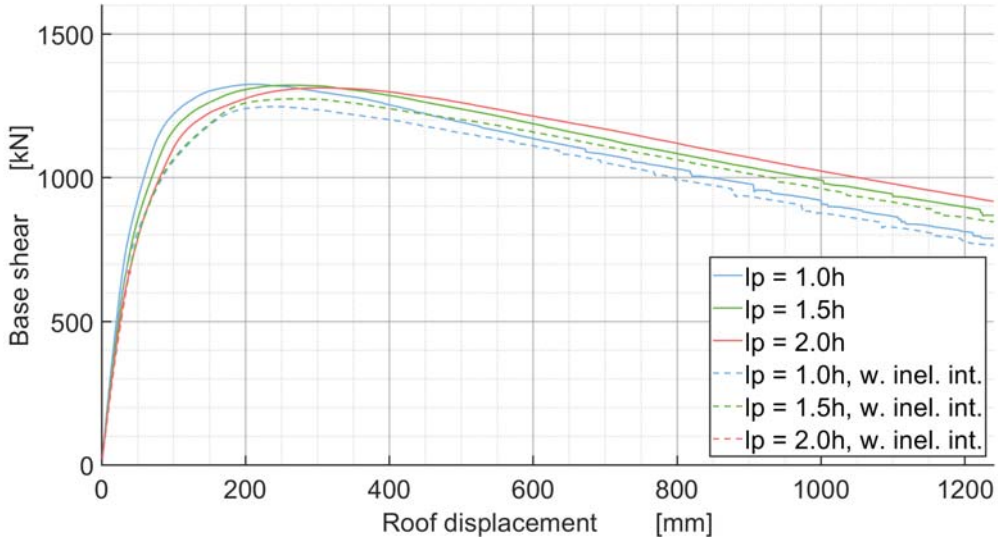


**Figure 5.6:** Base shear plotted against roof drift for different configurations of the BwH model.

Figure 5.7 shows a comparison between the different results for the different DB, FB and BwH model configurations. First of all, the initial stiffness is pretty much identical for all of them. The first model to soften is the FB model using eight IPs, which when compared with the others seems to be nonobjective. The DB model follows shortly thereafter, and has a considerably softer post-peak response than the other seemingly objective configurations. The BwH model using $l_p$ = 1.5 h and the FB model using three IPs, show very similar results, and appear to be well-behaved.

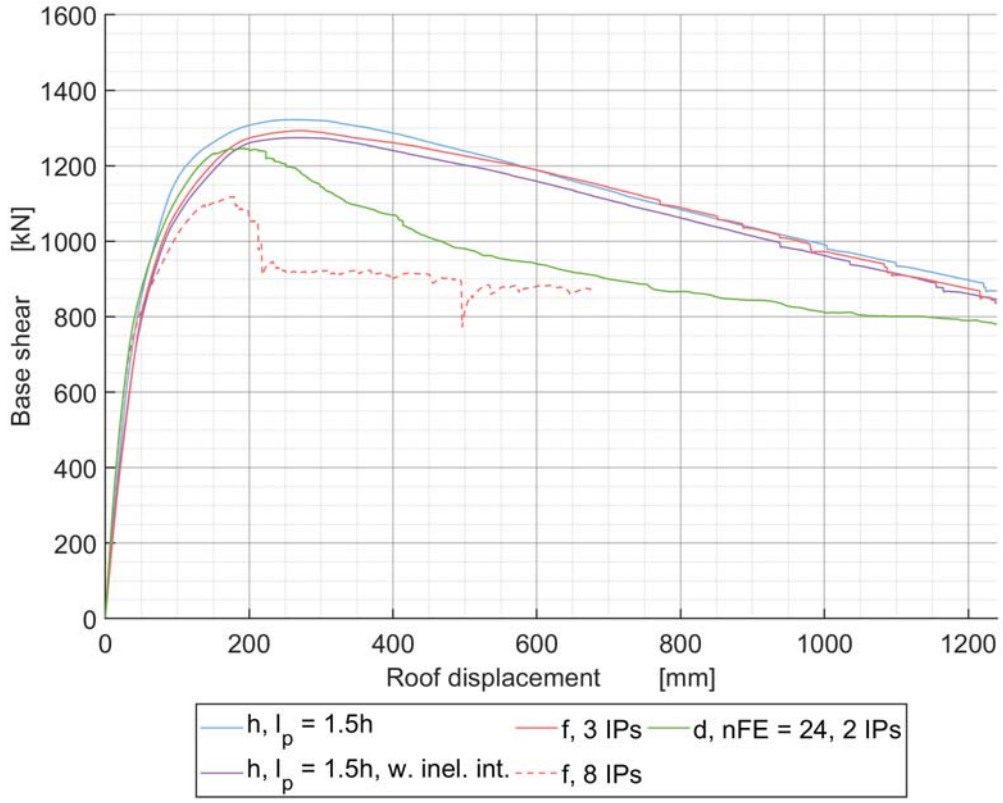


**Figure 5.7:** Base shear plotted against roof drift for selected configurations of the DB model (d), FB model (f) and the BwH model (h).

Figure 5.8 shows IDRs at 10% roof drift (1240 mm) for the BwH and FB model and their different configurations. This shows a very similar global response for both models in that the curves have the same pattern. For the different BwH model configurations, the responses can be seen as almost identical in Figure 5.8a. The most noticeable difference between them is that for the models using an inelastic interior, the displacements are more biased towards the lower stories. The same is the case for the FB model when using the largest number of IPs. Figure 5.8b shows that for six or more IPs, the solutions differ considerably from when five or less IPs are used. This also shows a less ”gradual” development than what can be seen in Figure 5.7.

Figure 5.9 shows the IDRs for the three different models at various roof drifts. From the IDR profiles at 2 and 4% roof drift, it can be seen that the three different models start out with very similar response. As the roof drift increases, the DB model starts displaying bias towards the lower stories. For 10% roof drift, larger differences than those observed in the capacity curves can be seen between the BwH model and the FB model using the selected configurations. The DB model has a softer response at the lower stories compared to the others.

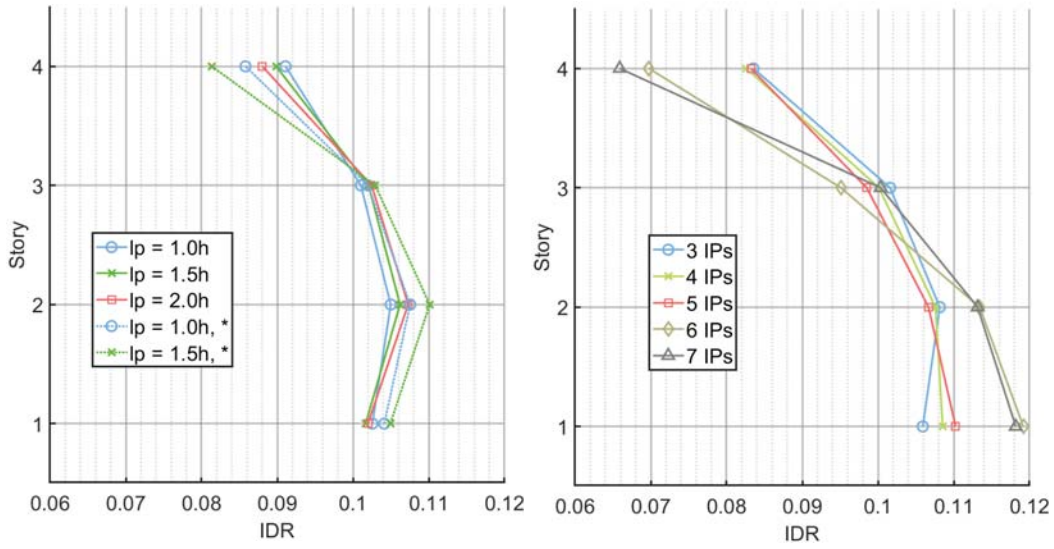


**(a)** BwH **(b)** FB beam-column

**Figure 5.8:** IDRs at 10% roof drift for different element configurations. *) Inelastic interiors are being used.

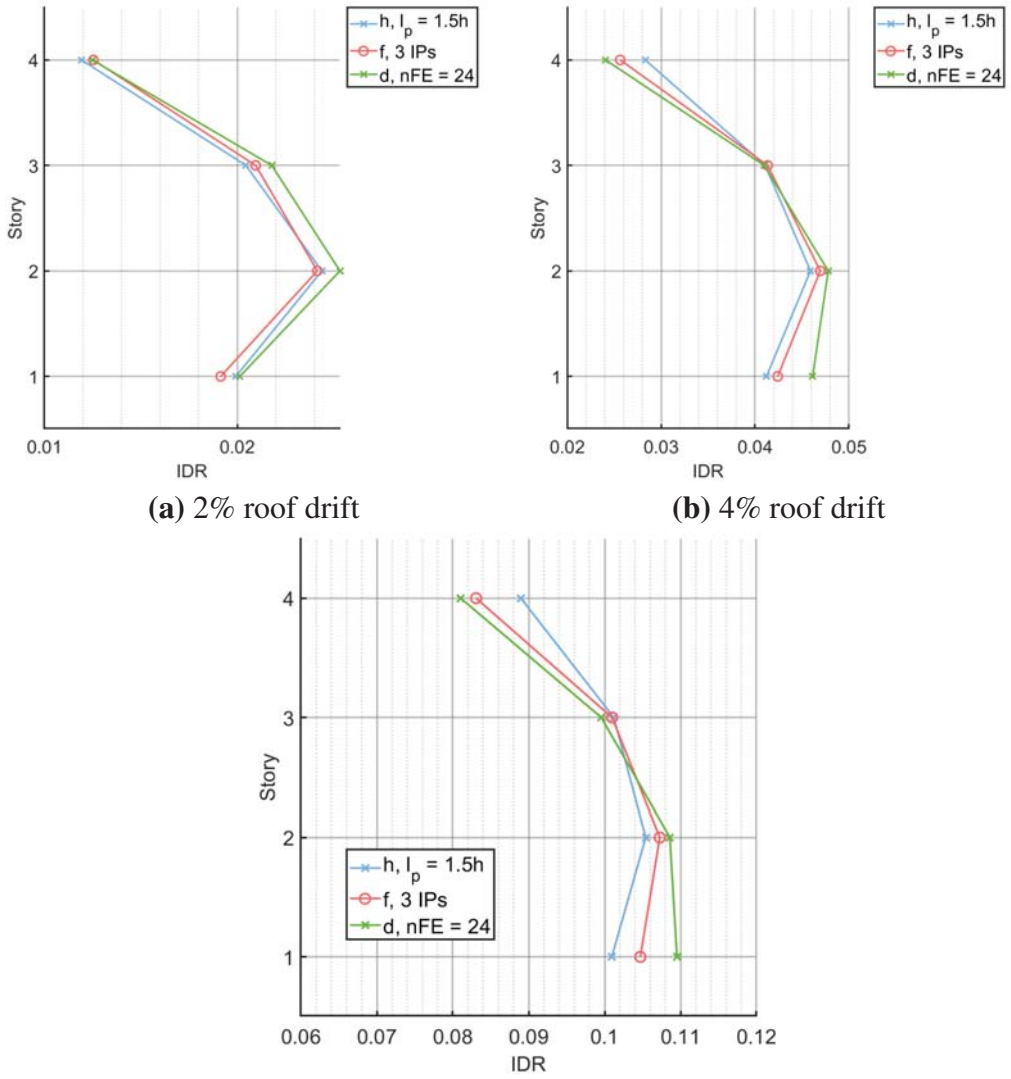


**(a)** 2% roof drift

**(b)** 4% roof drift

**(c)** 10% roof drift

**Figure 5.9:** IDRs for different element configurations at various roof drifts.

Moment-curvature relationships are also of interest. In the following moment-curvature relationship plots in Figure 5.10 and 5.11, the monitored IP is the bottom one (first) in the first-story column along axis 3. First, the relationship for the BwH element in Figure 5.10 should be mentioned. It shows an identical moment-curvature relationship for all element types.

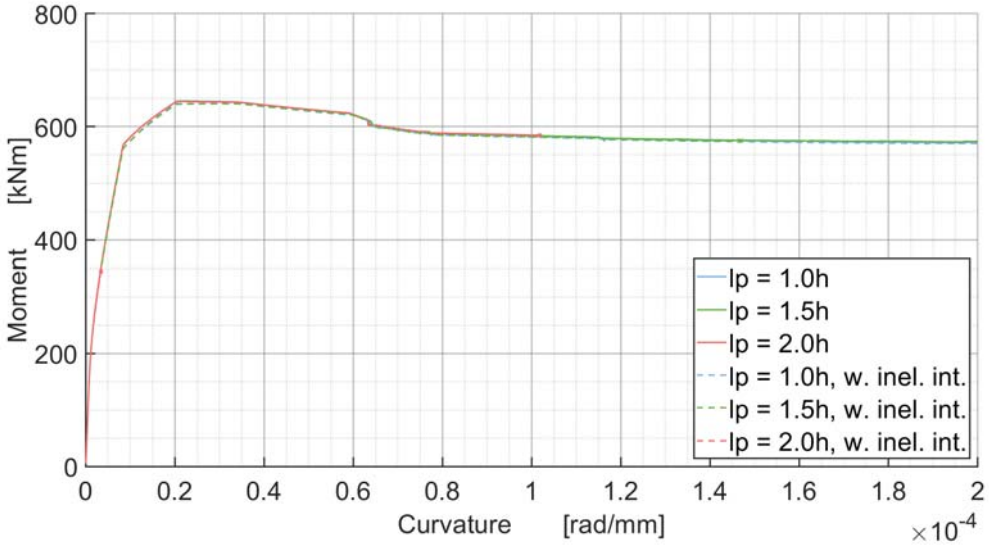


**Figure 5.10:** Moment-curvature relationship for the BwH model configurations.

Moment-curvature relationships for the two other models using the FB elements and the DB elements do not give more insight than the comparative plot in Figure 5.11. All curves for the FB elements using three to eight IPs overlap. Both the FB, DB and BwH element with or without inelastic interior have similar softening behaviour. What is not evident from this figure is that some of the curvatures are nonobjective.

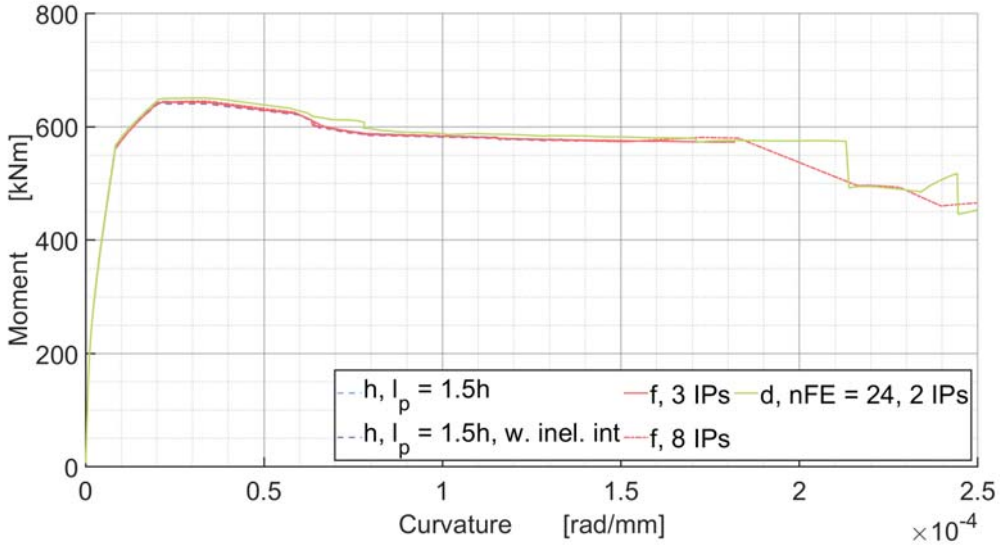


**Figure 5.11:** Moment-curvature relationship for selected configurations of the DB model (d), FB model (f) and the BwH model (h).

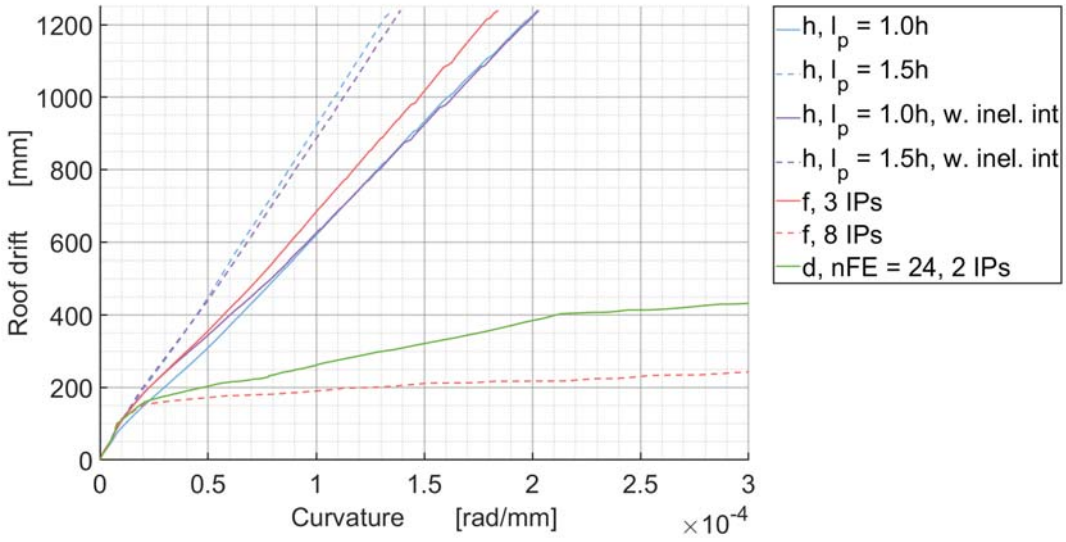


**Figure 5.12:** Roof drift plotted against the curvature in the monitored section.

The roof drift is plotted against the curvature at the control IP in Figure 5.12. This plot illustrates how some of the model configurations give nonobjective curvatures. Previous plots show that all models enter the plastic realm around the same roof displacement (150 mm). It is also here the curvatures start to become nonobjective for some configurations. Elements with plastic hinge lengths 1.0 h and 1.5 h show steady development of curvature as the roof displace. This includes the FB element with three IPs (which effectively have a hinge length of approximately 1.1 h). The FB model using eight IPs and the DB model using 24 FEs however, diverge significantly. It is not apparent from the figure, but when the structure has reached a 10% RDR, the curvature is sampled as $1.3e^{-3}$ rad/mm for the DB element using 24 FEs. This is eight times the magnitude of the model using BwH elements with $l_p$ = 1.0 h.

## 5.3 NTHA

A NTHA was performed for each of the seven ground motion records listed in Table 5.1 for the different numerical models; in total 84 NTHAs. The records were randomly chosen by the author from a larger set of 30 records. This set was compiled by Øystad-Larsen, who, considering recommendations by FEMA (P695) [26], selected records based on the following criteria:

- Only horizontal far-fault records should be selected.
- Peak ground accelerations must be above 2.0 m/s$^2$.
- The shear wave velocity, $V_{s30}$, must be between 180 m/s and 360 m/s.
- Magnitude of earthquake must be above 6.5.

| RSN | Name | Year | Mag | Rrap (km) | $V_{s30}$ (m/sec) | PGA |
|---|---|---|---|---|---|---|
| 282 | Trinidad | 1980 | 7.2 | 76 | 312 | 0.22 |
| 720 | Superstition Hills-02 | 1987 | 6.5 | 27 | 206 | 0.33 |
| 1003 | Northridge-01 | 1994 | 6.7 | 27 | 309 | 0.64 |
| 1110 | Kobe Japan | 1995 | 6.9 | 25 | 256 | 0.25 |
| 4889 | Chuetsu-Oki Japan | 2007 | 6.8 | 33 | 315 | 0.37 |
| 5832 | Iwate Japan | 2010 | 6.9 | 31 | 248 | 0.40 |
| 6923 | Darfield New Zealand | 2010 | 7 | 31 | 255 | 0.47 |

**Table 5.1:** Ground motion records used for the analyses.

The records have been collected from the PEER NGA-West2 ground motion database [55]. Choosing the records randomly was done to prevent bias. The number of records reflects that at least seven records are demanded in EN 1998 [17], clause 4.3.3.4.3, in order to use the average response parameter in further design. Even though these analyses will not be used for design, this demand is adhered to since it is based on a statistical rationale. This makes discussion of mean values of the responses meaningful.

The response spectra based on the records were scaled to match the elastic response spectrum defined in EN 1998 [17] at the first natural period of the structure. Both unscaled and scaled response spectra are shown in Figure 5.13 and 5.14. The response of the structure is dominated by the first natural mode, hence scaling in this way is justified. The production of response spectra and the scaling of them were performed in Matlab. The Matlab script developed for this purpose is found in Appendix G. The resulting scale factors are listed in Table 5.2. Ground motion records were scaled by multiplying them with the scale factors. This was expected to bring the structure into the inelastic realm. The script provided by Cemalovic in his thesis [57] was used as a starting point for the Matlab script. Parts of page 3 and 4 in Appendix G are solely results of Cemalovic's work.

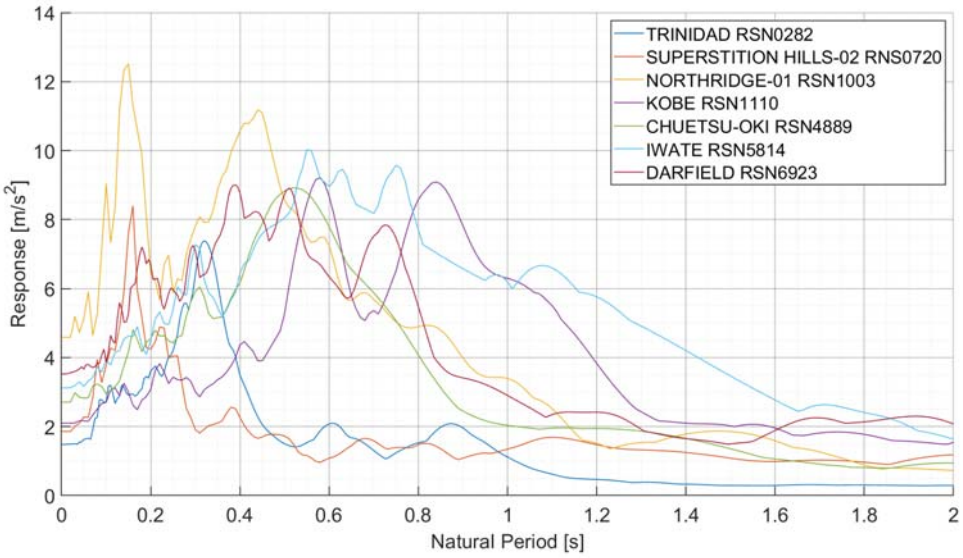


**Figure 5.13:** Unscaled response spectra.

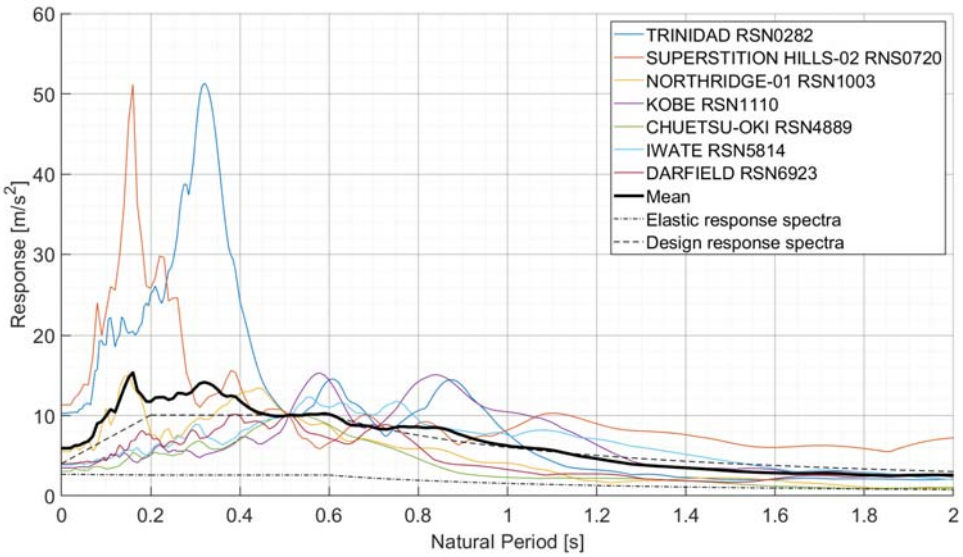


**Figure 5.14:** Scaled response spectra. Scaled to match the elastic spectrum in NS 1998 at $T_1$.

| RSN | Name | SF |
|---|---|---|
| 282 | Trinidad | 2,362 |
| 720 | Superstition Hills-02 | 1,882 |
| 1003 | Northridge-01 | 0,763 |
| 1110 | Kobe Japan | 1,666 |
| 4889 | Chuetsu-Oki Japan | 1,292 |
| 5832 | Iwate Japan | 1,121 |
| 6923 | Darfield New Zealand | 0,992 |

**Table 5.2:** Scale factors (SF) for the different ground motion records.

### 5.3.1 Results

The 84 NTHAs that were performed gave a large amount of output. Response histories showing RDR are given in appendices. The response history of the FB model is given in Appendix C. Results from the BwH model using elastic and inelastic interiors are shown in Appendix D and Appendix E, respectively. No NTHAs were performed using the DB model because it was found to be too time consuming. The response histories are presented together to show how they differ and to limit the number of pages. This results in some figures that are only able to give an overview of trends. In an attempt to give more detail, each response plot in Appendix D, E and C is accompanied with a magnified part of the same plot.

The results of the NTHAs for the Trinidad and Superstition Hills ground motions show somewhat odd responses. This seems to be due to the fact that the nature of these ground motions are peculiar. They are relatively short, but have large peaks distributed throughout. It is emphasized that although abnormal, they are regarded as valid in this work.

Of the total 84 NTHAs that were run, 16 failed to converge due to numerical instability. This is not always reflected by the presented figures, but should be considered when viewing them. Table 5.3 shows an overview of which failed to converge. All those that failed to converge did so before the structure reached significant roof drifts.

| Model | 282 | 720 | 1003 | 1110 | 4889 | 5832 | 6923 |
|---|---|---|---|---|---|---|---|
| BwH 1.0h el. int. | conv. | conv. | conv. | conv. | conv. | conv. | conv. |
| BwH 1.5h el. int. | conv. | conv. | conv. | conv. | conv. | conv. | conv. |
| BwH 2.0h el. int. | conv. | conv. | conv. | conv. | conv. | conv. | conv. |
| BwH 1.0h inel. int. | conv. | conv. | conv. | conv. | conv. | conv. | conv. |
| BwH 1.5h inel. int. | conv. | conv. | conv. | conv. | conv. | conv. | conv. |
| BwH 2.0h inel. int. | failed | failed | failed | failed | failed | failed | failed |
| FB 3 IPs | conv. | conv. | conv. | conv. | conv. | conv. | conv. |
| FB 4 IPs | conv. | conv. | conv. | conv. | conv. | conv. | conv. |
| FB 5 IPs | conv. | conv. | conv. | conv. | conv. | conv. | conv. |
| FB 6 IPs | failed | conv. | conv. | failed | conv. | conv. | conv. |
| FB 7 IPs | conv. | conv. | conv. | failed | conv. | failed | conv. |
| FB 8 IPs | failed | conv. | conv. | failed | failed | failed | failed |

**Table 5.3:** Analyses that converged and failed.

### The BwH models

The maximum roof drifts of the BwH models are presented in Figure 5.15 and Figure 5.18. For the model using elastic sections in the interior (Figure 5.15), the trend is that larger deformations are reached when using elements with longer plastic hinge lengths. The result of the analyses using Kobe ground motions is the exception. The time histories in Appendix D show that the differences in the results of the models apparent in Figure 5.15, are consistent throughout the entire response history. From the figures in Appendix D, it is evident that the model using $l_p$ = 2.0 h has a response that is usually larger than the others. In general, the models using $l_p$ = 1.5 h and $l_p$ = 2.0 h show similar development of period elongations and differences in amplitude. Figure 5.16 shows the maximum IDRs for the same cases as Figure 5.15, and the same trends are evident.

For most of the ground motions, the different hinge lengths seem to result in different dynamic properties of the models - they experience dis-synchronized beating. This is well illustrated in Figure D.8. From the 40-second mark, it can be seen that as the model using $l_p$ = 1.0 h starts responding with larger amplitudes, the one using $l_p$ = 2.0 h does the opposite.

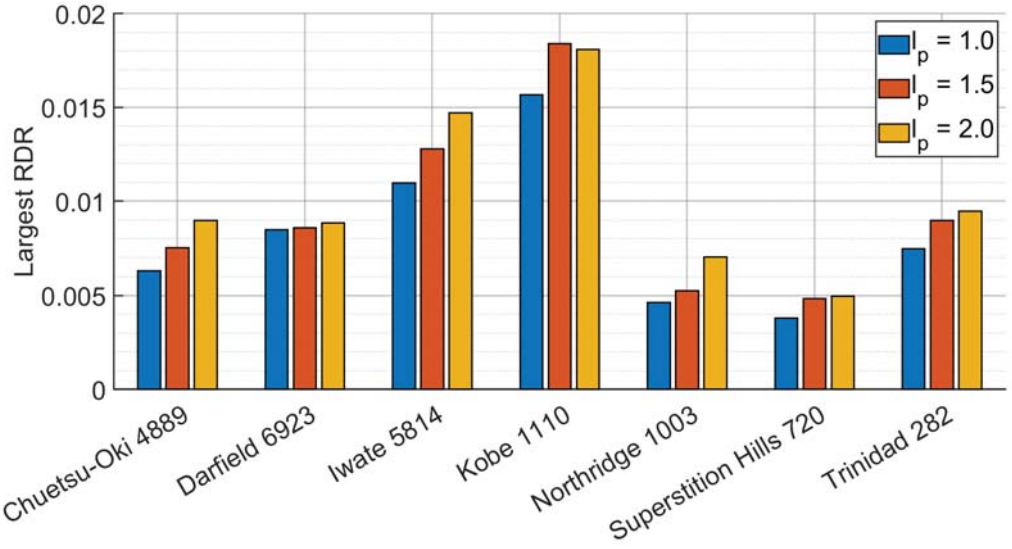


**Figure 5.15:** Maximum RDR for the BwH model using elastic interior.

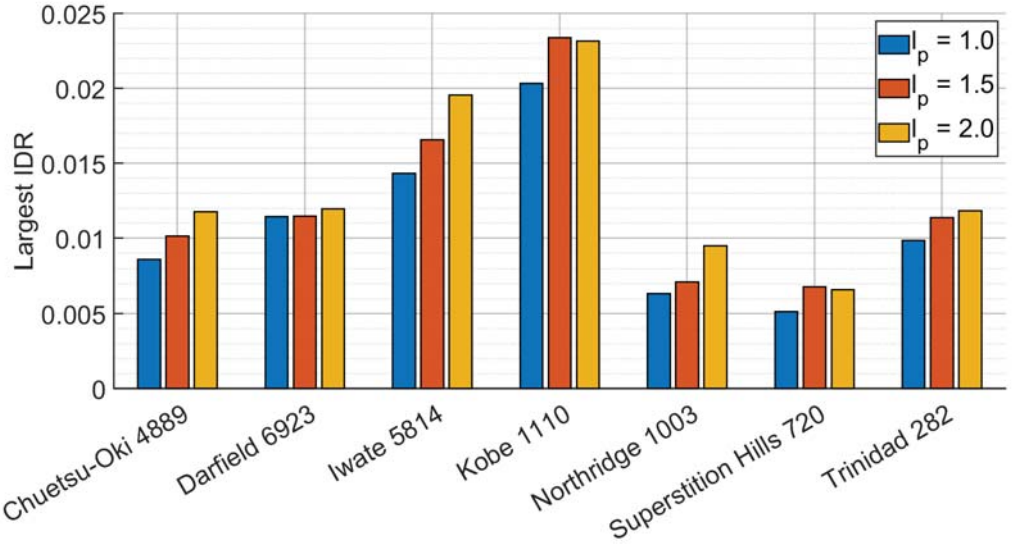


**Figure 5.16:** Maximum IDR for the BwH model using elastic interior.

The largest deviation can be found in the responses to the Chuetsu-Oki ground motions (Figure D.9). Smoothed, one-sided envelope curves for these response histories are presented in Figure 5.17 (for illustration purposes only). The first 24 seconds, the response of the different models are almost identical. At the 24-second mark, the first extreme roof drift cycle is reached, and after this the response of the different models diverge significantly. For the model with the shortest $l_p$, the response abate, while the response of the two other models continues to amplify. The differences of the three models become extreme after the initial cycles. Especially for the model using $l_p$ = 2.0 h, for which the response amplitudes

remain close to its maximum roof drift throughout. The model using $l_p$ = 1.5 h shows increased amplitudes around the 55-second mark.

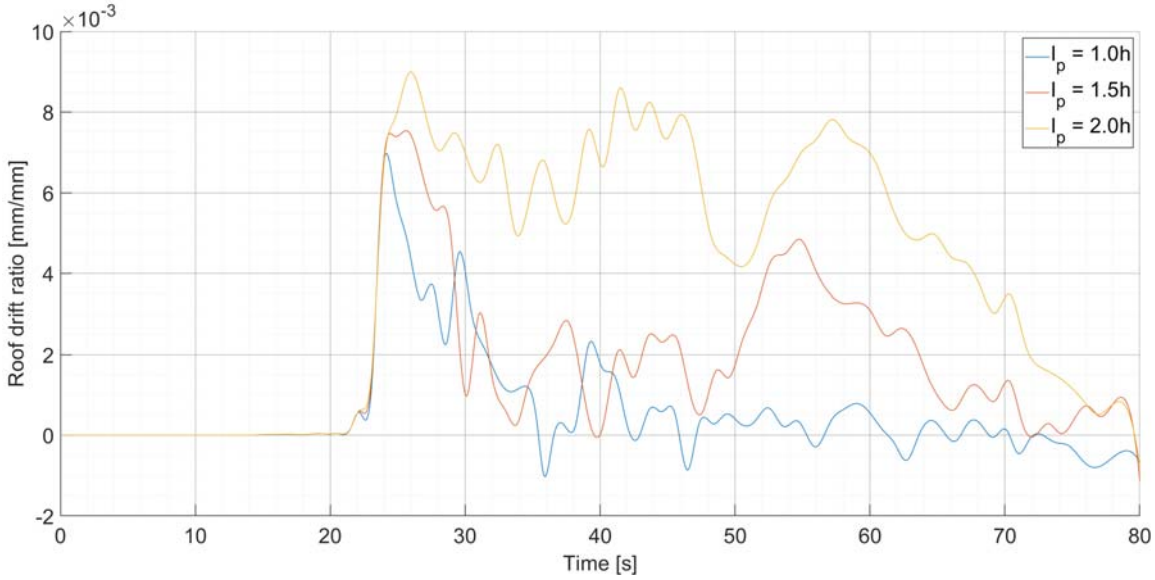


**Figure 5.17:** One-sided envelope curve of the roof displacement response histories for node 43. The responses correspond to the BwH models using elastic interior subjected to the Chuetsu-Oki ground motions. These curves are smoothed using spline interpolation separated by at least 50 samples. Much information is lost this way. This figure is for illustration purposes only. No conclusions of behavior are based on this figure.

Another noteworthy result can be observed in Figure D.2, which shows the response to the Trinidad ground motions. Here, the result starts to disagree around the 15-second mark. At this time, the two models using $l_p$ = 1.5 h and $l_p$ = 2.0 h separate from the one using $l_p$ = 1.0 h. What is interesting is that when this separation occurs, the model using $l_p$ = 1.0 h shows a rapid decrease in amplitude before an equally rapid increase.

In all the responses for the BwH models, period elongation is evident after the first cycles with large roof drifts. In relatively short time after these cycles, the different responses become dis-synchronized. It is also noteworthy that for some ground motions, the lines of equilibrium shift after plastic behaviour. This is best shown in the responses to the Superstition Hills ground motions, shown i Figure D.3. These shifts are different in magnitude for the different models.

For the models using a nonlinear fiber section in the element interior, the results are very similar to the ones using an elastic interior. The response histories for those with nonlinear interiors are found in Appendix E. Unfortunately, the analysis of these models using $l_p$ = 2.0 h failed to converge before any significant drifts were reached. All analyses using $l_p$ = 1.0 h and $l_p$ = 1.5 h did converge, and their results show the same trends for the same models using an elastic element interior. This can be seen in Figure 5.18 and 5.19.

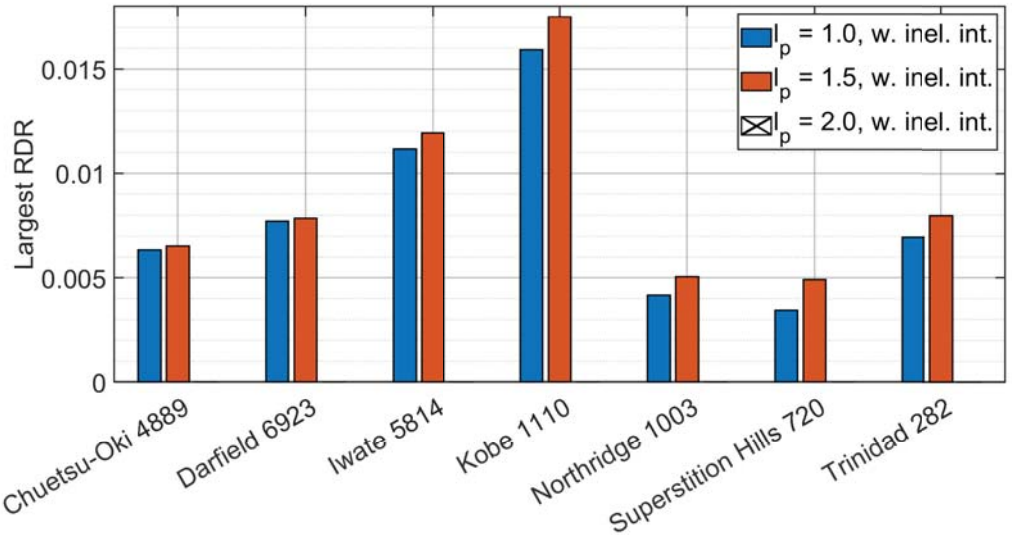


**Figure 5.18:** Maximum RDR for the BwH model using inelastic interior.

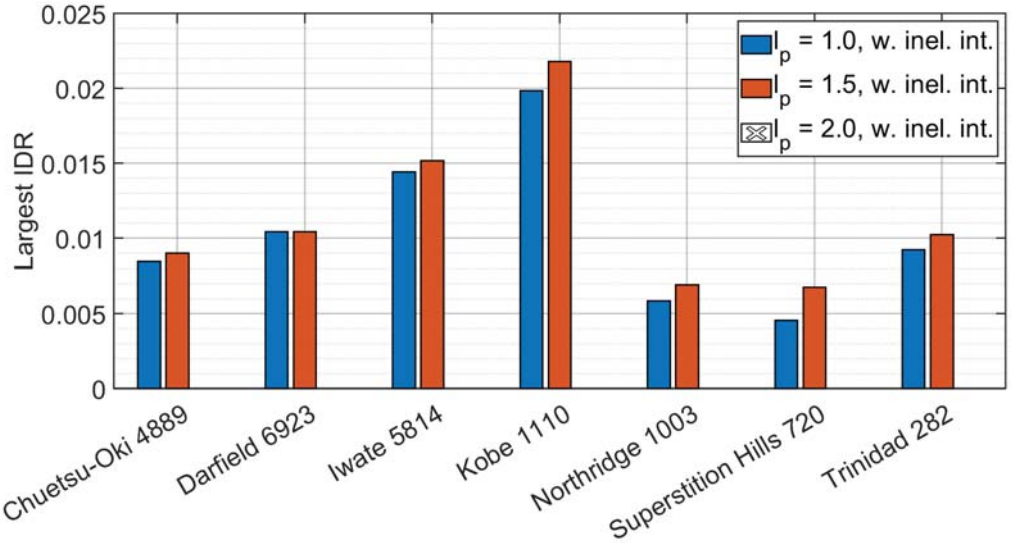


**Figure 5.19:** Maximum IDR for the BwH model using inelastic interior.

Figures 5.20, 5.21 and 5.22 show the RDR response histories for models using the same hinge length but with different interior sections. For all ground motion records except Chuetsu-Oki, the choice of interior sections has little effect on the roof drifts. Some differences are present towards the end of some response histories. As is seen in Figure 5.20 and Figure 5.21, there are small differences in response when using different interior sections. These plots are representative for all but the Chuetsu-Oki ground motion record. For the Chuetsu-Oki ground motion, large differences develop around the 52-second mark and disappear towards the end of the response history. For this type of comparison, only the

models using $l_p$ = 1.0 h and $l_p$ = 1.5 h were available, as the model using $l_p$ = 2.0 h with inelastic interior failed to converge.

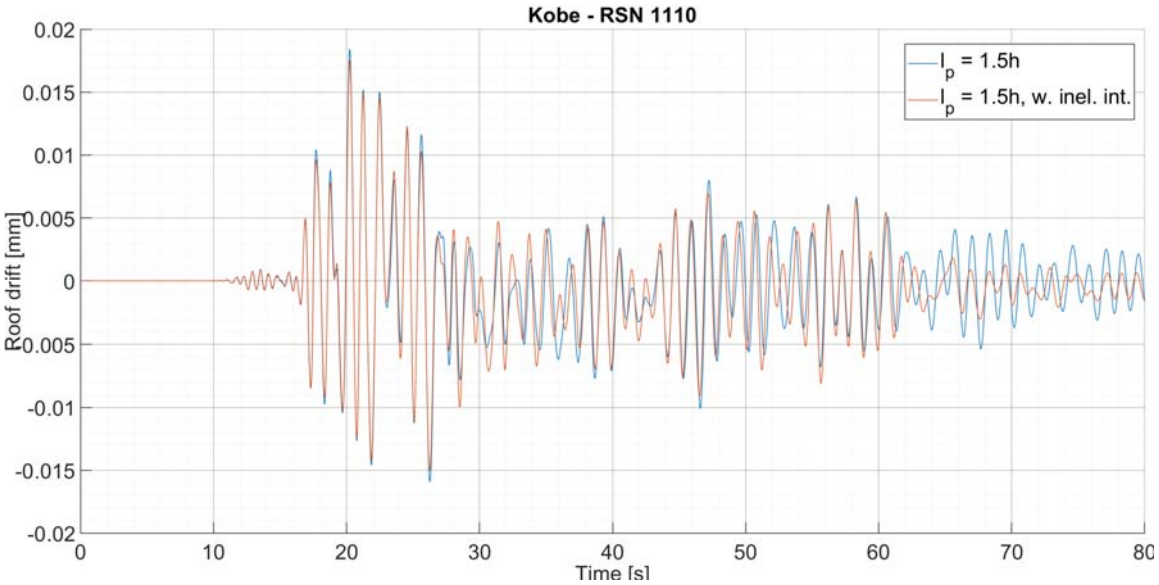


**Figure 5.20:** Response of the BwH models using $l_p$ = 1.5 h. Responses are for the Kobe ground motions.

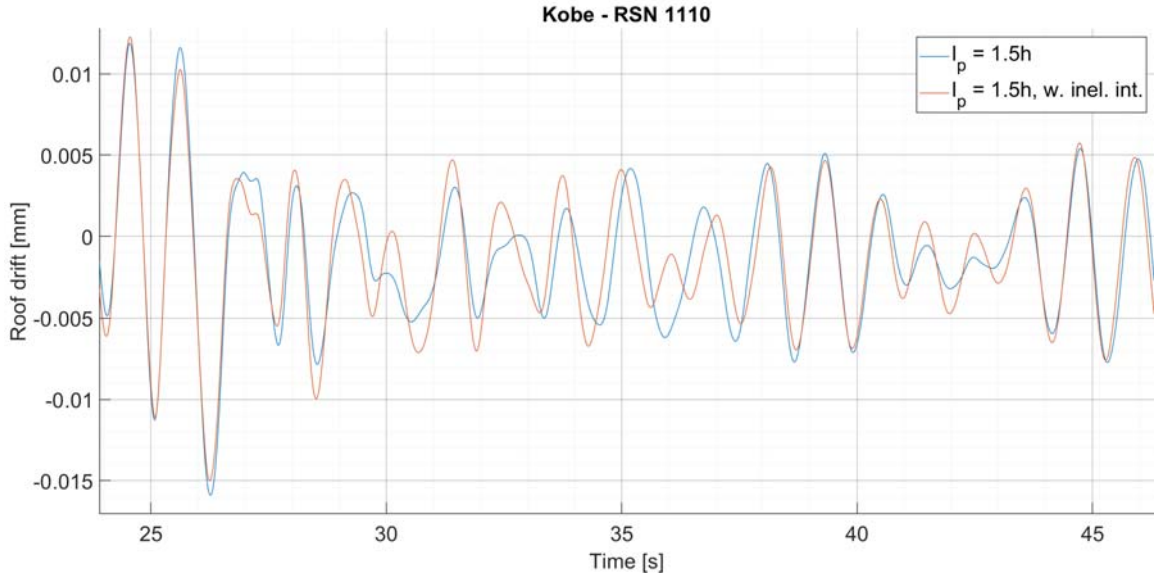


**Figure 5.21:** Response of the BwH models using $l_p$ = 1.5 h. This figure shows a magnified part of the response to the Kobe ground motions displayed in Figure 5.20.

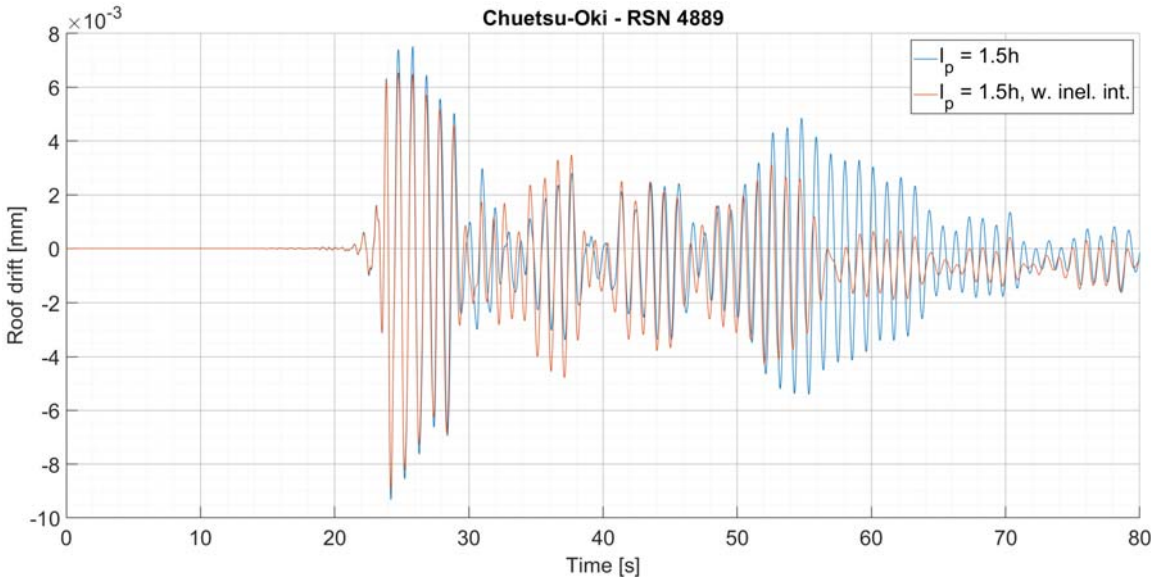


**Figure 5.22:** Response of the BwH models using $l_p$ = 1.5 h. Responses are for the Chuetsu-Oki ground motions.

### The FB models

The maximum RDRs of the FB model, using different element configurations, are summarized in Figure 5.23. The analyses that failed to converge have not been included. Here it is seen that increasing the number of IPs beyond five, appears to have little effect on the maximum displacements. The magnified plots of the roof drift response histories, given in Appendix C, show a slightly different trend. When increasing the number of IPs, the different responses appear to approach what can be characterized as an agreement. In some of the plots, it can be seen that when using five IPs, the response does not always agree with results obtained using six or more IPs. The roof drift response histories in Appendix C also show that the difference in amplitudes for the FB model is not as pronounced as for the different BwH models as the number of IPs is increased. Only for the Chuetsu-Oki ground motions do a significant difference in amplitude occur. When using three IPs, the response increases drastically after the 50-second mark. This is about the same time as was observed for the BwH model. Figure 5.24 shows the maximum IDRs for the same cases as Figure 5.23, and the same trends are evident.

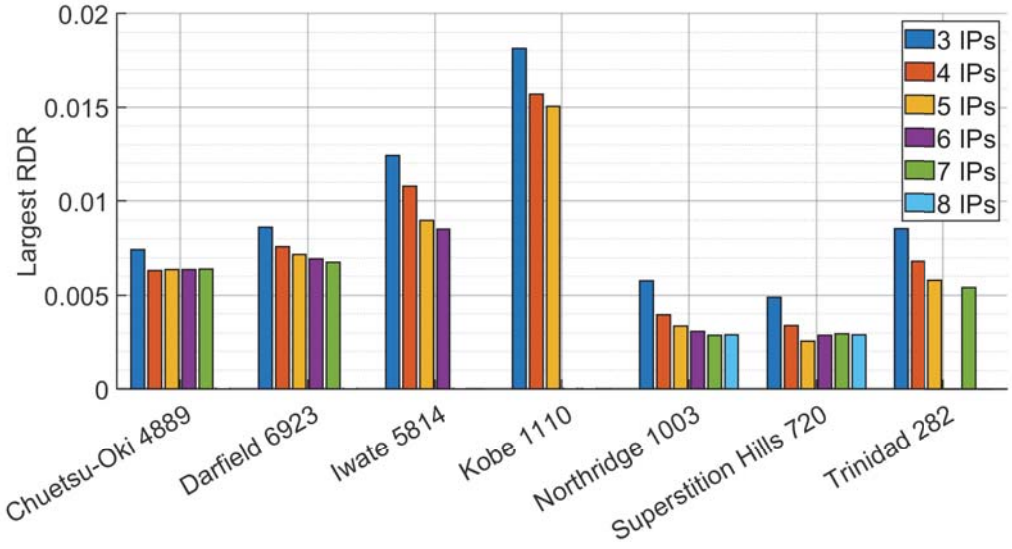


**Figure 5.23:** Maximum RDRs for the FB model.

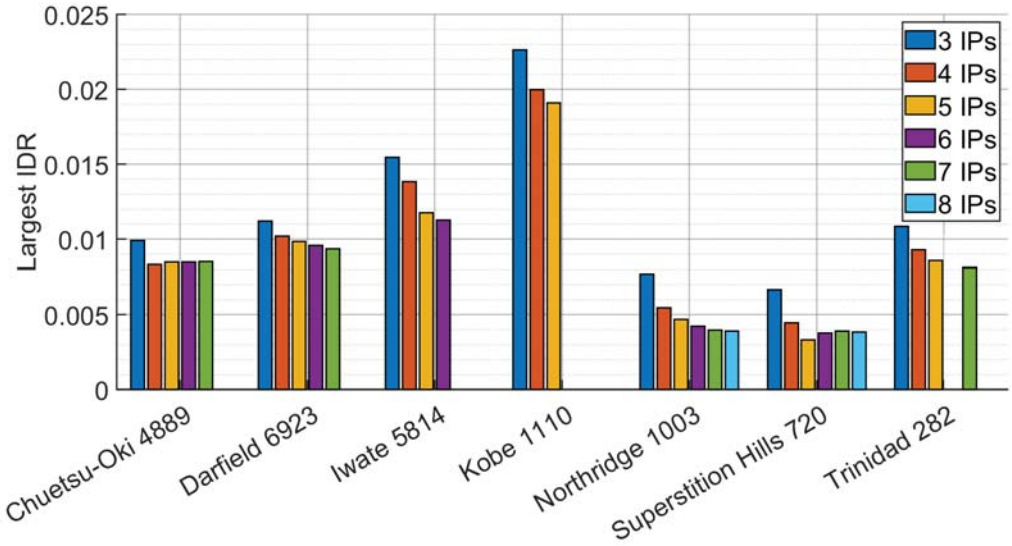


**Figure 5.24:** Maximum IDRs for the FB model.

### Overall trends for the FB model and the BwH model

Figure 5.25 shows an overview of the mean of the maximum RDRs and IDRs for the different model configurations. Numerical model configurations that did not converge have been left out to avoid discussion of means based on results from less than 7 ground motion records. The figure shows that the maximum IDR values are consistently larger than the maximum RDR values for the same models. Across the various configurations, the trends shown for the RDRs and IDRs are very similar. For both measures, it is evident that the peak responses decrease as the number of IPs increases for the FB model. For the BwH element,

longer hinge lengths leads to larger peak values for both RDRs and IDRs, regardless of the interior. For elastic interiors, the peaks are somewhat larger compared with results from models using inelastic interiors.

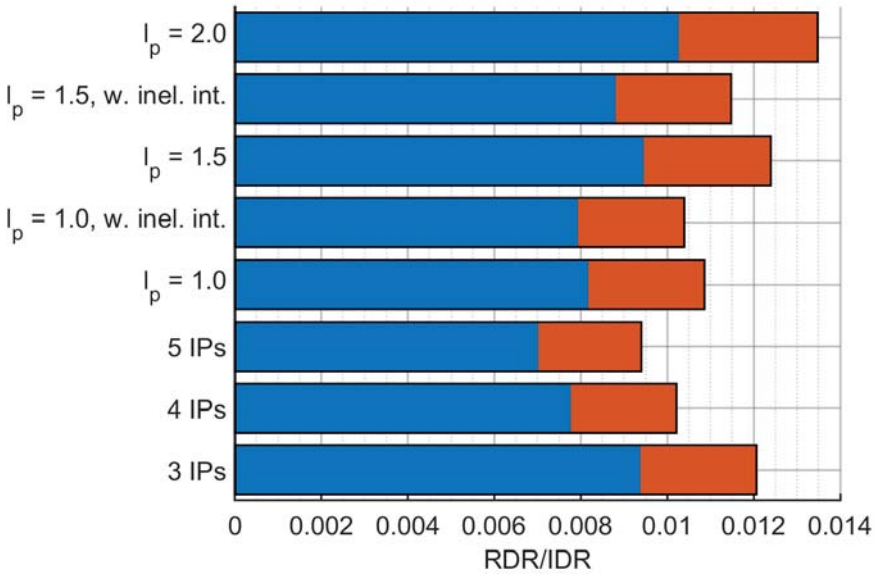


**Figure 5.25:** Mean values of RDRs and IDRs for the different numerical models. Blue bars represent RDRs while the values of the IDRs are represented by blue plus orange bars.

Figure 5.26 and 5.27 show the hysteresis curve of the curvature versus RDR for the Chuetsu-Oki and Kobe ground motions, respectively, for two different models: the BwH model using an elastic interior and a hinge length of 1.0 h and the FB model using five IPs. The response to the Chuetsu-Oki ground motions shows the typical difference between the two models, which is that the BwH model reach larger curvatures than the FB model. The response to the Kobe ground motions is more extreme and the differences in curvature between the models are larger. Here, the FB model shows significantly larger curvatures than the BwH model for negative roof drifts.

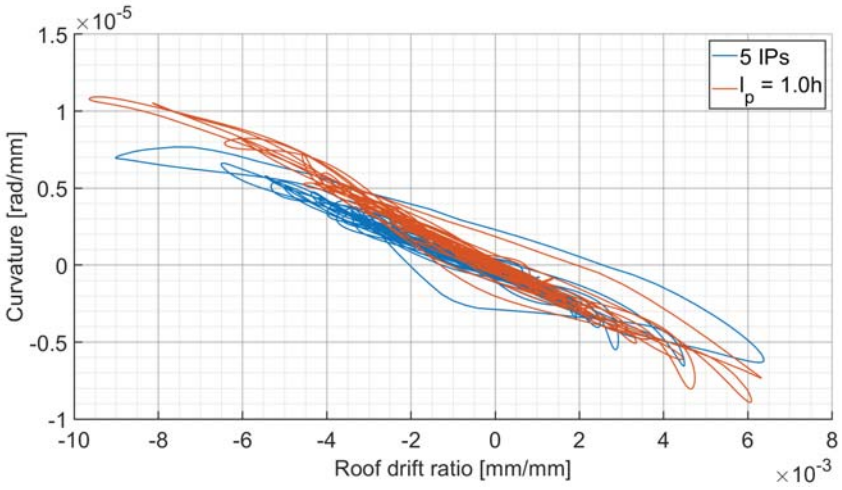


**Figure 5.26:** The RDR versus curvature for the FB model using five IPs and BwH model using $l_p$ = 1 h with an elastic interior. This is the response to the Chuetsu-Oki ground motions.

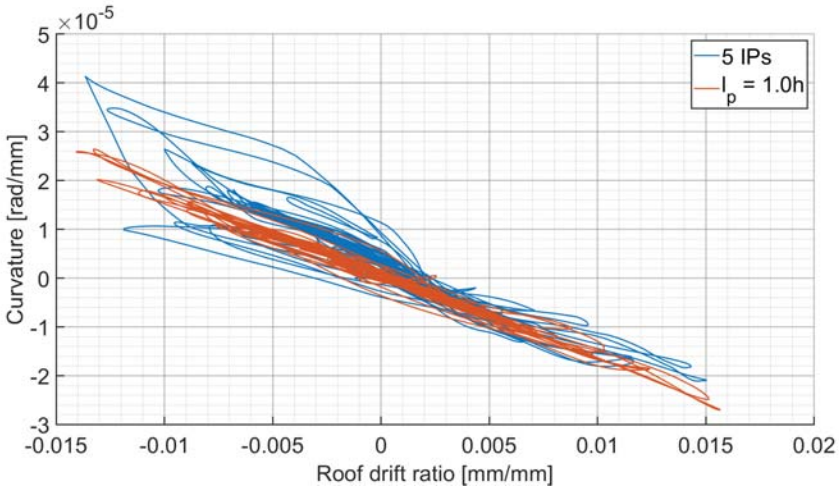


**Figure 5.27:** The RDR versus curvature for the FB model using five IPs and BwH model using $l_p$ = 1 h with an elastic interior. This is the response to the Kobe ground motions.

Figure 5.28 and 5.29 show plots of curvatures versus RDRs for selected time windows of the response to the Chuetsu-Oki and Kobe ground motions respectively. These time windows cover the oscillation where maximum roof drift occurs. As seen from the figures, there seems to be a reasonable agreement between the FB model using different numbers of IPs. This suggests that in this time span, no localization occurs. This is at least true for the Kobe response and parts of the Chuetsu-Oki response. At the bottom right in Figure 5.28, it can be seen that there are differences in roof drifts and curvatures.

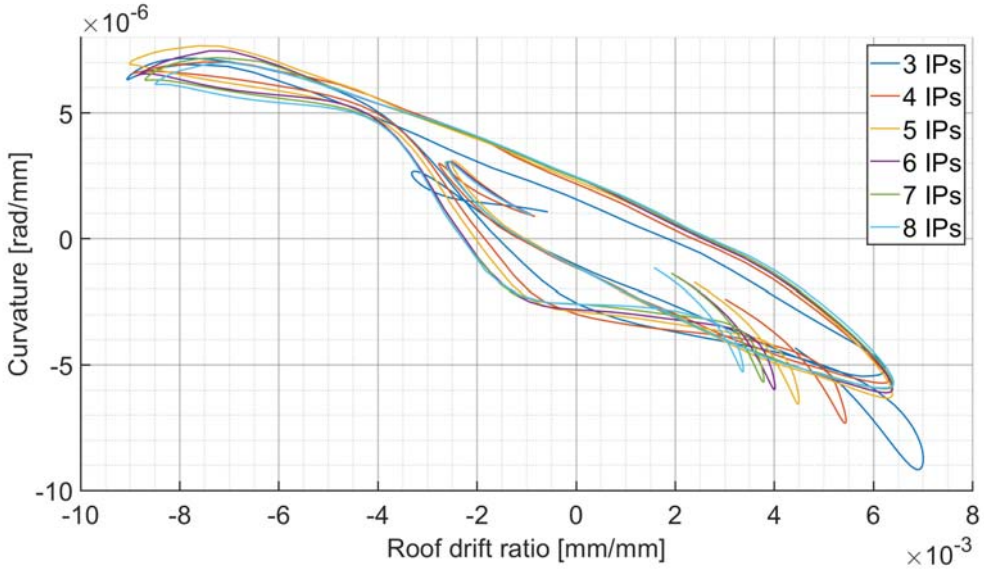


**Figure 5.28:** Curvature versus RDR for the FB model response to the Chuetsu-Oki ground motions. Curvatures are sampled at the first section (IP) in the first-story column in axis 3.

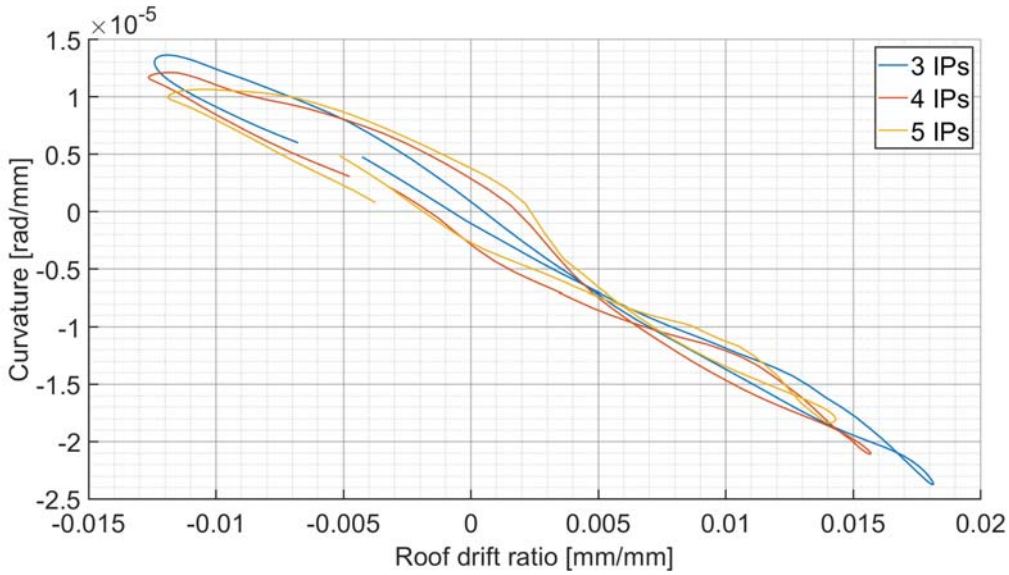


**Figure 5.29:** Curvature versus RDR for the FB model response to the Kobe ground motions. Curvatures are sampled at the first section (IP) in the first-story column in axis 3.

The plastic deformations of the elements were also recorded. Figure 5.30 and 5.31 show the plastic rotations of the base of the first-story column in axis 3 due to Superstition Hills and Iwate ground motions, respectively. For the Superstition Hills ground motions, which showed to give relatively small deformations, the model using three IPs estimates very different plastic rotations compared to the other model configurations. The plastic rotations

in the monitored base reach peaks with magnitude three times larger than those of the surrounding peaks resulting from using more integration points. For the Iwate ground motions, the differences between the responses are less profound.

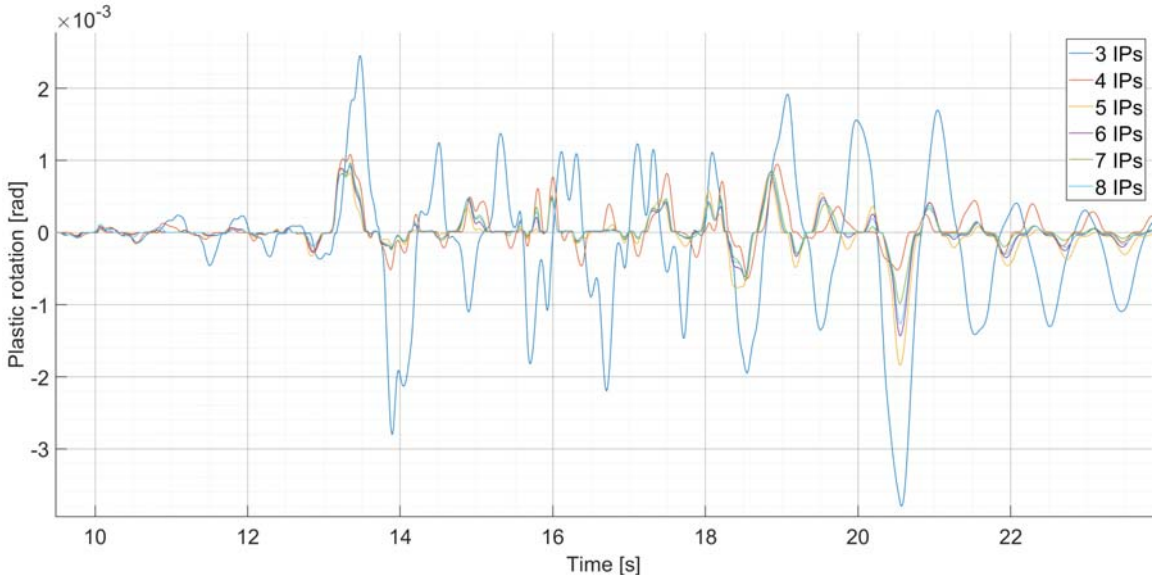


**Figure 5.30:** Part of the response history of the FB model to the Superstition Hills ground motions, showing total plastic rotations in the base of the first-story column in axis 3.

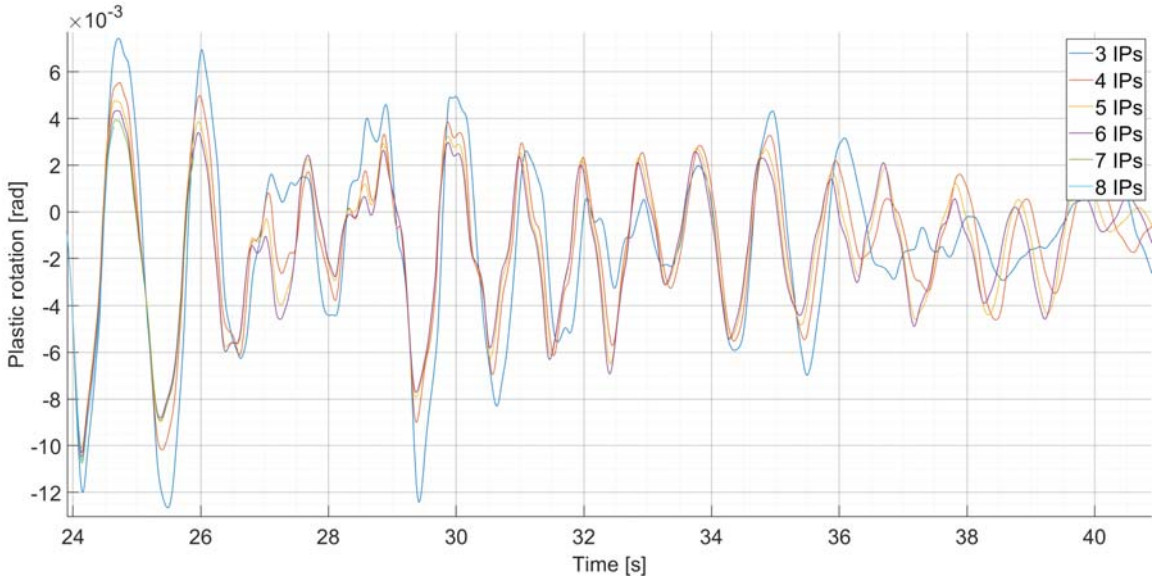


**Figure 5.31:** Part of the response history of the FB model to the Iwate ground motions showing total plastic rotations in the base of the first-story column in axis 3.

The plastic rotations at the top of the element were recorded as well. Figure 5.32 and Figure 5.33 show these rotations. They show very different response histories for the different FB

model configurations. As seen in the figure for the Iwate ground motions (Figure 5.33), the different model responses all coincide in the beginning of the excitation period. After about 32 seconds however, the model using three IPs starts to display almost zero plastic rotations where the rotations of the other models remain significant. For the Superstition Hills ground motions, the model using three IPs display very different plastic rotations compared with the ones using more IPs. Here, its rotations are larger.

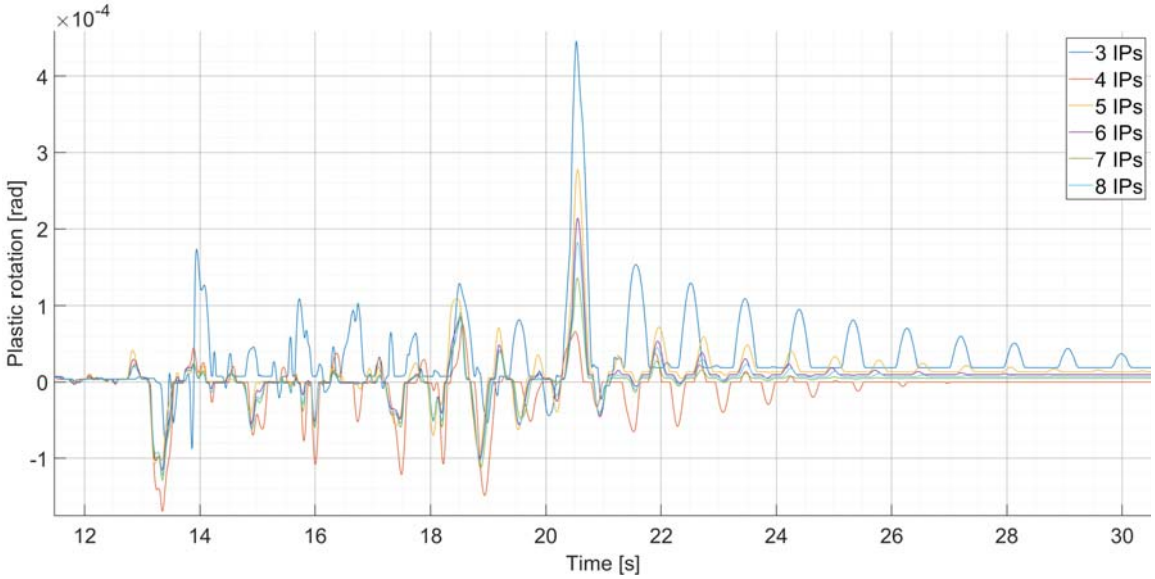


**Figure 5.32:** Part of the response history of the FB model to the Superstition Hills ground motions showing total plastic rotations in the top of the first-story column in axis 3.

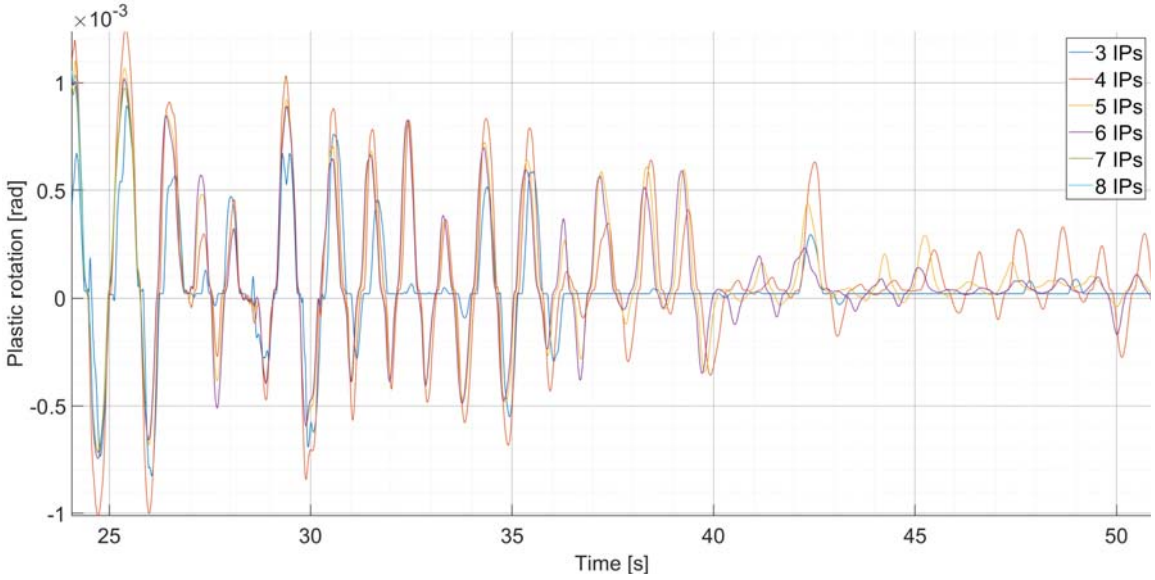


**Figure 5.33:** Part of the response history of the FB model to the Iwate ground motions showing total plastic rotations in the top of the first-story column in axis 3.

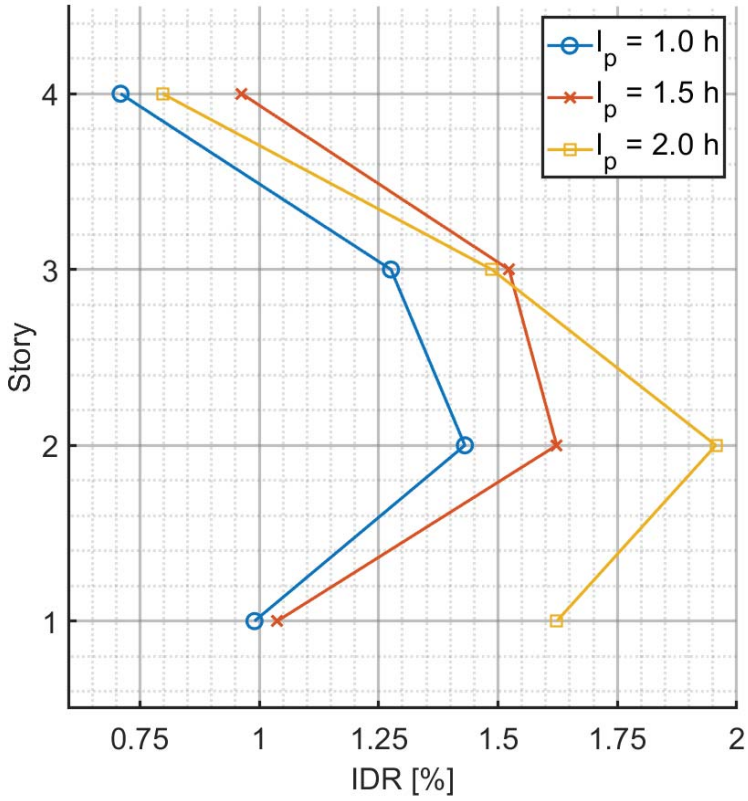


**Figure 5.34:** IDRs for the response of the BwH model using elastic interior to the Iwate ground motions.

IDRs for all the different model configurations and ground motions are shown in Appendix F. These display the IDR profile recorded at the same time as the maximum roof drift occurs. For the BwH model, it can be seen that for almost all ground motion records, the profiles corresponding to the different hinge lengths have the same shape. The exception is the response to the Iwate ground motions, where the model using $l_p$ = 2.0 h shows a larger bias towards the lower stories. The IDR plot for this ground motion is provided in Figure 5.34.

The IDRs for the FB model presented in Appedix F, show similar profile shapes. As were seen for the time histories, the results seem to converge towards a stable solution as the number of IPs is increased.

# Chapter 6

# Discussion

## 6.1 Control cantilever

The analysis of the control cantilever was helpful to identify the reason for the unexpected results of the SPO of the DB model. It clearly showed that OpenSees does not automatically mesh DB elements as initially assumed. The results also showed trends that could lead to the conclusion that using more FEs than 18 might be unnecessary. When comparing the results from the cantilever to the behaviour of the DB model during the MPA, it appears that seemingly negligible errors accumulate in the large numerical model.

## 6.2 SPO

The results from Figure 5.4 show that four FEs per member are enough to achieve a satisfactory solution for the elastic response for the DB model, but when nonlinearities start to occur, the solution becomes too stiff. Using 24 FEs seems to give satisfactory results for the capacity curves. However, this model yielded nonobjective results. This was illustrated in Figure 5.12, displayed below for convenience (Figure 6.1). These results are consistent with those found by Calabrese et al. [11] and others [35]; for softening behaviour, increasing the number of DB elements leads to nonobjective curvatures. Also, as was showed by Calabrese et al. and confirmed in the results presented herein, the FB model shows nonobjective curvatures as well.

A regularization technique for the DB model was presented by Calabrese et al. [11], which was to set the length of the most strained FE equal to twice the hinge length. However, in the present work, the DB model was found to be inefficient compared to the FB models. Based on this fact, the author is in doubt whether it is worth considering the DB element for analysis of MRFs such as the one considered herein.

Figure 5.10, which displays the moment-curvature relationships for the BwH model, shows results consistent with expectations based on knowledge presented in section 2.4. Because the characteristic length of the IP gets shorter, it must give higher values of curvature to produce the same displacements. The differences between the BwH model configurations are significant. Considering that the curvature is used as a control measure, for example $1.5e^{-4}$ rad/mm, the difference between the final roof drifts is large (approximately 290 mm).

The FB model's post-peak response was nonobjective. This is shown in Figure 6.1. It was only the model with three IPs that had a seemingly objective response. These results are

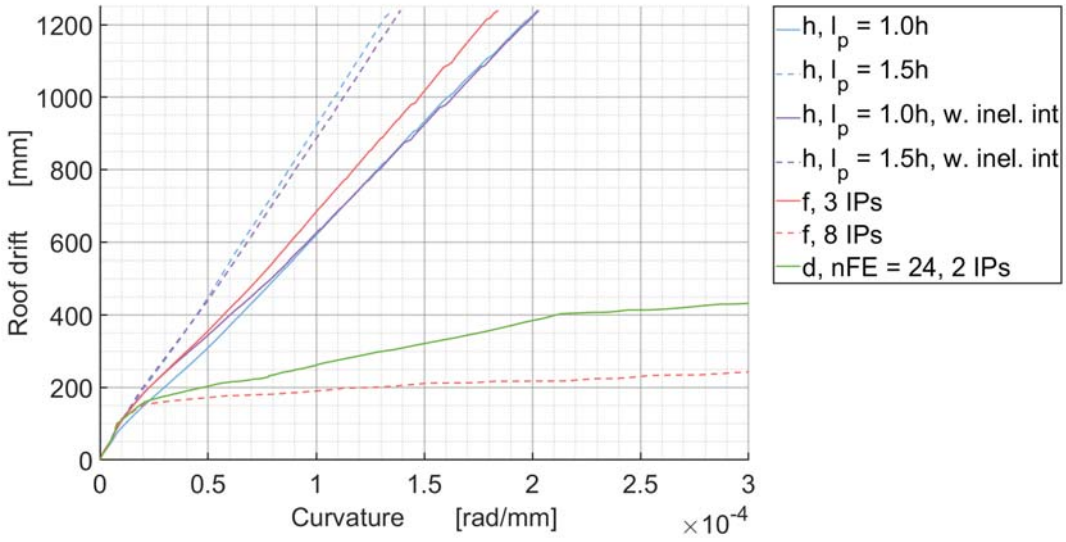


**Figure 6.1:** Roof drift plotted against the curvature in the monitored section.

also consistent with those of Calabrese et al. [11]. Because of the softening response, the curvatures localize in the first IP. For the elements with many IPs, the critical length (length of integration) for all IPs is short. For the IP where the curvature localize, these lengths are too short because the curvatures must reach extreme magnitudes in order to compute the same level of displacement. For the FE using three IPs, the critical length is 0.333L/2 which is approximately 570 mm [39]. This length is close to both $l_p$ = 1.0 h = 500 and $l_p$ = 1.5 h = 750, but closest to the former. This can be seen in Figure 6.1, as the line of the FB model (with three IPs) leans more towards the BwH using $l_p$ = 1.0 h.

The differences seen in curvature responses of these models have direct implications for the measure of damage in the structural elements. It shows that when using a shorter hinge length than whatever may be correct, the assessment of damage will be non-conservative. Also, if a larger hinge length is used, the assessment may be overly conservative. As curvature is a common DM in methodologies in building codes, these findings are important.

## 6.3 NTHA

The results from the NTHA show that using different hinge lengths or different number of IPs yields different results. Figure 5.25 shows the mean values of the maximum roof drifts, and it is evident that the FB model using three IPs reach similar values as the 1.5 h BwH model. This is interesting since this FB model also showed similar response to the BwH models in the SPO.

For the BwH models, the differences between the response amplitudes for models using different hinge lengths were significant, no matter which interior sections were being used. Not only did the maximum values differ, but the response amplitudes were consistently larger for larger hinge lengths throughout the duration of the response history. As stated

in the literature review, the main sources of structural damage are stress reversals and high stresses. The latter is more significant for low-rise buildings [16]. With this in mind, it would be natural to assume that if a numerical model using $l_p$ = 2.0 h were used in design, the damage due to cyclic stress reversals would be assessed as more pronounced.

A softer numerical model would give larger peak responses and have a larger natural period. If larger hinge lengths give a softer structure, this would explain the increased amplitudes. This means that these models should show longer periods. The results of the NTHAs show that this generally is the case. Not initially when the response is elastic, but after cycles where nonlinear response occur. Natural periods increase after significant deformations, some approaching 1 second. This shows that the different hinge lengths give different post-yield responses. The fact that the BwH model reach larger roof drifts, might result in more softening than the other models, causing the observed period elongation. The largest deviations were found in the responses to the Chuetsu-Oki ground motions (Figure D.9). The response shown by the model using $l_p$ = 2.0 h is so extreme that it cannot possibly be regarded as what could be expected of the physical structure. The periods visible in the response are not that different for those in other models, so extreme softening is not likely to be the cause. This shows that large hinge lengths may sometimes lead to a defective numerical model.

When considering the IDR plots for the BwH model in Appendix F, the differences are not that remarkable. However, the IDR plot for the Iwate ground motions (Figure 5.34) showed bias towards the lower stories for the model using $l_p$ = 2.0 h. The Iwate ground motions induce the second largest mean responses among the ground motions. What this plot might suggest is that for models using larger hinge lengths, a mechanism where displacements localize in the lower stories is reached sooner. Increasing the intensity of the ground motions would help shed light on this theory.

If the hinge lengths are so long that $8l_p > L$, the weights associated with the modified Gauss-Radau integration rules cover more length than that of the elements. This is the case for the columns when using $l_p$ = 1.0 h, $l_p$ = 1.5 h and $l_p$ = 2.0 h. This might seem like a numerical issue because the weights of the IPs in the interior, associated with the modified Gauss-Radau rules, overlap. However, as stated by Scott et al. [5], the integral that (in part) represents the elastic interior, is additive over its limits of integration (recall equation 2.3). This integral cancels out what has been integrated where the weights (critical lengths) overlap. Scott et al. [5] only address the use of elastic interiors. OpenSees allows inelastic sections to be used in the interior, but neither the wiki, nor any other source, explains how this operation is performed numerically.

When using $l_p$ = 2.0 h, the total weigh of one of the Gauss-Radau rules extends beyond the element length ($4l_p > L$). This could be the cause of the convergence issues when using this hinge length and inelastic interior. Because of the limited knowledge of which numerical procedures are used in this situation, it is difficult to confirm that this is the case. An investigation of the source code of the software or contacting its author, would be the next step. Nevertheless, the response shows that assumptions regarding hinge lengths can have profound effects on final results.

The results from the analyses using the FB models showed that there were large differences

in amplitudes, especially for the model using three IPs. The results also displayed that when increasing the number of IPs, the time histories seemed to converge towards one stable solution. Both the period elongations and the amplitudes decreased as the number of IPs was increased. As seen in Figure 6.2, the model using five IPs seems to give results that can be as satisfactory as the models with more IPs. The roof drift response histories do not support this observation. For some ground motions, this model also shows response that differs significantly from finer models (models using more IPs). The RDR histories do show that the trend is the same throughout the duration of the response - models using more IPs approach a stable solution. The IDR profile plots also show these characteristics. For the models using six IPs or more, the differences appear to be negligible. Based on these results it is argued that six or more IPs should be used. This is more IPs than what Neuenhofer and Filippou [37] recommended, which was four to six IPs.

With reference to Table 5.3, the use of six or more IPs seems to result in convergence issues for some ground motions. This suggests that the FB elements using less IPs have superior stability. In this thesis, the iterative form of the FB element was unfortunately not used. This form is expected to perform better, according to the OpenSees wiki [41], and will be accompanied with more computation for each element. With this in mind, it is advisable to use the iterative form of the element. If instability occurs, trying to use fewer IPs per element might be helpful, but it will come with the cost of less accuracy.

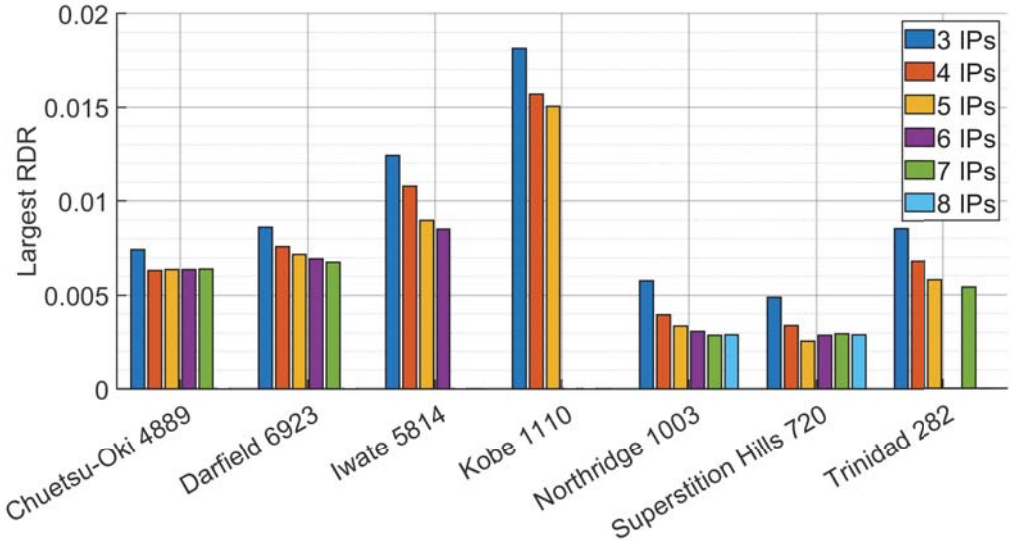


**Figure 6.2:** Maximum roof drifts for FB models.

The plots of the plastic rotations show that the apparent inaccuracy of the coarser FB models has large implications on this inelastic response measure. The results of the models using three and four IPs are significantly different compared to the responses of the finer models. For the model using five IPs, the plastic rotations are more consistent with the finer models, but the path and its magnitude diverge somewhat in some response histories. Again, results suggest that six or more IPs should be used.

These results have serious implications for assessment of the damage of the different models.

Since the inelastic response of the coarse models differs so much from others, the effects of cyclic degradation can be both over- and underestimated when using them. This may further lead to unconservative, or overly conservative, design decisions.

These findings could have been dismissed as erroneous if numerical softening behaviour occurred during the response. As seen in the SPO, when softening response occurs, increasing the number of IPs in the FB element does not lead to a unique solution. No indications of softening behaviour were found, suggesting that no such behaviour will occur during earthquake excitations for this structure, or that none of the excitations are intense enough to induce it. The latter seems most likely. In any case, FB model responses are reasonable and considered objective.

The DB model was not used in the NTHAs because it was computationally inefficient. It is the authors opinion that the use of the stiffness formulation is unsuitable for such analyses, compared to the much more efficient FB formulation. Although direct computational cost is an issue of the past in the context of seismic design, computational efficiency is still important.

In chapter 2.3.2, non-convergence was presented as a signal of global instability of the structure [27]. Obviously, it only signals instability of the numerical model, making this statement only true for ”perfect” models. Seeing this as ”true” collapse can therefore be problematic for any novice analyst with limited knowledge of how the different formulations are used. This fact should motivate learning and inspire diligence.

It may be reasonable to consider the uncertainties associated with the numerical model in design methodologies. Inaccuracies will always be inherent in numerical modeling, but the results show significant sensitivity to modeling assumptions. This must not be seen as an argument for allowing improper modeling to be accounted for. It was found that perfectly reasonable model configurations gave significantly different results. As an example, the assumed hinge lengths had remarkable effects on the resulting curvatures. This should definitively be considered by an analyst, but it may be legitimate reasons for this to be considered in design methodologies as well. This topic of discussion lies in the intersection between two subtopics. The first is how the effect of different hinge lengths affect the results from a numerical model. The other is how different hinge lengths are calculated using accepted methods and how they compare to experimental results. The latter is beyond the scope of this thesis, but the former topic is addressed here and results suggest that further study should be considered.

## 6.4 Further work

Over the course of this study, interesting topics have revealed themselves. It is also work that the author simply did not have time to do. Although geometrical nonlineareties (P-$\delta$ effects) are most decisive for high-rise buildings, it would be interesting to measure how these effects could change the measured responses. Also, increasing the intensity of the ground motion records in order to achieve larger plastic displacements could give additional insights.

Performing an IDA study of the response of different BwH models could give valuable information. The hinge lengths could be varied between, for example, 75 and 125% of a hinge length found using commonly accepted methods; for example equation 2.1. Such a study would give further insight to the significance of small changes to the hinge lengths, quantified using probabilistic measures. Realistically, there are such small changes (errors) in hinge lengths that it would be reasonable to expect when defining a numerical model for use in design. This would be an interesting topic for future study.

# Chapter 7

# Conclusion

The objective of this thesis was to investigate the effect of modeling assumptions. This has been achieved through analysis of a RC MRF using NTHAs and SPOs using different model configurations. Modeling assumptions have been shown to have large effects on the results of both NTHAs and SPOs. The same numerical model also shows different characteristics when analyzed using the two procedures. This is only natural, but the results have illustrated that it may be advantageous to perform both types of analyses.

The most significant result of the SPOs is that the recorded curvatures are sensitive to the critical lengths in the element for all models. Thus, when using curvature as a limiting DM, it is possible to over- or underestimate the actual damage if incorrect hinge lengths are used. It is concluded that when using curvature as a DM, extra attention should be paid to the estimation of the hinge lengths.

For the NTHA, plastic rotations were shown to differ when using the FB models. Using three IPs yielded what seemed to be erroneous results. The same could be seen from the time histories. Interestingly, using four or even five integration points seemed to lead to imprecise solutions. This suggest that it is advantageous to use six or more integration points, which is more than what is recommended in parts of the literature.

The different types of elements available to an analyst, be it DB, FB or BwH elements, have their limitations and potential pitfalls. The different results show that an analyst must be able to assess what kind of phenomena are occurring in the numerical model in order to assess the objectivity of the results. Because different assumptions lead to so different results, it may be reasonable to consider the uncertainties associated with the numerical model in design methodologies.

# Bibliography


[1] M. Fragiadakis et al. “Seismic assessment of structures and lifelines.” In: *Journal of Sound and Vibration* 334 (2015), pp. 29–56.

[2] N. Ning, W. Qu, and Z. J. Ma. “Design recommendations for achieving “strong column-weak beam” in RC frames.” In: *Engineering Structures* 126 (2016), pp. 343–352.

[3] L. Xie et al. “Experimental Study and Numerical Model Calibration for Earthquake-Induced Collapse of RC Frames with Emphasis on Key Columns, Joints, and the Overall Structure.” In: *Journal of Earthquake Engineering* 19.8 (2015), pp. 1320–1344.

[4] A. B. Liel, C. B. Haselton, and G. G. Deierlein. “Seismic Collapse Safety of Reinforced Concrete Buildings. II: Comparative Assessment of Nonductile and Ductile Moment Frames.” In: *Journal of Structural Engineering* 137.4 (2011), pp. 492–502.

[5] M. H. Scott and G. L. Fenves. “Plastic Hinge Integration Methods for Force-Based Beam–Column Elements.” In: *Journal of Structural Engineering* 132.2 (2006), pp. 244–252.

[6] P. Ceresa et al. “A fibre flexure-shear model for seismic analysis of RC-framed structures.” In: *Earthquake Engineering & Structural Dynamics* 38.5 (2009), pp. 565–586.

[7] D.-C. Feng and X.-D. Ren. “Enriched Force-Based Frame Element with Evolutionary Plastic Hinge.” In: *Journal of Structural Engineering* 143.10 (2017).

[8] C. Zeris, D. Vamvatsikos, and P. Giannitsas. “Impact of Fe Modeling in the Seismic Performance Prediction of Existing Rc Buildings.” In: *ECCOMAS Thematic Conference on Computational Methods in Structural Dynamics and Earthquake Engineering*. Rethymno, 2007.

[9] S. K. Kunnath and E. Erduran. *Pushover procedures for seismic assessment of buildings issues, limitations and future needs*. Tech. rep. Lisbon, Portugal, 2008, pp. 31–43.

[10] J. B. Mander. “Seismic Design of Bridge Piers.” Doctoral dissertation. University of Canterbury, 1983.

[11] A. Calabrese, J. P. Almeida, and R. Pinho. “Numerical Issues in Distributed Inelasticity Modeling of RC Frame Elements for Seismic Analysis.” In: *Journal of Earthquake Engineering* 14.sup1 (2010), pp. 38–68.

[12] N. Øystad-Larsen, M. Cemalovic, and A. M. Kaynia. *Investigation of Overstrength of Dual System by Non-Linear Static and Dynamic Analyses*. Tech. rep. Norwegian University of Science and Technology, 2016.

[13] OpenSees wiki. *The Open System for Earthquake Engineering Simulation*. 2006. URL: `http://opensees.berkeley.edu/OpenSees/home/about.php` (Cited 01/30/2018).

[14] A. K. Chopra. *Dynamics of Structures: Theory and Applications to Earthquake Engineering*. 4th ed. Essex: Pearson, 2014.

[15] A. M. Mwafy and A. S. Elnashai. “Static pushover versus dynamic collapse analysis of RC buildings.” In: *Engineering Structures* 23.5 (2001), pp. 407–424.

[16] Y.-J. Park, F. Ang, and Y. K. Wen. “Seismic damage analysis of reinforced concrete buildings.” In: *Journal of Structural Engineering* 111.4 (1985), pp. 740–757.

[17] Standard Norge. *NS-EN 1998-1 - Eurocode 8: Design of structures for earthquake resistance. Part 1: General rules, seismic actions and rules for buildings*. Lysaker, 2014.

[18] A. K Chopra. “MPA procedure.” In: *Dynamics of Structures: Theory and Applications to Earthquake Engineering*. 4th ed. Essex: Pearson, 2014. Chap. 20.7, p. 800.

[19] H. Krawinkler and G. D. P. K. Seneviratna. “Pros and cons analysis of seismic evaluation.” In: *Engineering Structures* 20.6 (1998), pp. 452–464.

[20] E. I. Katsanos, A. G. Sextos, and G. D. Manolis. “Selection of earthquake ground motion records: A state-of-the-art review from a structural engineering perspective.” In: *Soil Dynamics and Earthquake Engineering* 30.4 (2010), pp. 157–169.

[21] J. Hancock and J. J. Bommer. “A State-of-Knowledge Review of the Influence of Strong-Motion Duration on Structural Damage.” In: *Earthquake Spectra* 22.3 (2006), pp. 827–845.

[22] M. Raghunandan and A. B. Liel. “Effect of ground motion duration on earthquake-induced structural collapse.” In: *Structural Safety* 41 (Mar. 2013), pp. 119–133.

[23] R. Chandramohan, J. W. Baker, and G. G. Deierlein. “Quantifying the Influence of Ground Motion Duration on Structural Collapse Capacity Using Spectrally Equivalent Records.” In: *Earthquake Spectra* 32.2 (2016), pp. 927–950.

[24] D. Vamvatsikos and C. A. Cornell. “Applied Incremental Dynamic Analysis.” In: *Earthquake Spectra* 20.2 (2004), pp. 523–553.

[25] A. Azarbakht and M. Dolšek. “Prediction of the median IDA curve by employing a limited number of ground motion records.” In: *Earthquake Engineering & Structural Dynamics* 36.15 (2007), pp. 2401–2421.

[26] Applied Technology Council. “Quantification of building seismic performance factors.” In: *Fema P695* (2009).

[27] D. Vamvatsikos and C. A. Cornell. “Incremental dynamic analysis.” In: *Earthquake Engineering & Structural Dynamics* 31.3 (2002), pp. 491–514.

[28] A. B. Liel et al. “Incorporating modeling uncertainties in the assessment of seismic collapse risk of buildings.” In: *Structural Safety* 31.2 (2009), pp. 197–211.

[29] M. Fragiadakis, D. Vamvatsikos, and M. Aschheim. “Application of Nonlinear Static Procedures for the Seismic Assessment of Regular RC Moment Frame Buildings.” In: *Earthquake Spectra* 30.2 (2014), pp. 767–794.

[30] E. Spacone, F. C. Filippou, and Fabio F. Taucer. “Fiber beam-column model for non-linear analysis of R/C frames: Part II. Applications.” In: *Earthquake Engineering and Structural Dynamics* 25.7 (1996), pp. 727–742.

[31] S. A. Kaba and S. A. Mahin. *Refined Modelling of Reinforced Concrete Columns*. Tech. rep. Berkeley: University of California, 1984.

[32] F. F. Taucer, E. Spacone, and F. C. Filippou. *A Fiber Beam-Column Element for Seismic Response Analysis of Reinforced Concrete Structures*. Tech. rep. Berkeley: University of California, 1991.

[33] B. N. Alemdar and D. W. White. "Displacement, Flexibility, and Mixed Beam–Column Finite Element Formulations for Distributed Plasticity Analysis." In: *Journal of Structural Engineering* 131.12 (2005), pp. 1811–1819.

[34] M. Fragiadakis and M. Papadrakakis. "Modeling, analysis and reliability of seismically excited structures: Computational issues." In: *International Journal of Computational Methods* 05.04 (2008), pp. 483–511.

[35] J. Coleman and E. Spacone. "Localization Issues in Force-Based Frame Elements." In: *Journal of Structural Engineering* 127.11 (2001), pp. 1257–1265.

[36] M. H. Scott. *Numerical Integration Options for the Force-Based Beam-Column Element in OpenSees*. Tech. rep. OpenSees wiki, 2011.

[37] A. Neuenhofer and F. C. Filippou. "Evaluation of Nonlinear Frame Finite-Element Models." In: *Journal of Structural Engineering* 123.7 (1997), pp. 958–966.

[38] A. Neuenhofer and F. C. Filippou. "Geometrically Nonlinear Flexibility-Based Frame Finite Element." In: *Journal of Structural Engineering* 124.6 (1998), pp. 704–711.

[39] E. W. Weisstein. *Lobatto Quadrature*. URL: `http://mathworld.wolfram.com/LobattoQuadrature.html` (Cited 06/04/2018).

[40] T. Paulay and M. Priestley. *Seismic Design of Reinforced Concrete and Masonry Buildings*. 1st ed. New York: John Wiley and Sons, 1992.

[41] OpenSees wiki. *Beam With Hinges Element*. 2006. URL: `http://opensees.berkeley.edu/wiki/index.php/Beam_With_Hinges_Element` (Cited 03/13/2018).

[42] M. H. Scott and K. L. Ryan. "Moment-Rotation Behavior of Force-Based Plastic Hinge Elements." In: *Earthquake Spectra* 29.2 (2013), pp. 597–607.

[43] C.-L. Lee and F. C. Filippou. "Efficient Beam-Column Element with Variable Inelastic End Zones." In: *Journal of Structural Engineering* 135.11 (2009), pp. 1310–1319.

[44] N. Li, Z. Li, and L. Xie. "A fiber-section model based Timoshenko beam element using shear-bending interdependent shape function." In: *Earthquake Engineering and Engineering Vibration* 12.3 (2013), pp. 421–432.

[45] J. P. Almeida, S. Das, and R. Pinho. "Adaptive force-based frame element for regularized softening response." In: *Computers & Structures* 102-103 (2012), pp. 1–13.

[46] N. Øystad-Larsen, E. Erduran, and A. M. Kaynia. "Evaluation of effect of confinement on the collapse probability of reinforced concrete frames subjected to earthquakes." In: *Procedia Engineering* 199 (2017), pp. 784–789.

[47] J. B. Mander, M. J. N. Priestley, and R Park. "Theoretical Stress-Strain Model for Confined Concrete." In: *Journal of Structural Engineering* 114.8 (1988), pp. 1804–1826.

[48] S. Popovics. "A numerical approach to the complete stress-strain curve of concrete." In: *Cement and Concrete Research* 3.5 (1973), pp. 583–599.

[49] P. H. Bischoff and S. H. Perry. "Compressive behaviour of concrete at high strain rates." In: *Materials and Structures* 24.6 (1991), pp. 425–450.

[50] B. D. Scott, R. Park, and M. J. N. Priestley. "Stress-Strain Behavior of Concrete Confined by Overlapping Hoops at Low and High Strain Rates." In: *Journal Proceedings* 79.1 (1982), pp. 13–27.

[51] J. B. Mander, M. J. N. Priestley, and R. Park. "Observed Stress-Strain Behavior of Confined Concrete." In: *Journal of Structural Engineering* 114.8 (1988), pp. 1827–1849.

[52] R. D. Cook. *Concepts and applications of finite element analysis*. 4th ed. New York: Wiley, 2002.

[53] E. Erduran. "Evaluation of Rayleigh damping and its influence on engineering demand parameter estimates." In: *Earthquake Engineering & Structural Dynamics* 41.14 (2012), pp. 1905–1919.

[54] A. K. Chopra and F. McKenna. "Modeling viscous damping in nonlinear response history analysis of buildings for earthquake excitation." In: *Earthquake Engineering & Structural Dynamics* 45.2 (2016), pp. 193–211.

[55] The Pacific Earthquake Engineering Research Center. *The Structural Performance Database*. 2014. URL: http://peer.berkeley.edu/ngawest2/databases/ (Cited 02/12/2018).

[56] F. Bjercke. "Non-linear analysis methods in performance-based earthquake engineering." Doctoral dissertation. Norwegian University of Science and Technology, 2016.

[57] M. Cemalovic. "Earthquake analysis of structures using nonlinear models." Doctoral dissertation. Norwegian University of Science and Technology, 2015.

[58] S. A. Semere. "Investigation of RC Structural Behaviour of Wall-Equivalent Dual System through Non-Linear Analyses." Doctoral dissertation. Norwegian University of Science and Technology, 2016.

[59] Standard Norge. *NS-EN 1992 - Eurocode 2: Design of concrete structures. Part 1-1: General rules and rules for buildings*. Lysaker, 2008.

[60] OpenSees wiki. *Concrete04 Material*. 2006. URL: http://opensees.berkeley.edu/wiki/index.php/Concrete04_Material_--_Popovics_Concrete_Material (Cited 03/13/2018).

[61] OpenSees wiki. *Moment Curvature Example*. 2011. URL: http://opensees.berkeley.edu/wiki/index.php/Moment_Curvature_Example (Cited 04/20/2018).

[62] The Pacific Earthquake Engineering Research Center. *The Structural Performance Database*. 2003. URL: https://nisee.berkeley.edu/spd/ (Cited 02/08/2018).

# Appendix A

# Drawings of structure

This appendix presents drawings of structural elements.

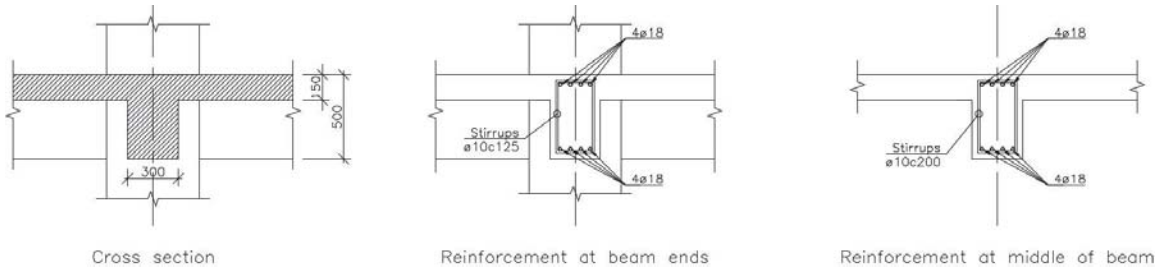


**Figure A.1:** Beams at first, second and third floor. This figure has been provided by Øystad-Larsen.

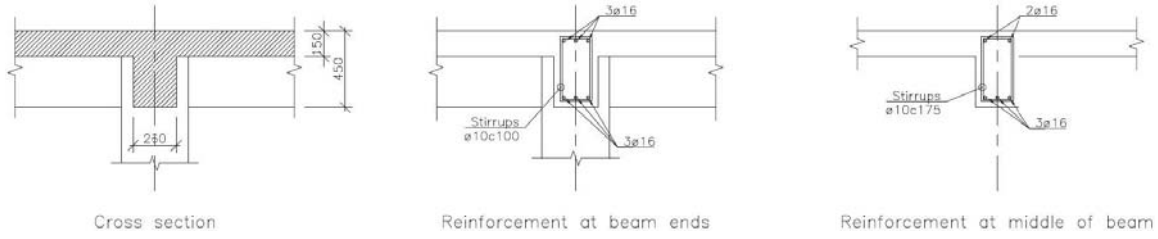


**Figure A.2:** Beams at roof level. This figure has been provided by Øystad-Larsen.

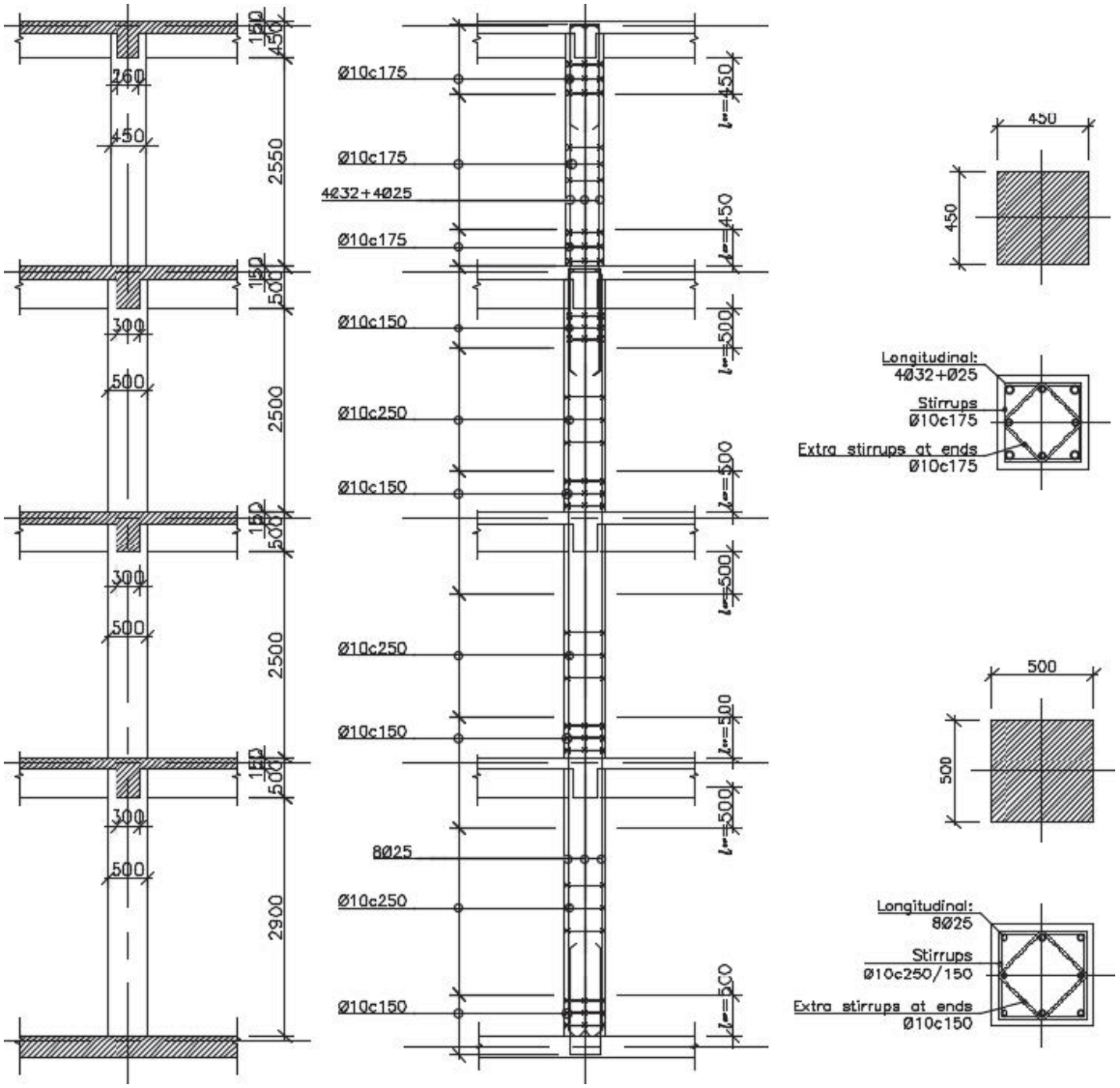


**Figure A.3:** Internal columns. This figure has been provided by Øystad-Larsen.

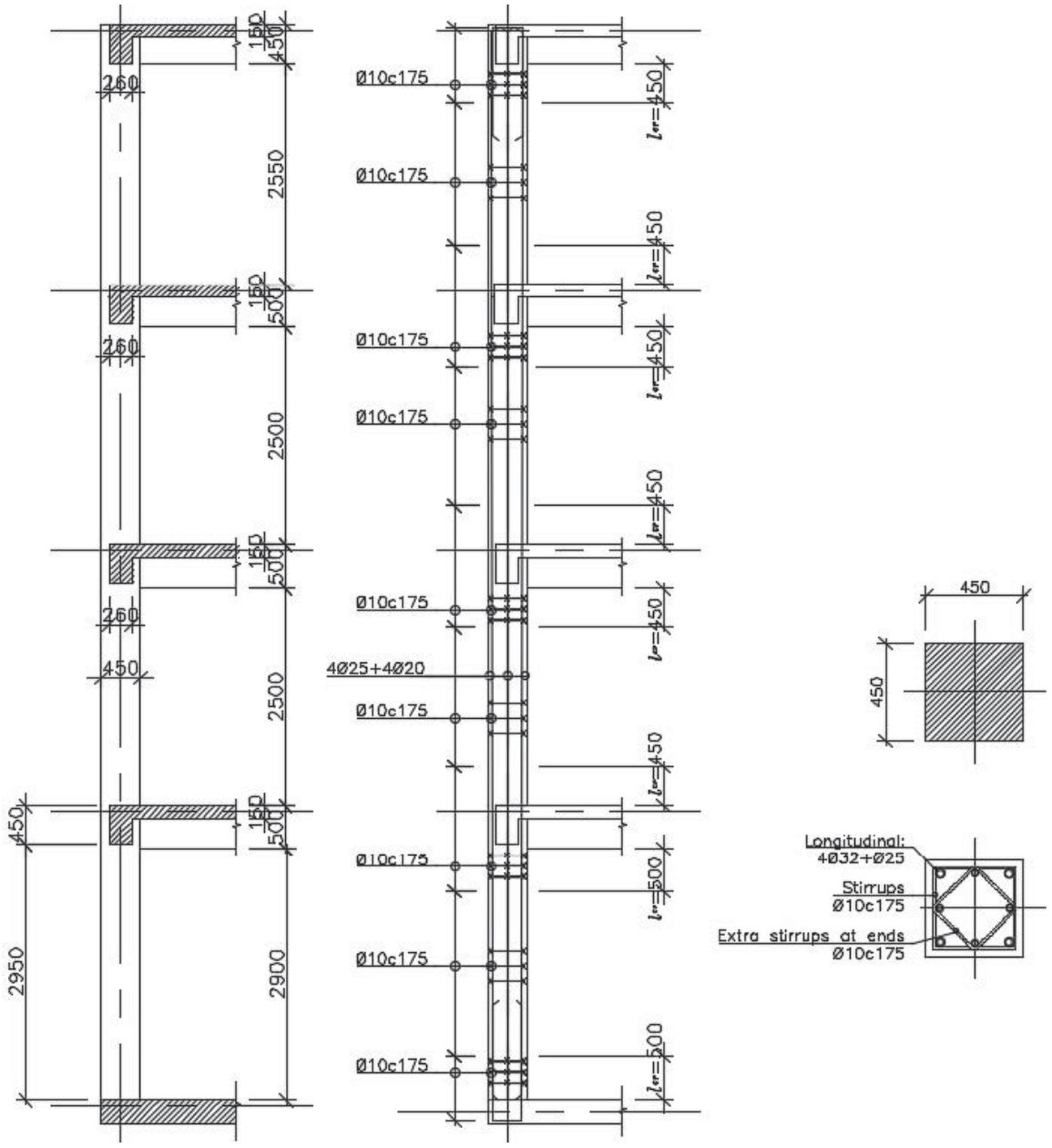


**Figure A.4:** Boarder columns. This figure has been provided by Øystad-Larsen.

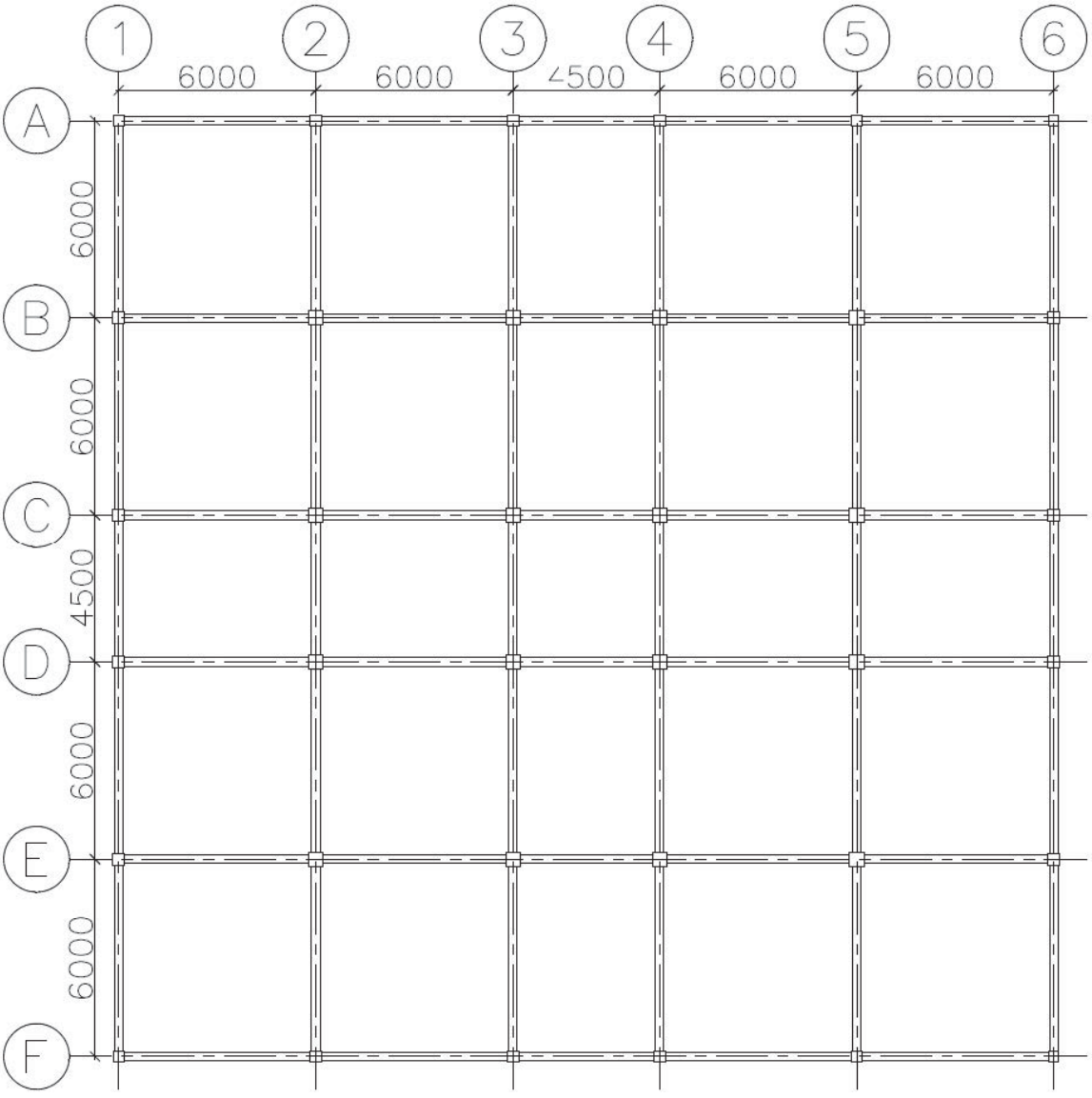


**Figure A.5:** Plan view of the structure. This figure has been provided by Øystad-Larsen.

# Appendix B

# Ground motion records

The following is a presentation of the seven ground motion records used in the NTHAs. They are collected from the NGA-West2 ground motion database, developed by PEER [62]. The records are unscaled and not processed in any other way.

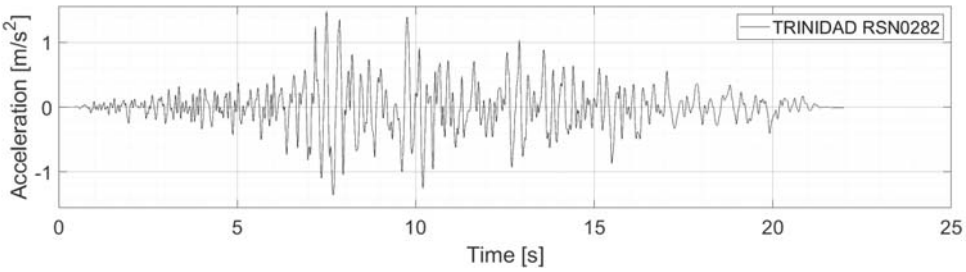


**Figure B.1:** As recorded, ground acceleration record. 0282 Trinidad.

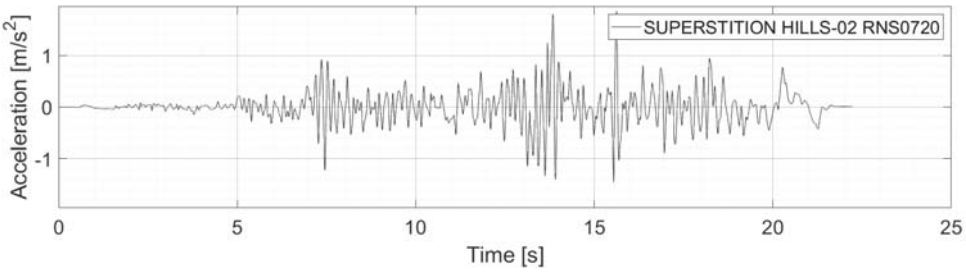


**Figure B.2:** As recorded, ground acceleration record. 0720 Superstition Hills.

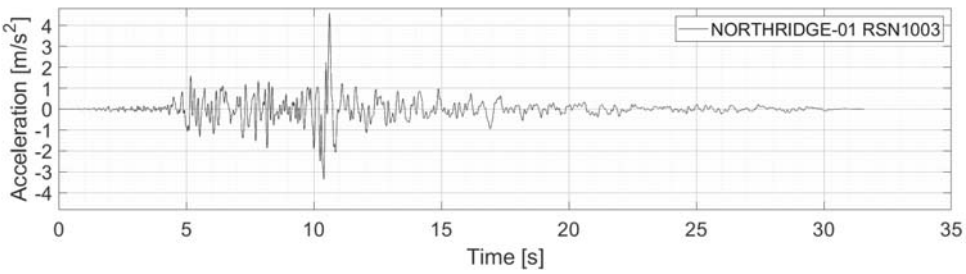


**Figure B.3:** As recorded, ground acceleration record. 1003 Northridge.

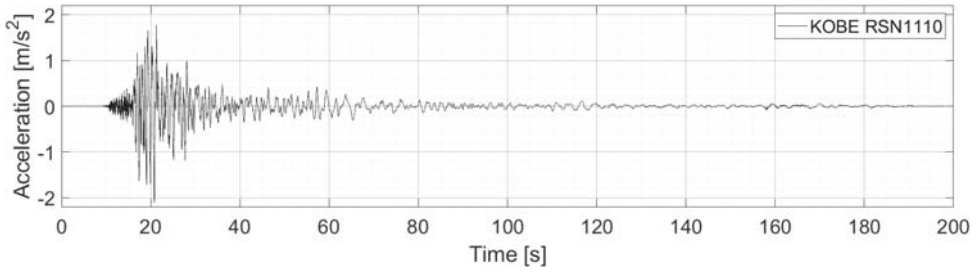


**Figure B.4:** As recorded, ground acceleration record. 1110 Kobe.

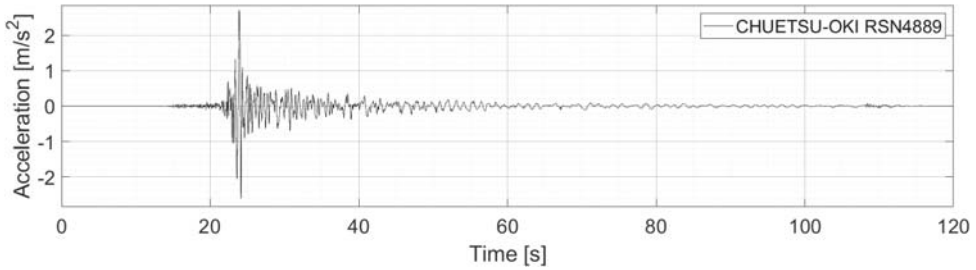


**Figure B.5:** As recorded, ground acceleration record. 4889 Chuetsu-Oki.

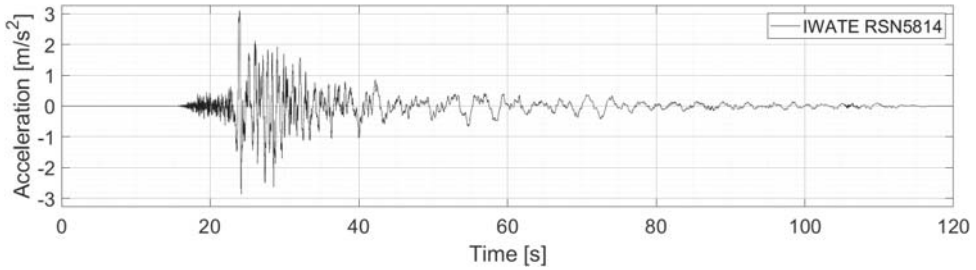


**Figure B.6:** As recorded, ground acceleration record. 5814 Iwate.

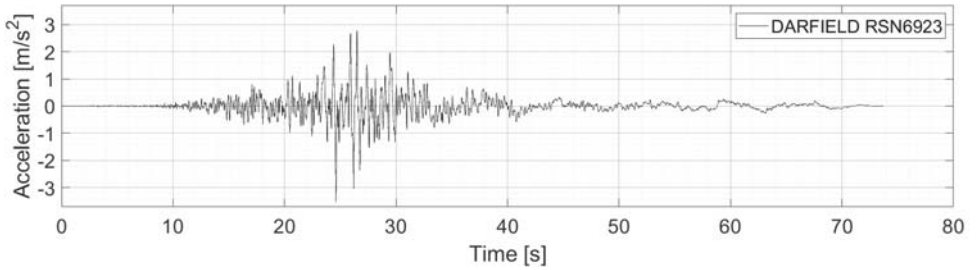


**Figure B.7:** As recorded, ground acceleration record. 6923 Darfield.

# Appendix C

# Response histories - FB model

The following is a presentation of the seven response histories for node 43 for the FB models.

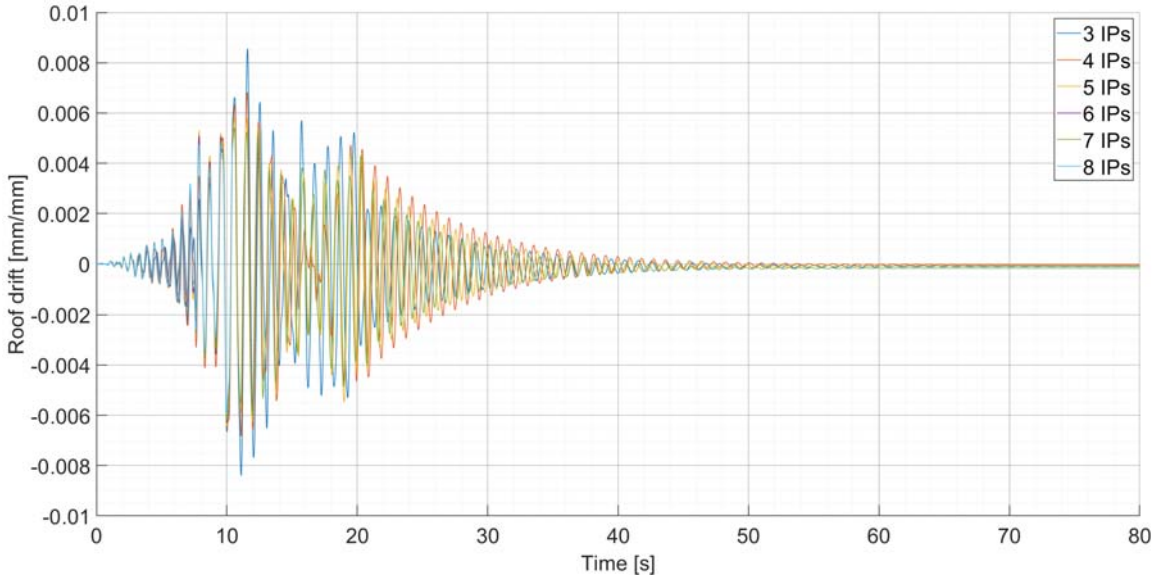


**Figure C.1:** Response histories using the FB model for node 43. 0282 Trinidad.

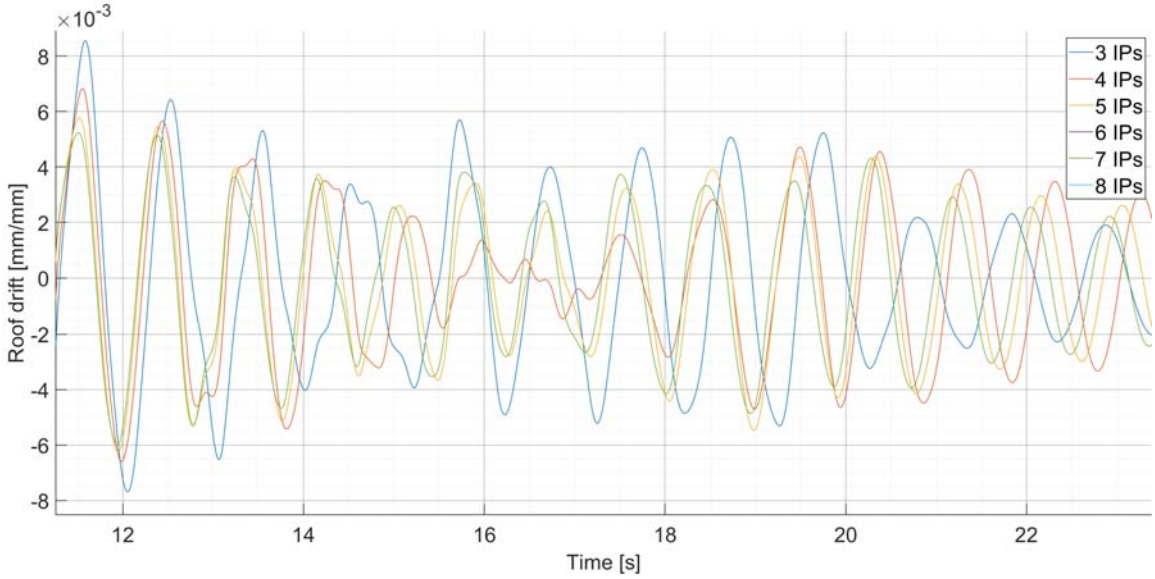


**Figure C.2:** Response histories using the FB model for node 43. 0282 Trinidad.

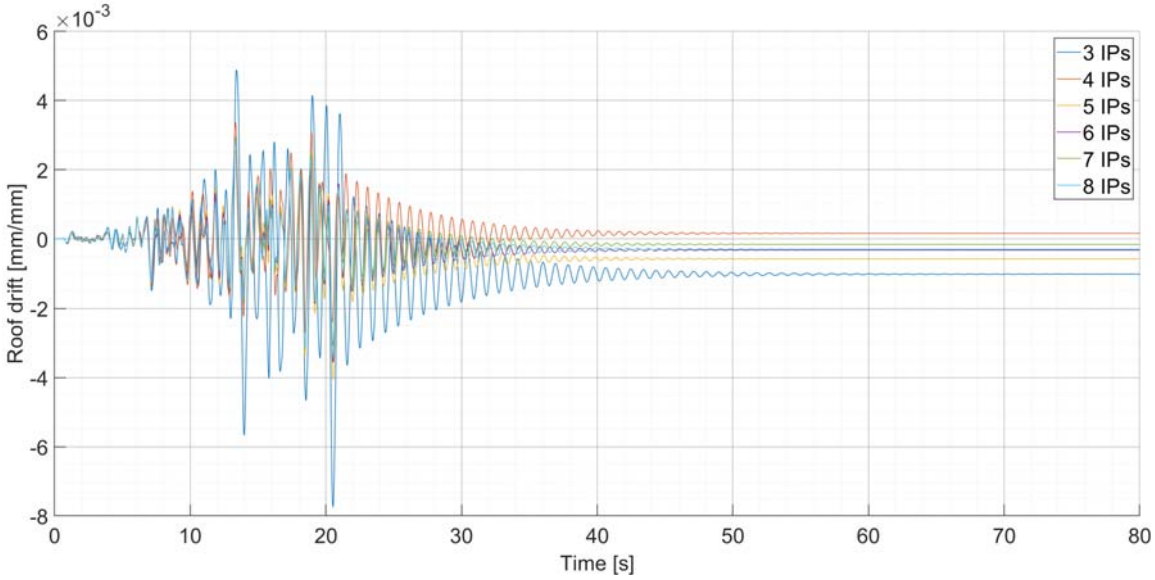


**Figure C.3:** Response histories using the FB model for node 43. 0720 Superstition Hills.

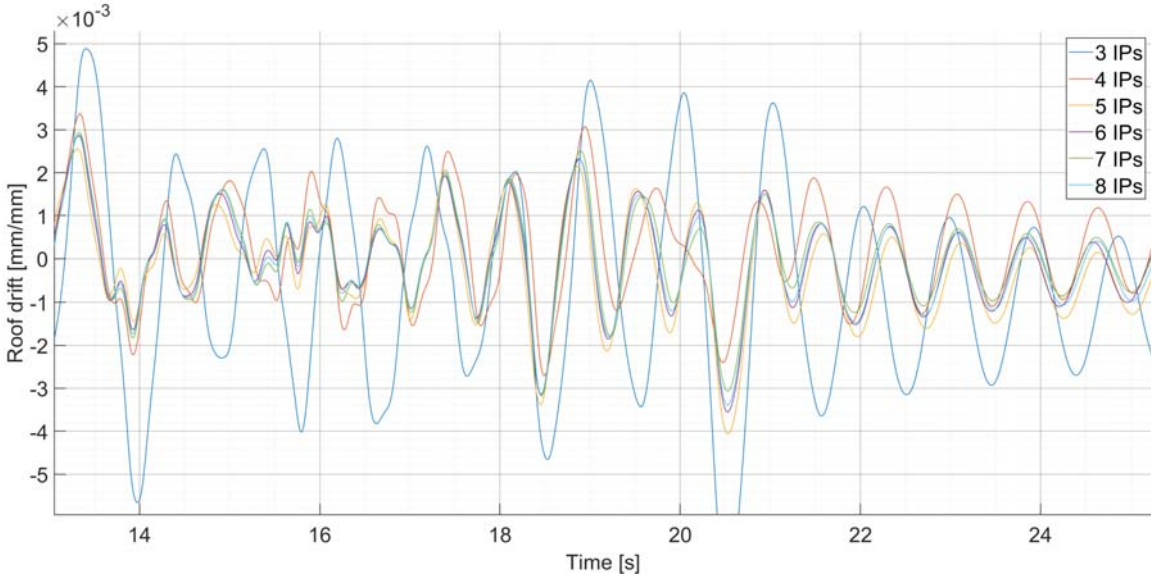


**Figure C.4:** Response histories using the FB model for node 43. 0720 Superstition Hills.

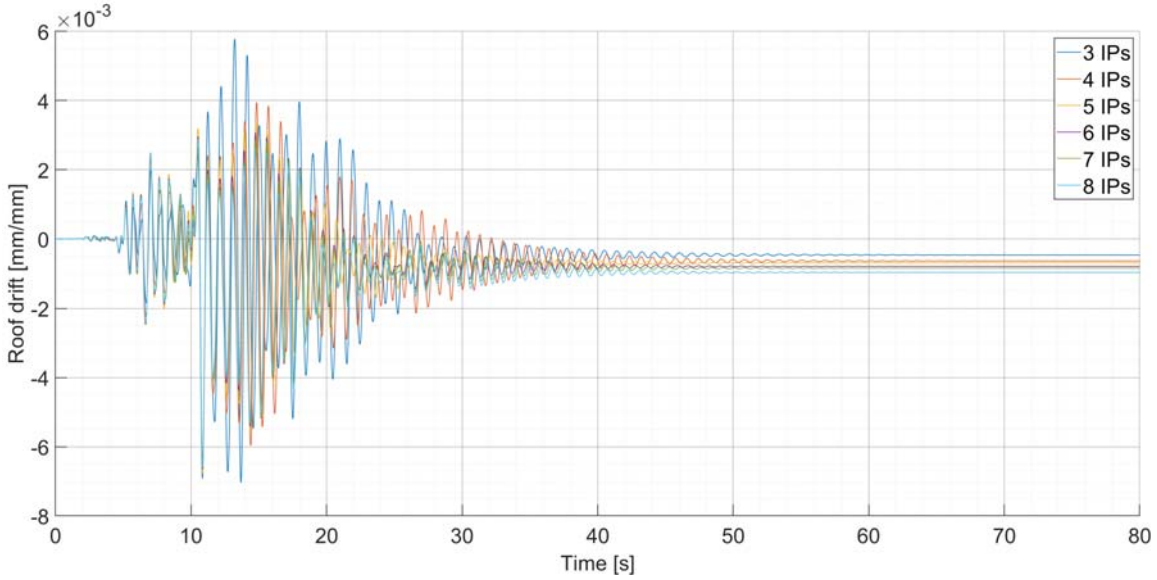


**Figure C.5:** Response histories using the FB model for node 43. 1003 Northridge.

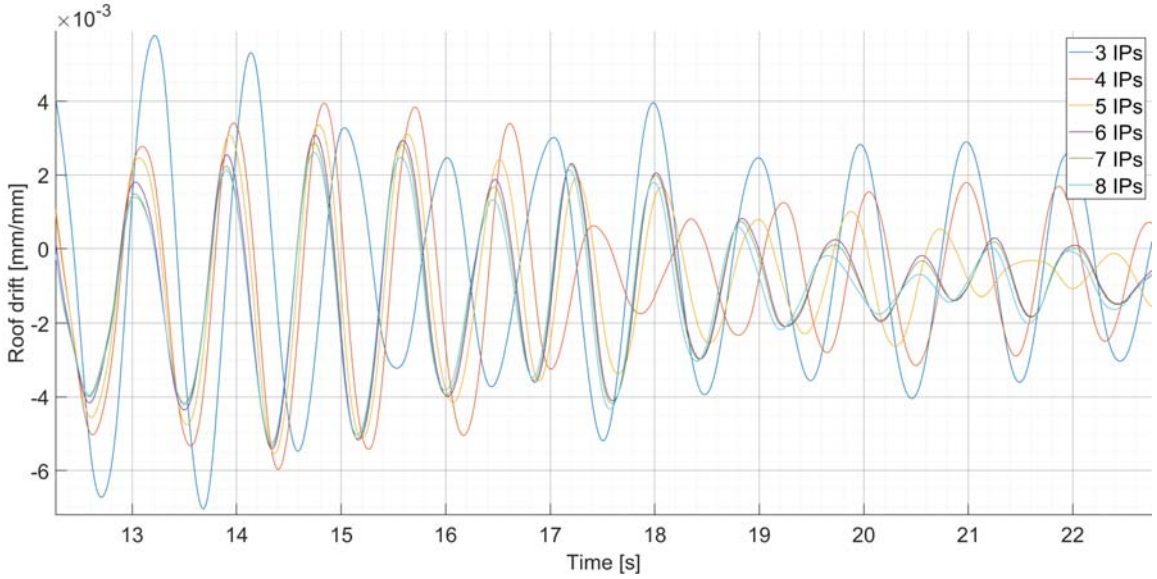


**Figure C.6:** Response histories using the FB model for node 43. 1003 Northridge.

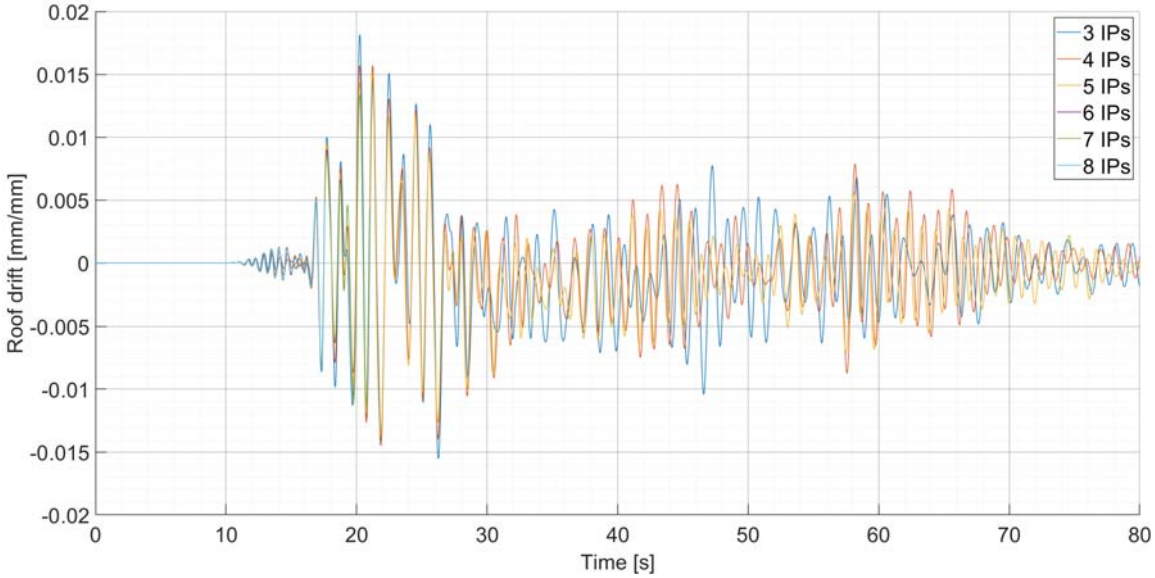


**Figure C.7:** Response histories using the FB model for node 43. 1110 Kobe.

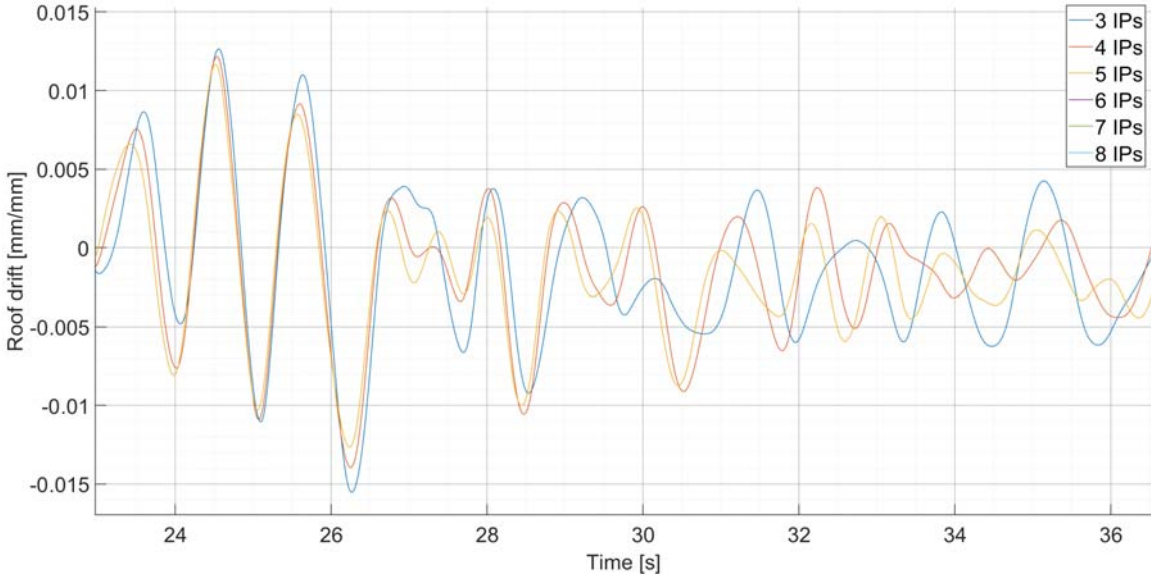


**Figure C.8:** Response histories using the FB model for node 43. 1110 Kobe.

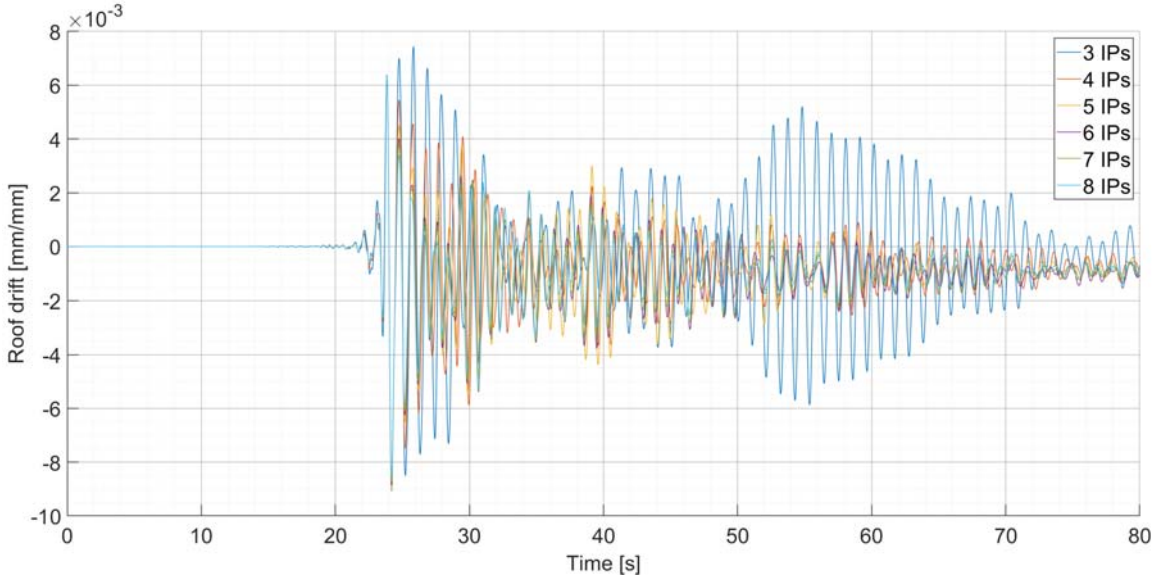


**Figure C.9:** Response histories using the FB model for node 43. 4889 Chuetsu-Oki.

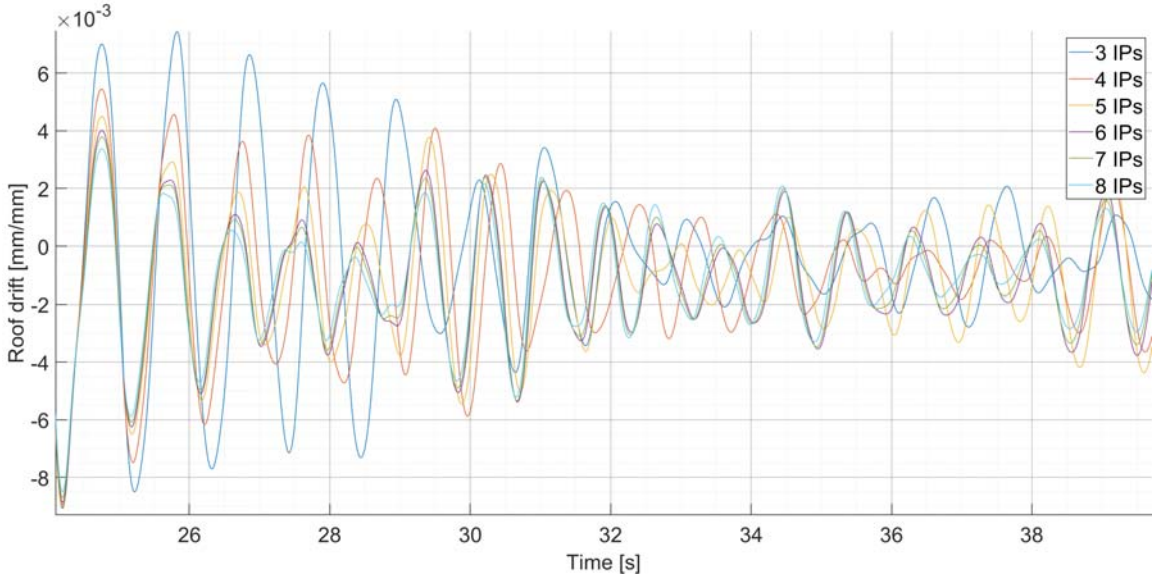


**Figure C.10:** Response histories using the FB model for node 43. 4889 Chuetsu-Oki.

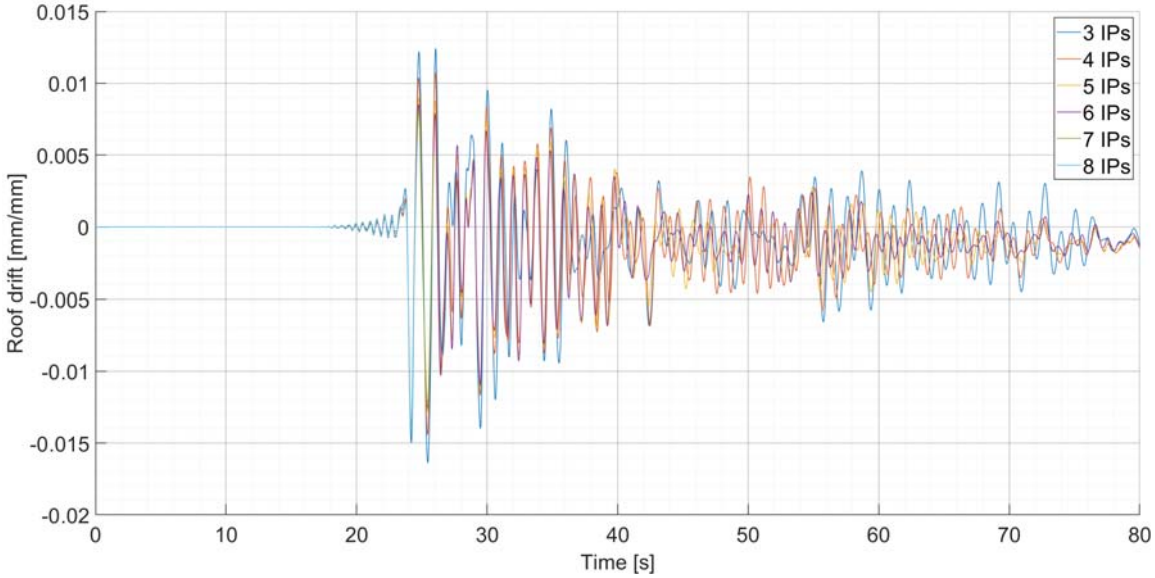


**Figure C.11:** Response histories using the FB model for node 43. 5814 Iwate.

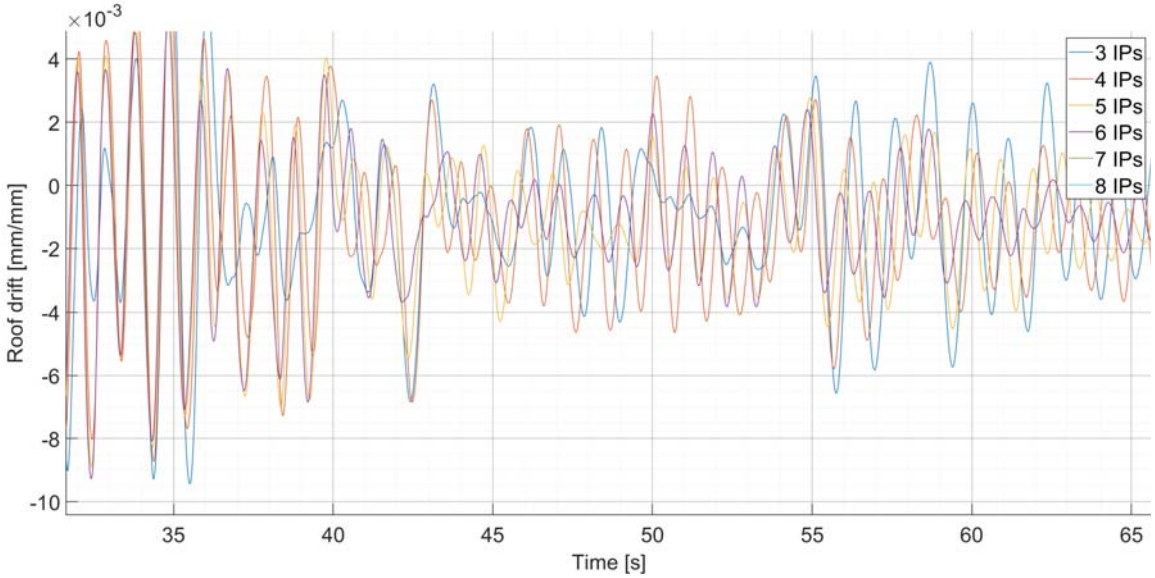


**Figure C.12:** Response histories using the FB model for node 43. 5814 Iwate.

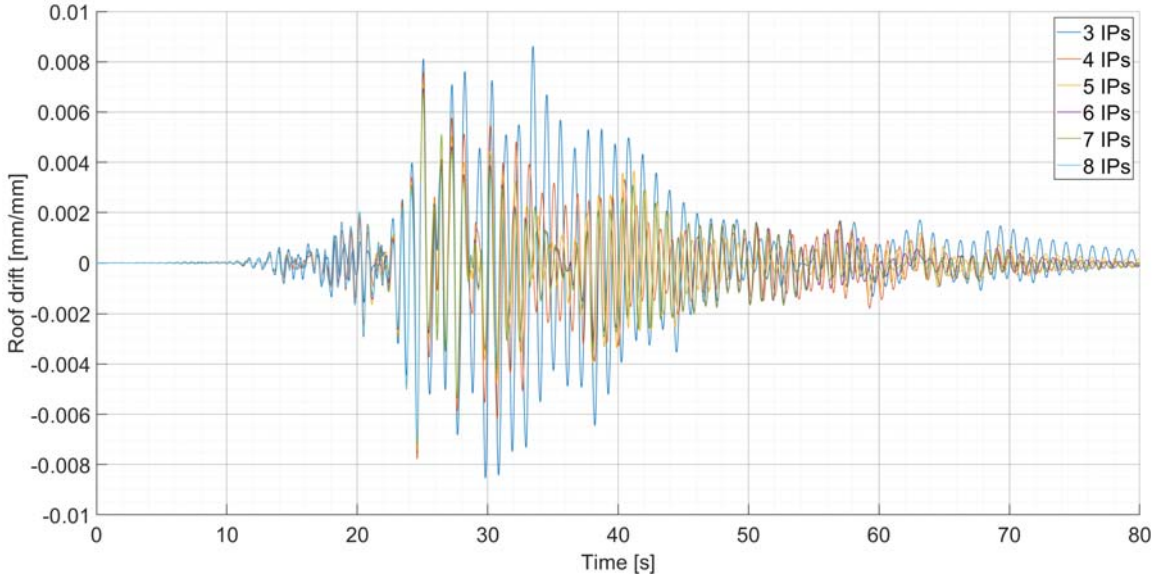


**Figure C.13:** Response histories using the FB model for node 43. 6923 Darfield.

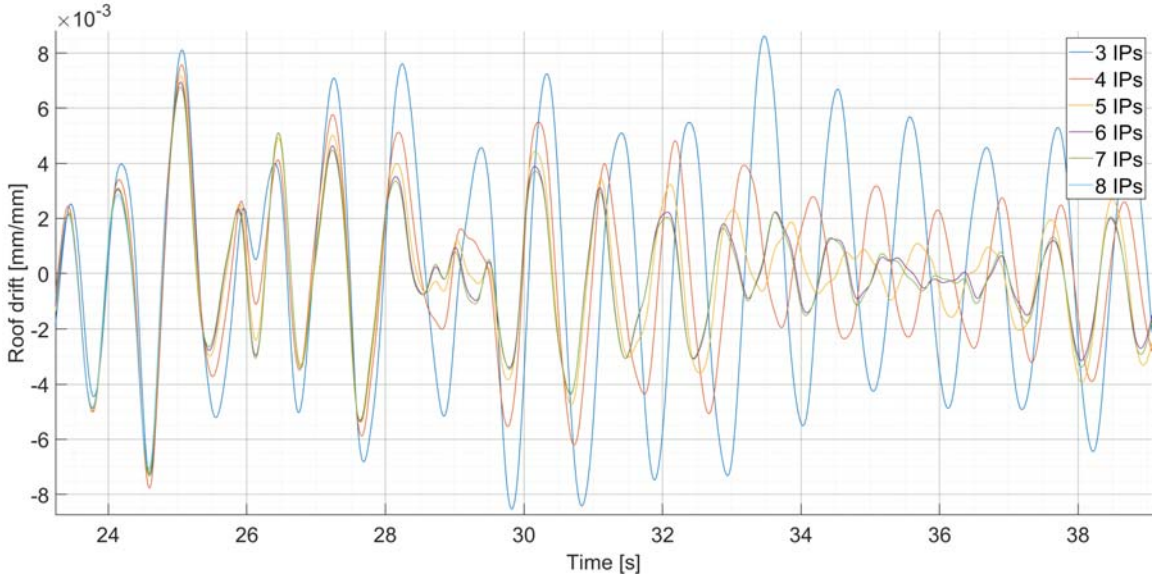


**Figure C.14:** Response histories using the FB model for node 43. 6923 Darfield.

# Appendix D

# Response histories - BwH el. int

The following is a presentation of the seven response histories for node 43 for the BwH models using elements with elastic interior.

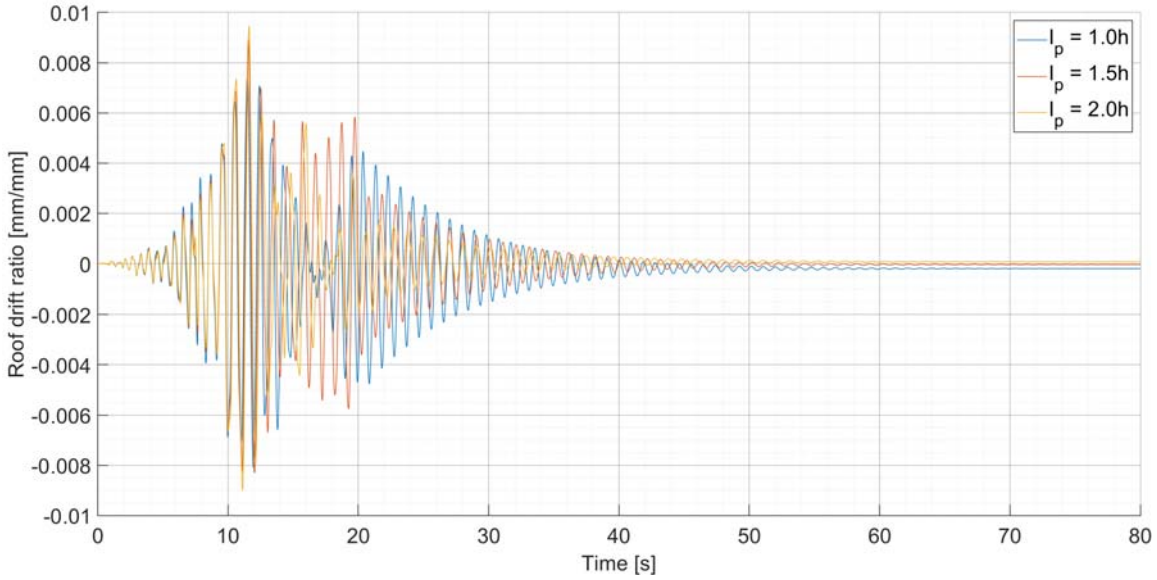


**Figure D.1:** Response histories using the BwH model with elastic interior for node 43. 0282 Trinidad.

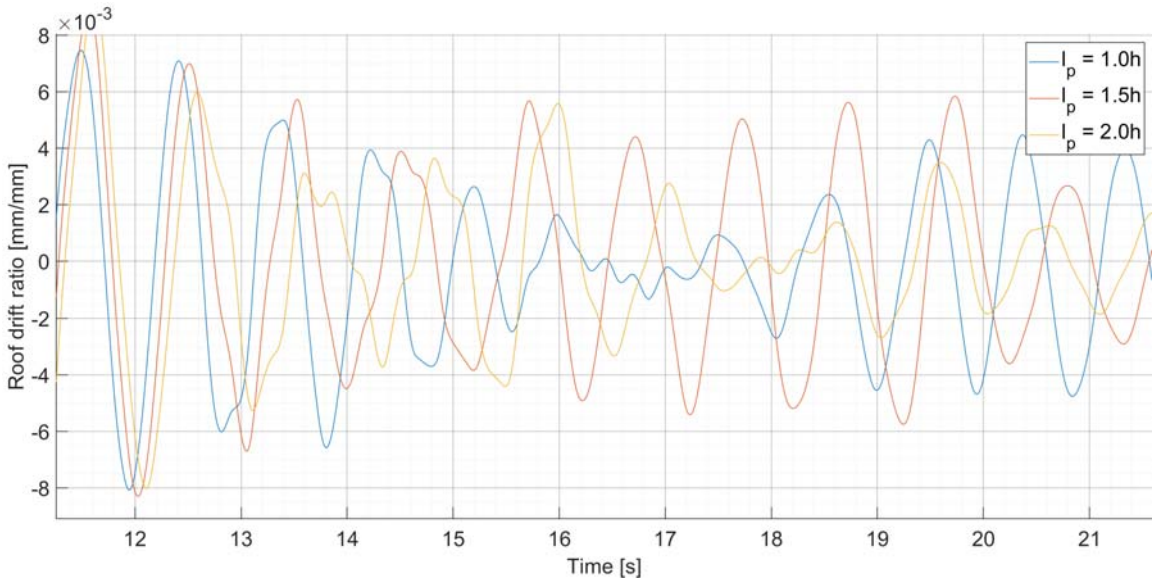


**Figure D.2:** Response histories using the BwH model with elastic interior for node 43. 0282 Trinidad.

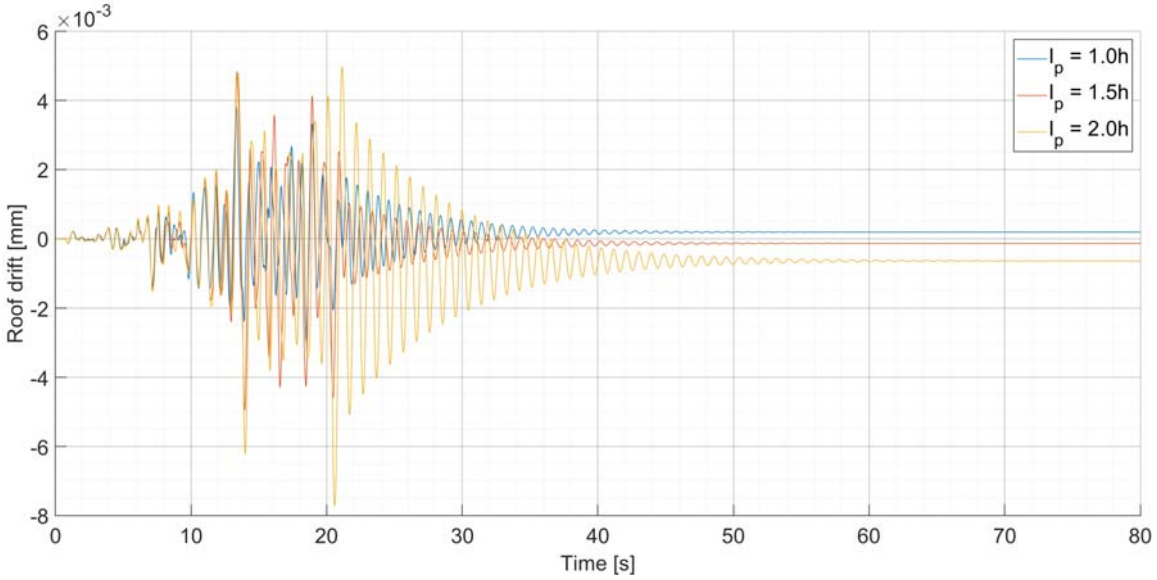


**Figure D.3:** Response histories using the BwH model with elastic interior for node 43. 0720 Superstition Hills.

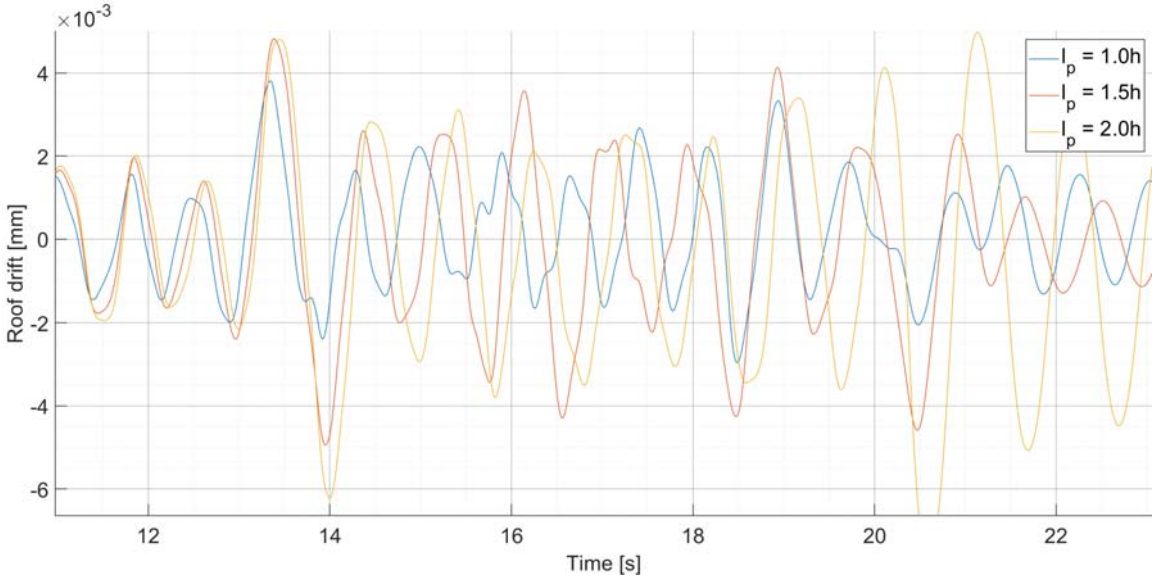


**Figure D.4:** Response histories using the BwH model with elastic interior for node 43. 0720 Superstition Hills.

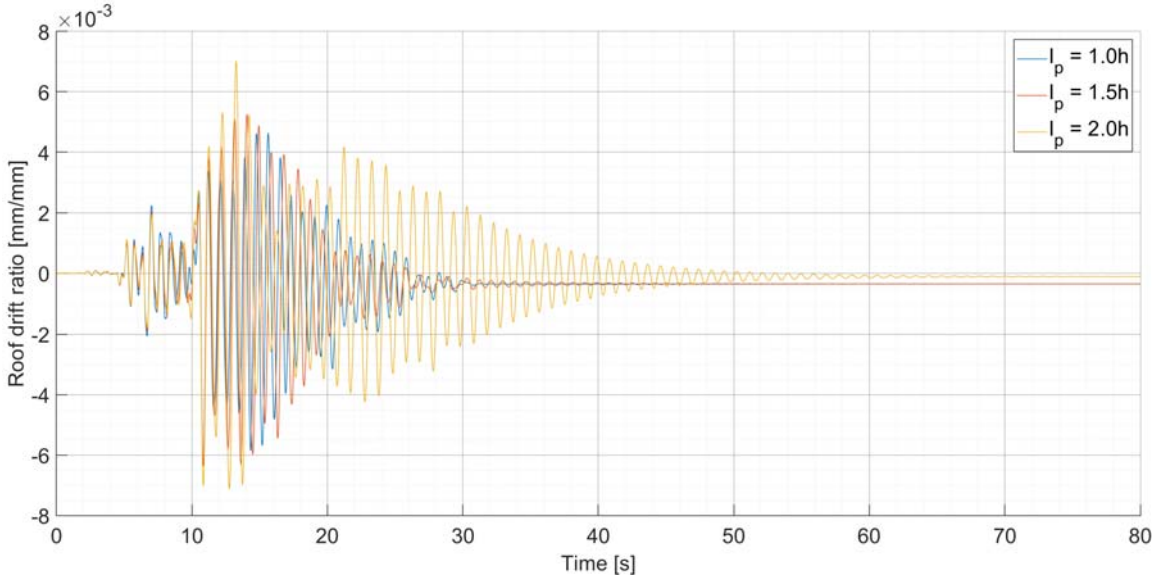


**Figure D.5:** Response histories using the BwH model with elastic interior for node 43. 1003 Northridge.

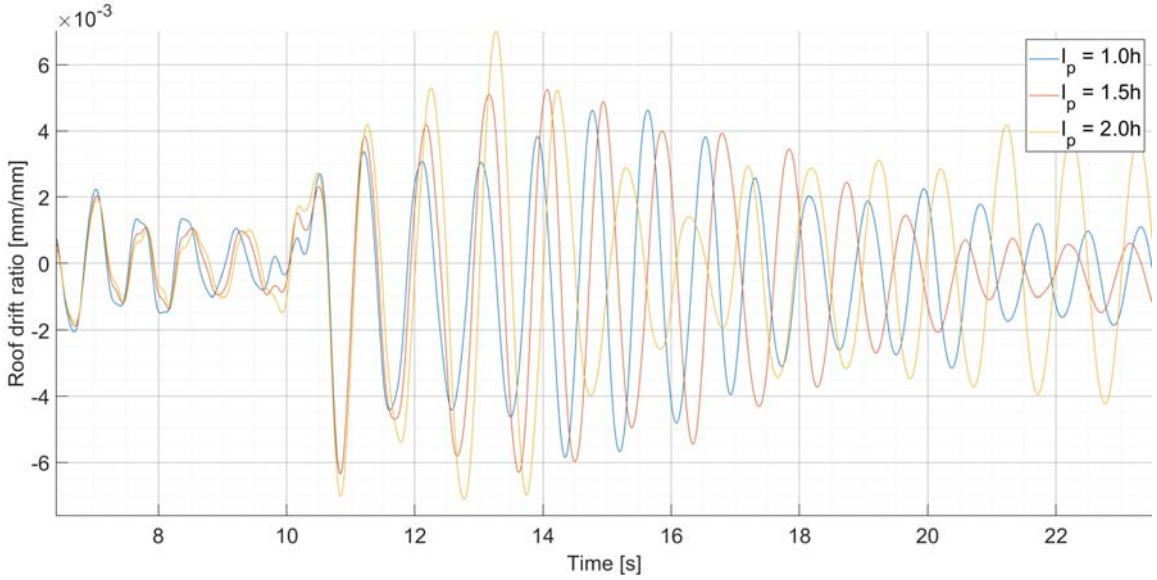


**Figure D.6:** Response histories using the BwH model with elastic interior for node 43. 1003 Northridge.

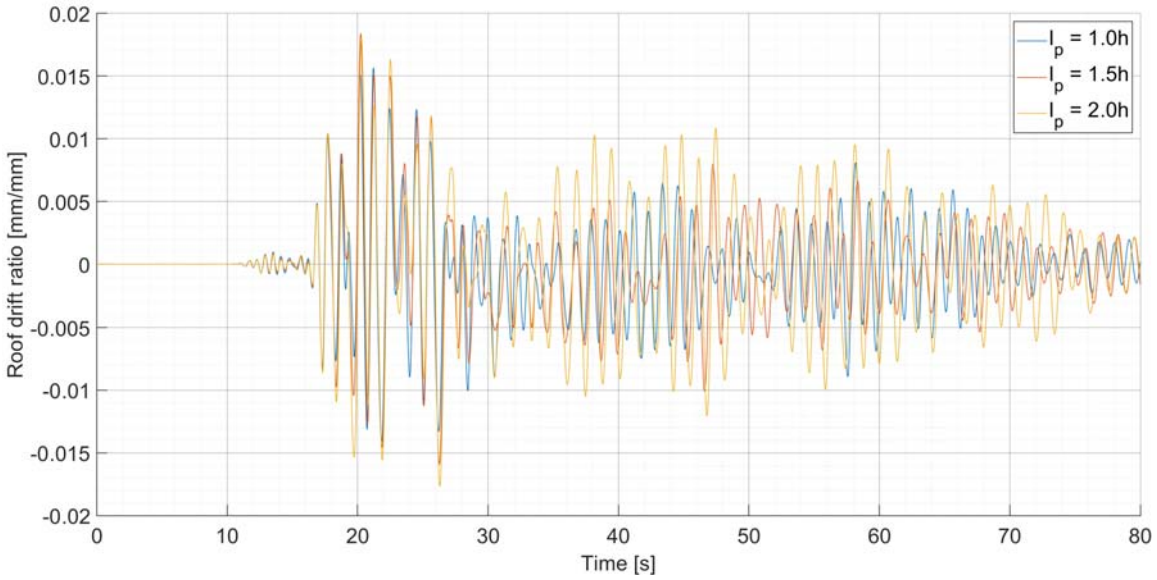


**Figure D.7:** Response histories using the BwH model with elastic interior for node 43. 1110 Kobe.

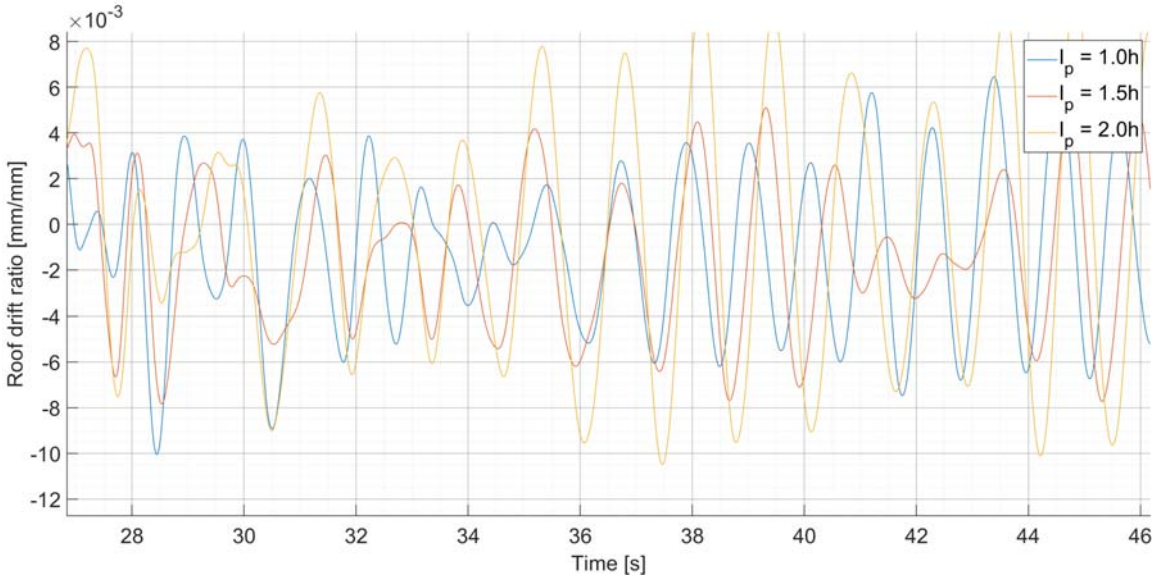


**Figure D.8:** Response histories using the BwH model with elastic interior for node 43. 1110 Kobe.

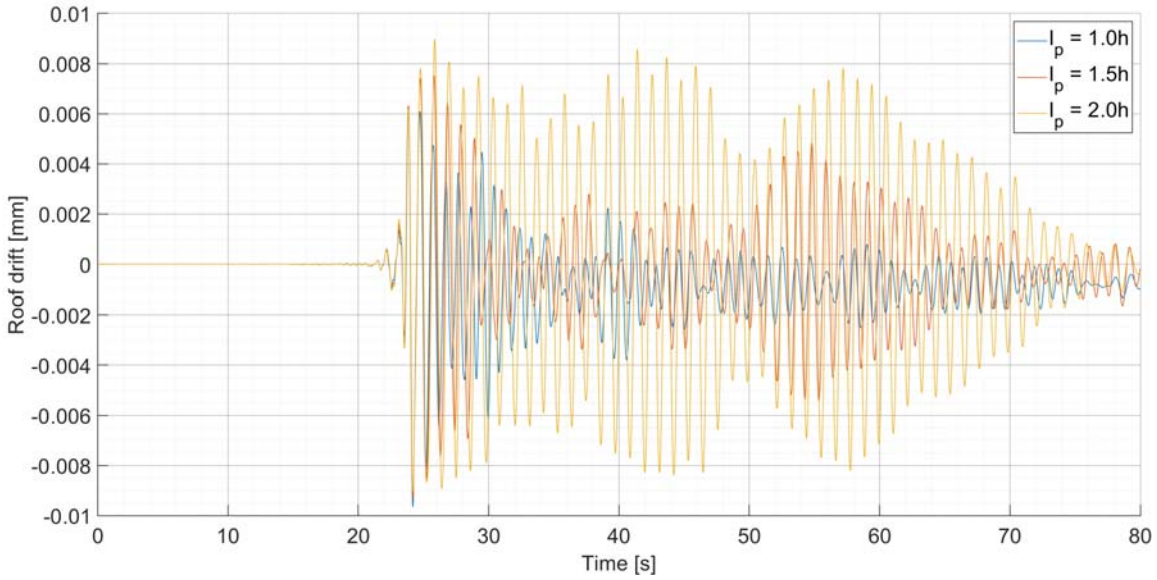


**Figure D.9:** Response histories using the BwH model with elastic interior for node 43. 4889 Chuetsu-Oki.

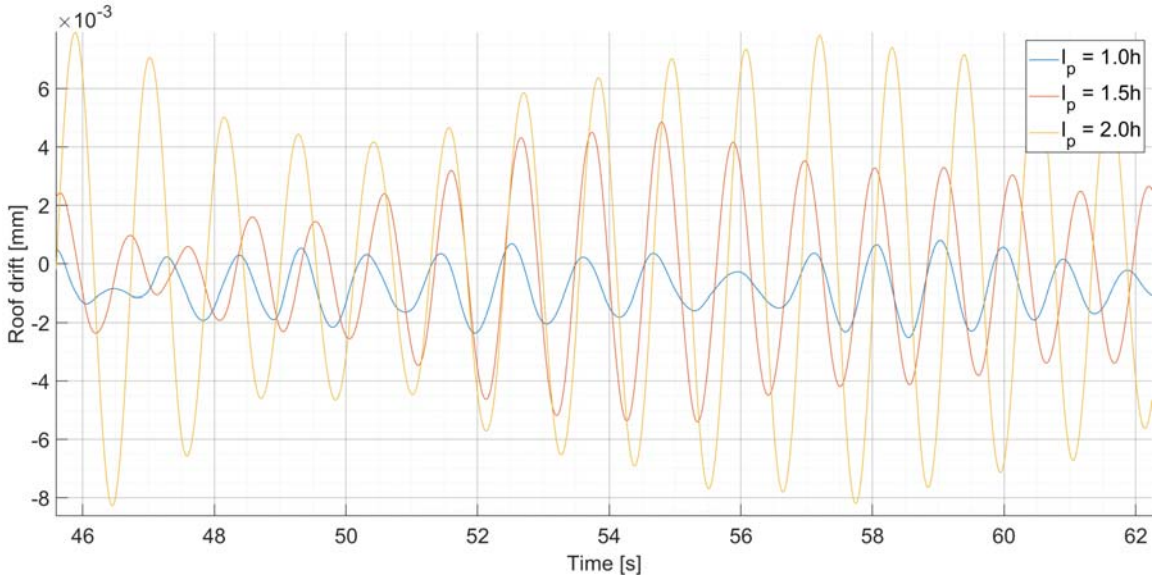


**Figure D.10:** Response histories using the BwH model with elastic interior for node 43. 4889 Chuetsu-Oki.

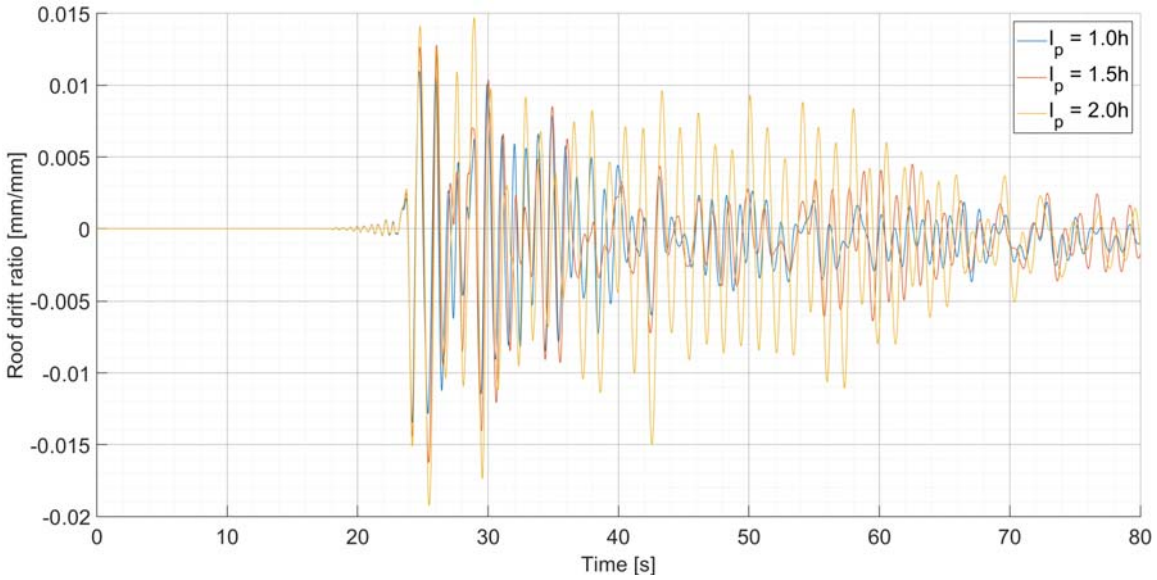


**Figure D.11:** Response histories using the BwH model with elastic interior for node 43. 5814 Iwate.

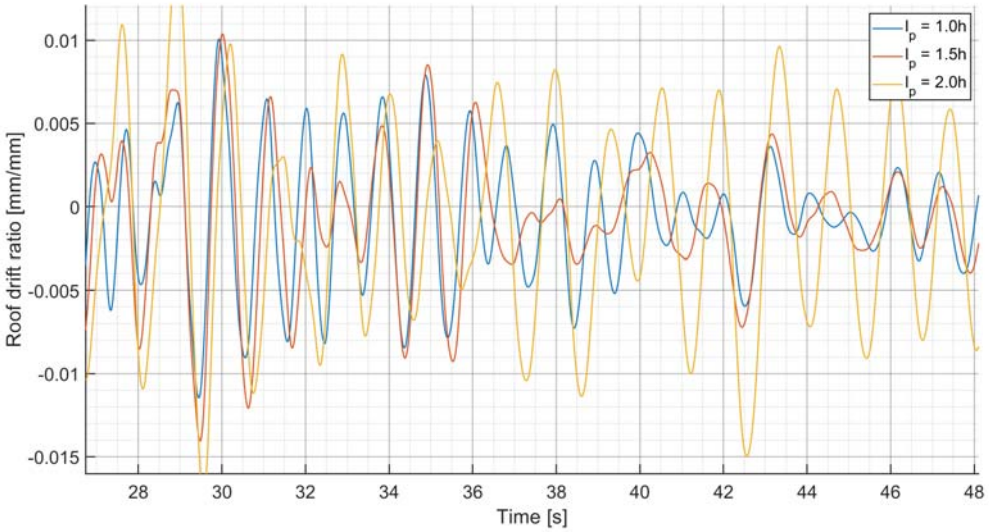


**Figure D.12:** Response histories using the BwH model with elastic interior for node 43. 5814 Iwate.

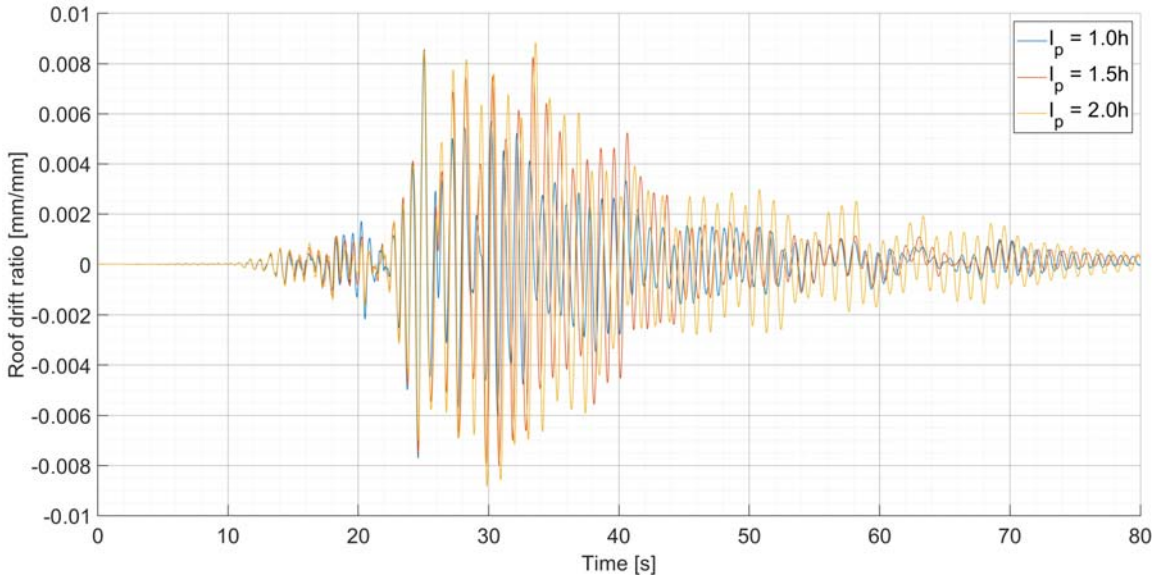


**Figure D.13:** Response histories using the BwH model with elastic interior for node 43. 6923 Darfield.

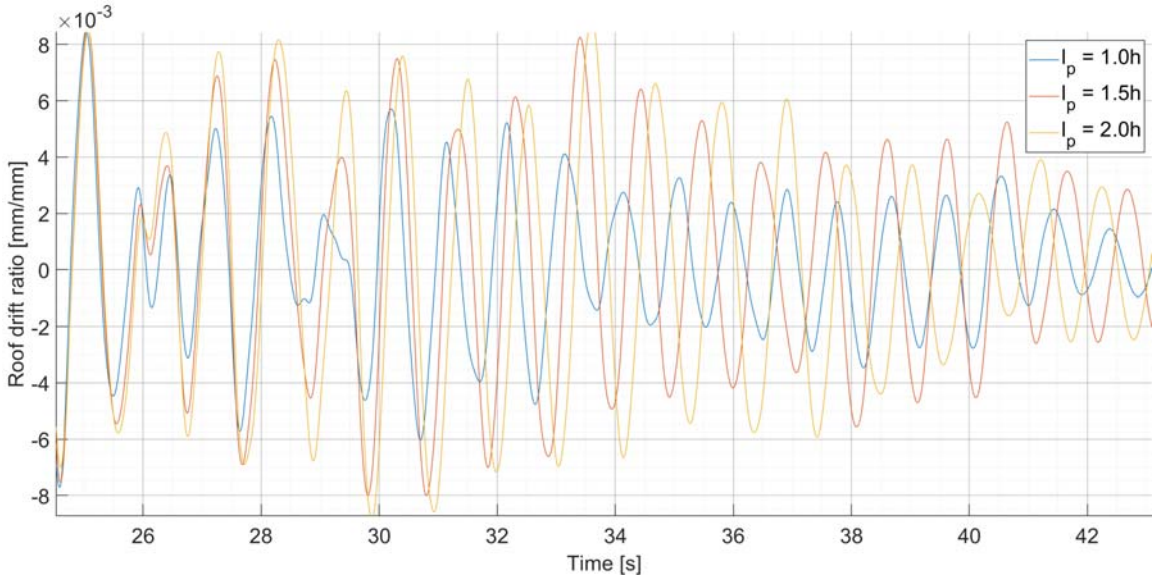


**Figure D.14:** Response histories using the BwH model with elastic interior for node 43. 6923 Darfield.

# Appendix E

# Response histories - BwH inel. int

The following is a presentation of the seven response histories for node 43 for the BwH models using elements with inelastic interior.

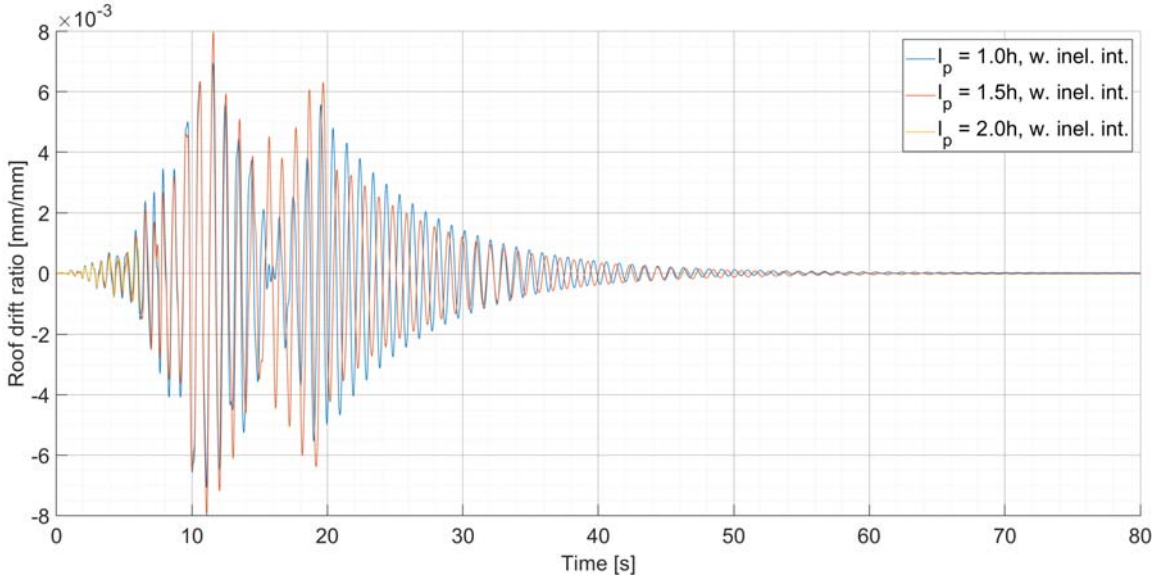


**Figure E.1:** Response histories using the BwH model with inelastic interior for node 43. 0282 Trinidad.

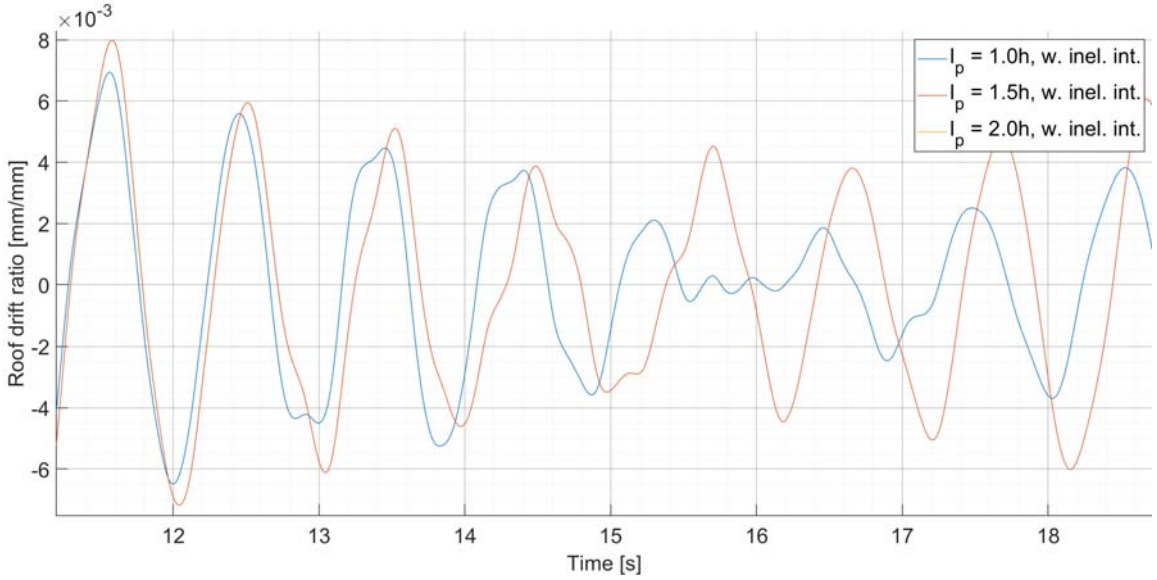


**Figure E.2:** Response histories using the BwH model with inelastic interior for node 43. 0282 Trinidad.

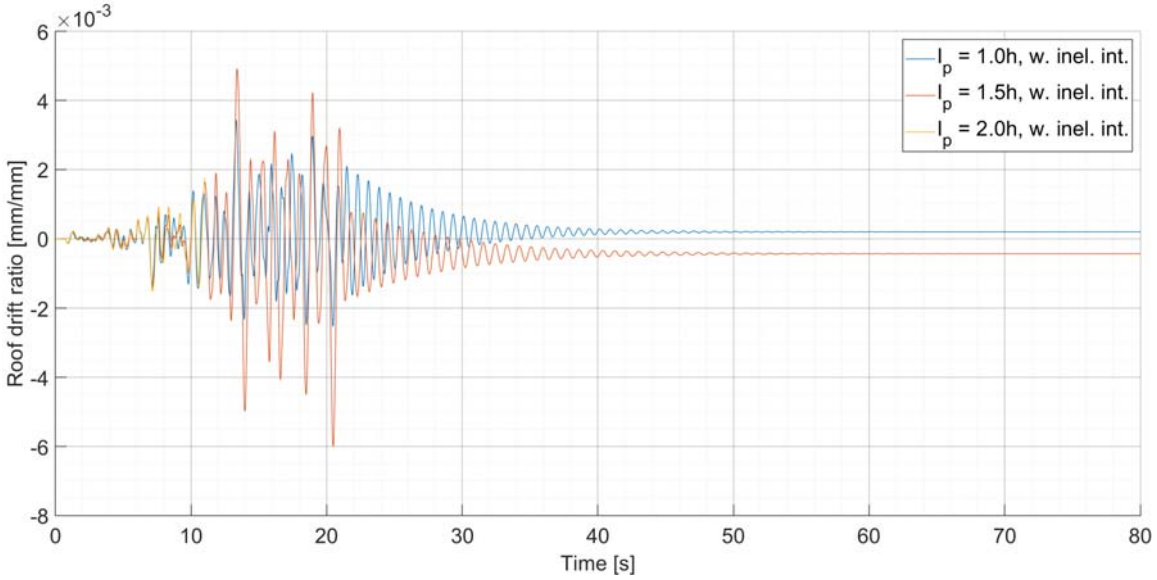


**Figure E.3:** Response histories using the BwH model with inelastic interior for node 43. 0720 Superstition Hills.

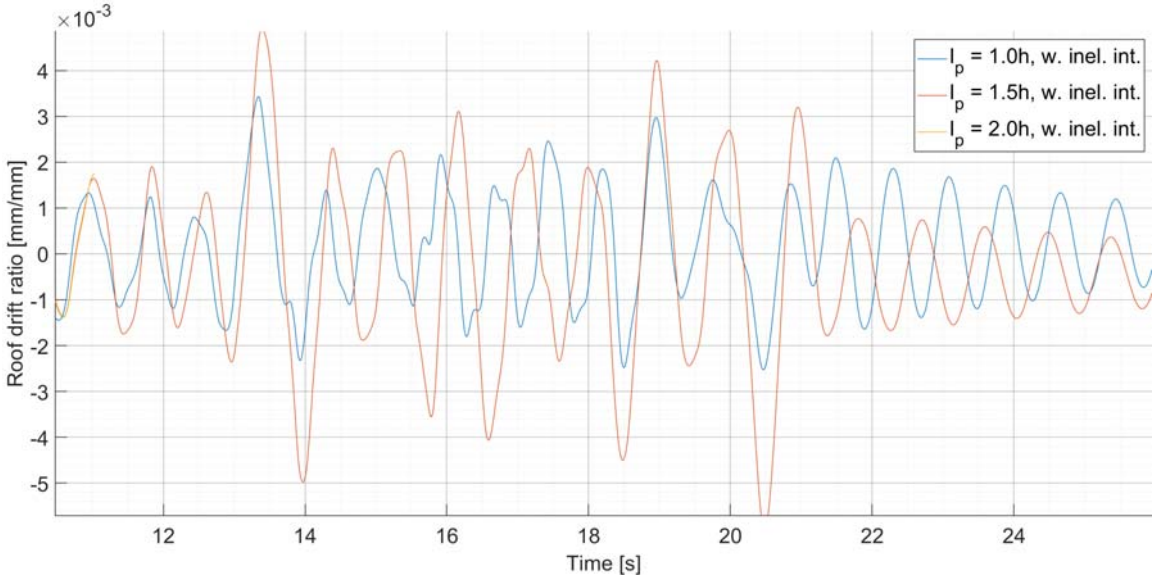


**Figure E.4:** Response histories using the BwH model with inelastic interior for node 43. 0720 Superstition Hills.

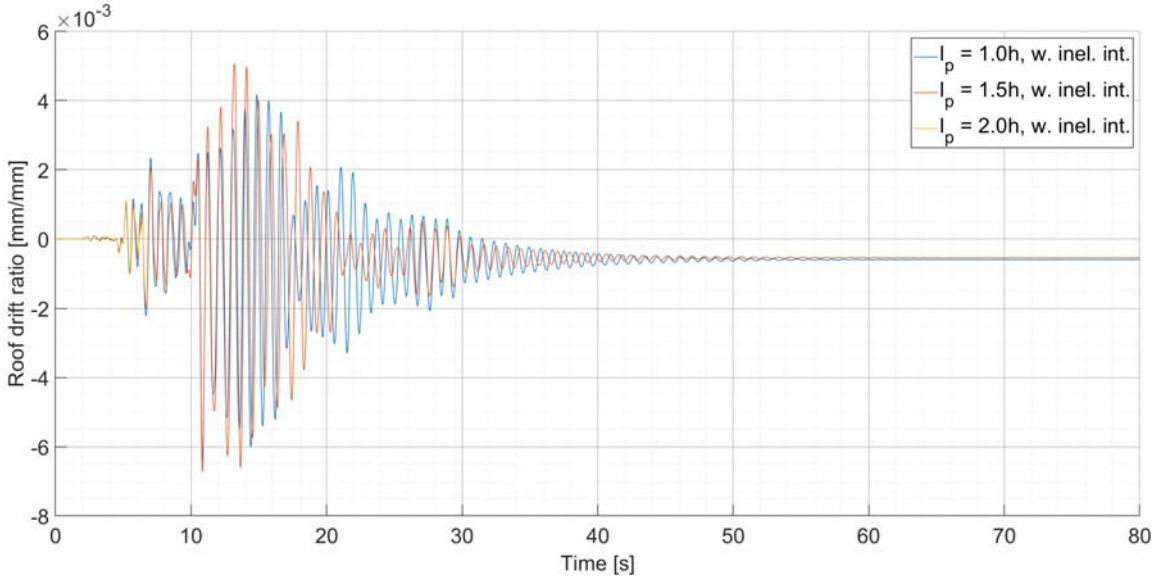


**Figure E.5:** Response histories using the BwH model with inelastic interior for node 43. 1003 Northridge.

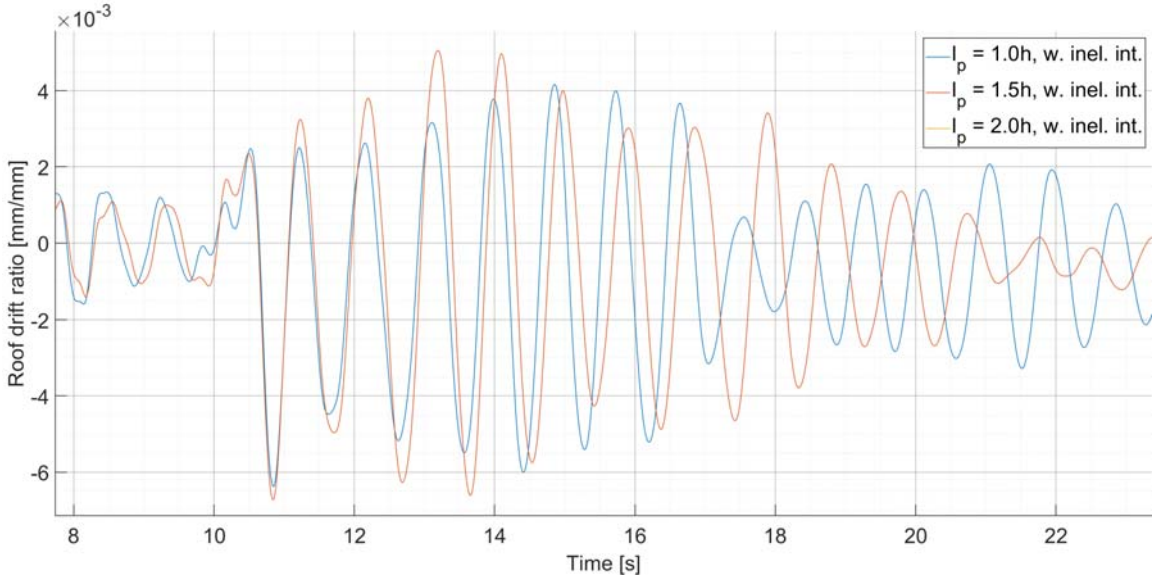


**Figure E.6:** Response histories using the BwH model with inelastic interior for node 43. 1003 Northridge.

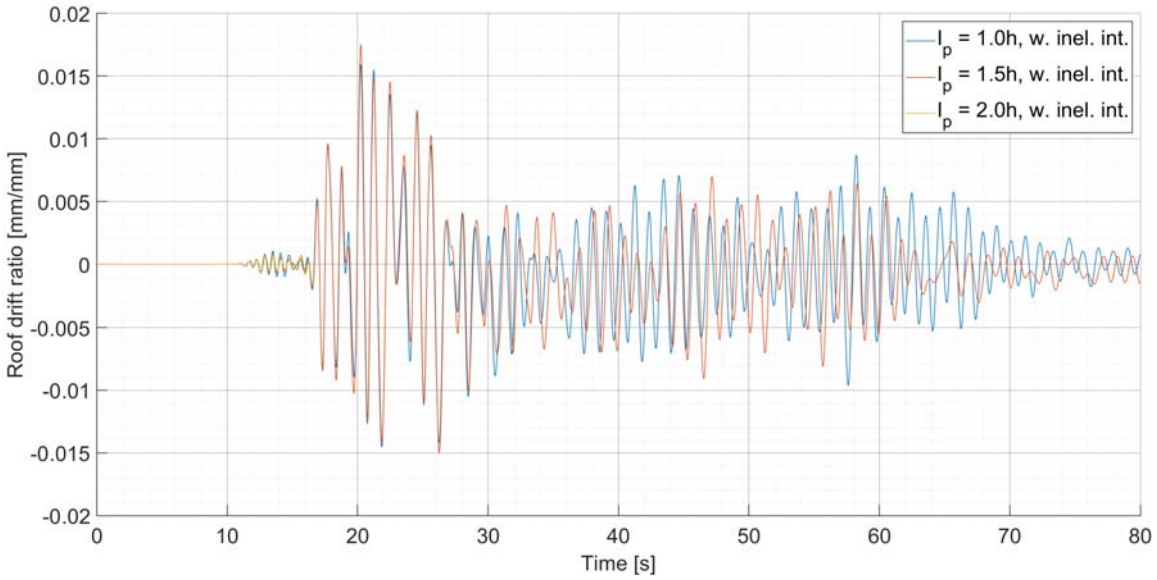


**Figure E.7:** Response histories using the BwH model with inelastic interior for node 43. 1110 Kobe.

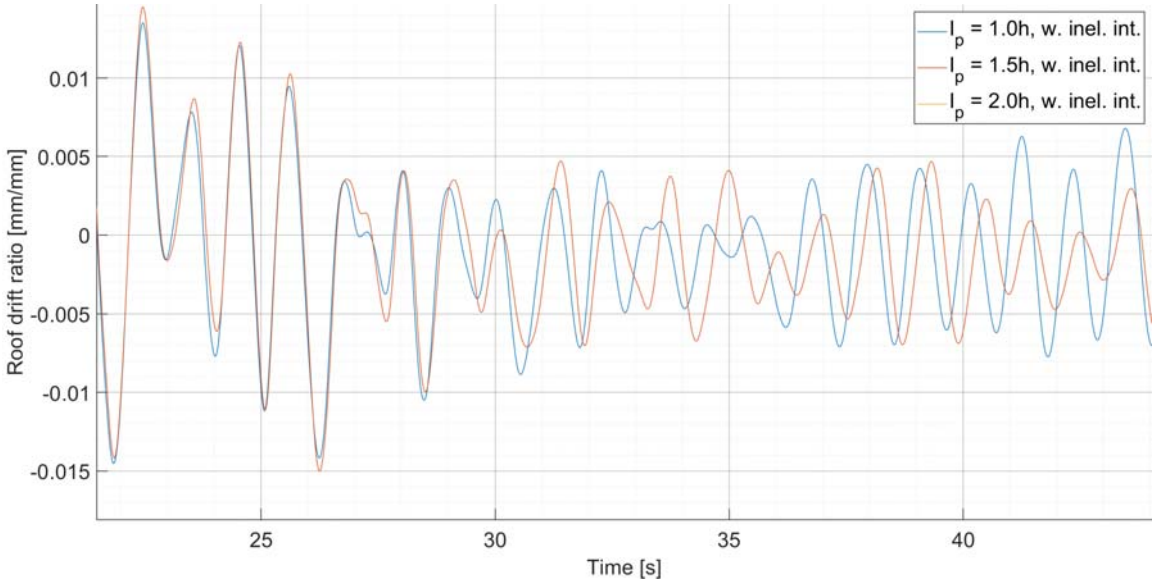


**Figure E.8:** Response histories using the BwH model with inelastic interior for node 43. 1110 Kobe.

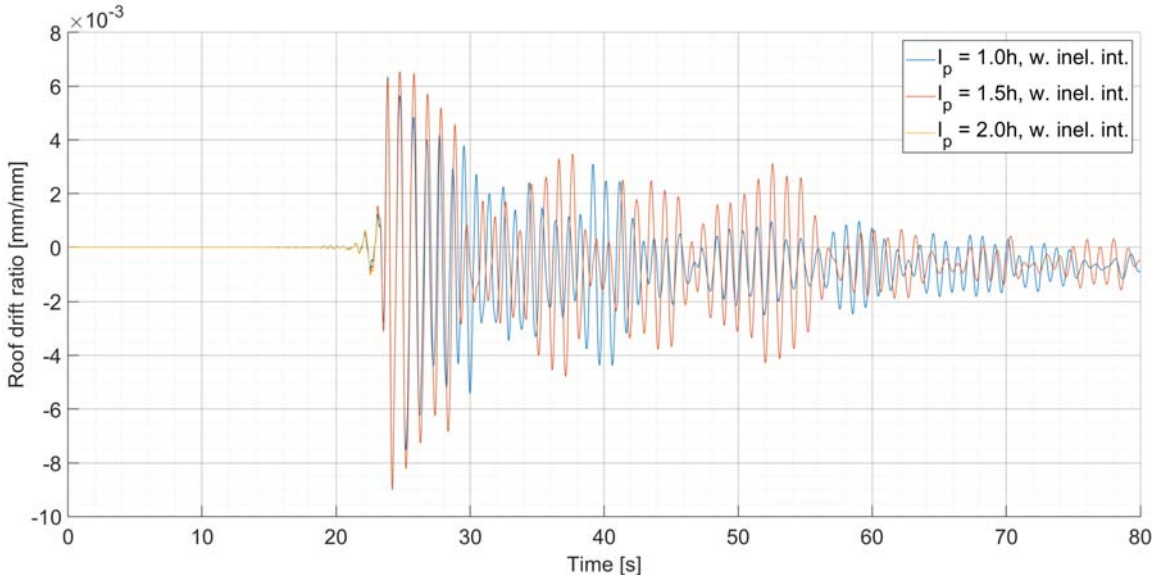


**Figure E.9:** Response histories using the BwH model with inelastic interior for node 43. 4889 Chuetsu-Oki.

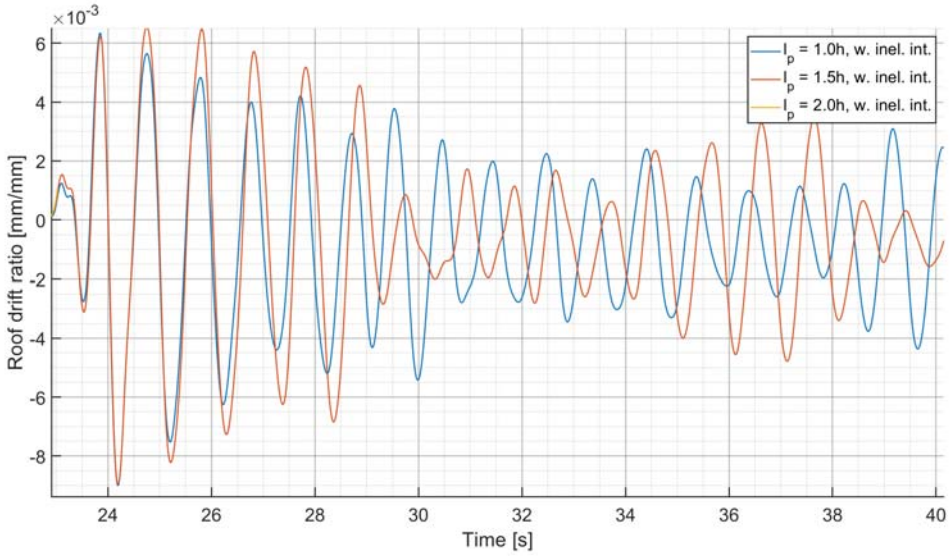


**Figure E.10:** Response histories using the BwH model with inelastic interior for node 43. 4889 Chuetsu-Oki.

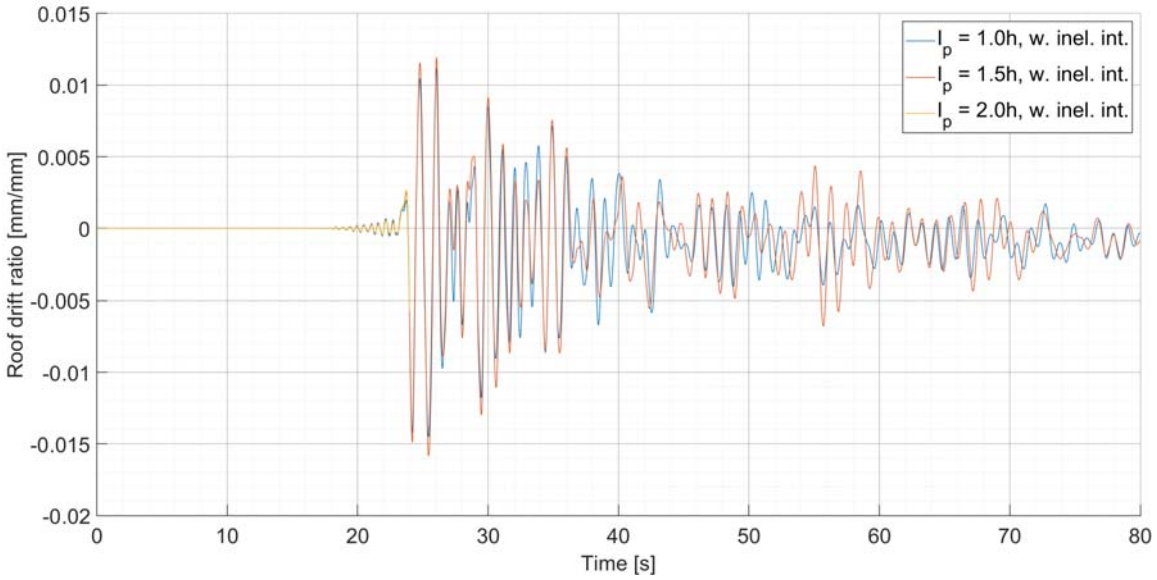


**Figure E.11:** Response histories using the BwH model with inelastic interior for node 43. 5814 Iwate.

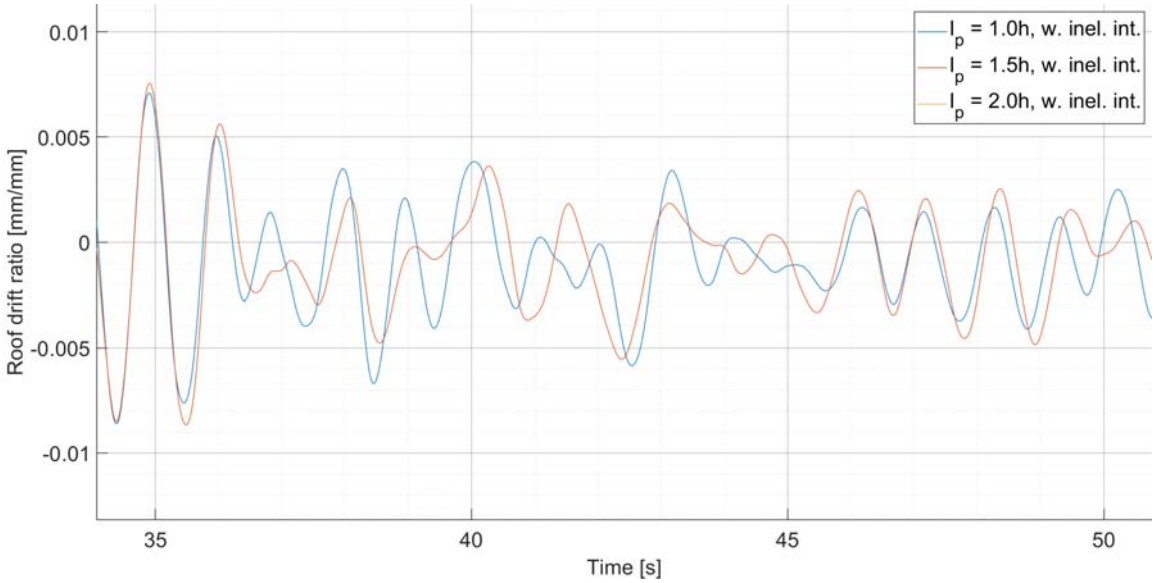


**Figure E.12:** Response histories using the BwH model with inelastic interior for node 43. 5814 Iwate.

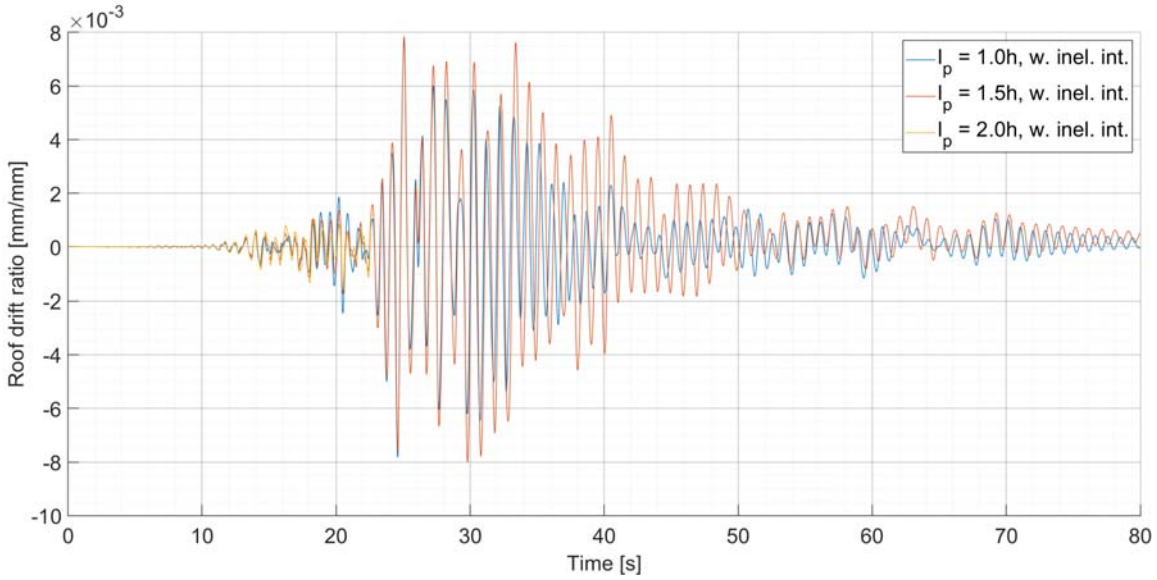


**Figure E.13:** Response histories using the BwH model with inelastic interior for node 43. 6923 Darfield.

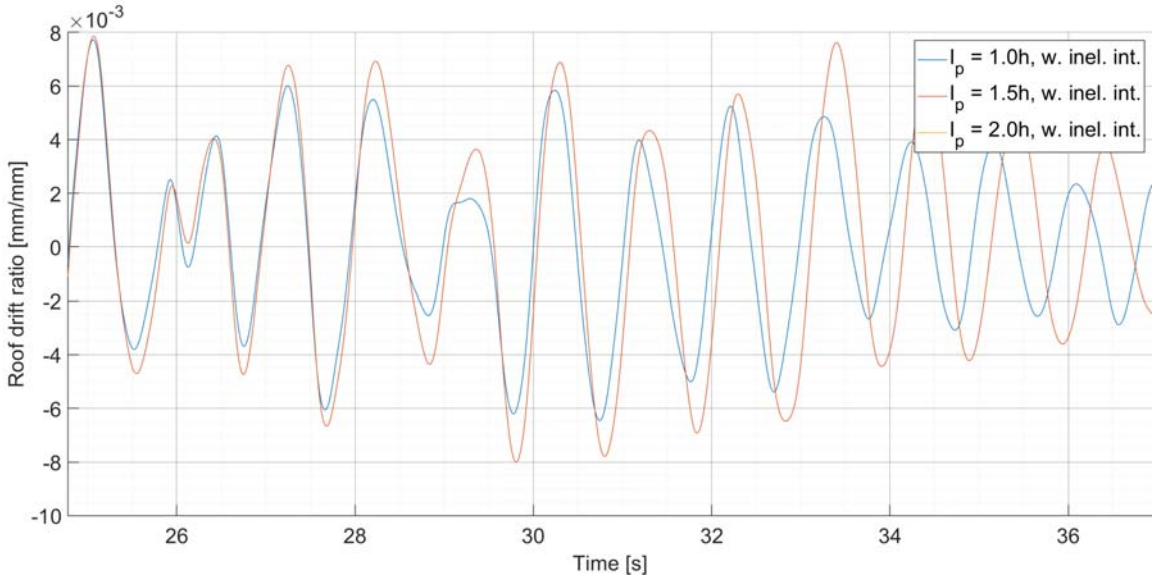


**Figure E.14:** Response histories using the BwH model with inelastic interior for node 43. 6923 Darfield.

# Appendix F

# Inter-story drift ratios (IDR)

The following is a presentation of the IDR profiles for the different models and ground motions. The IDRs are sampled at the time where the peak roof drift is reached.

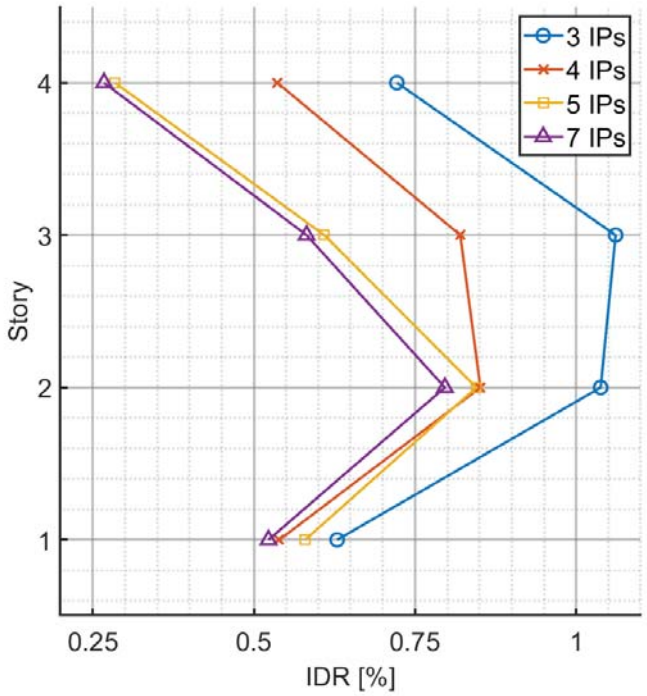


**Figure F.1:** IDRs for the FB model response to the Trinidad ground motions.

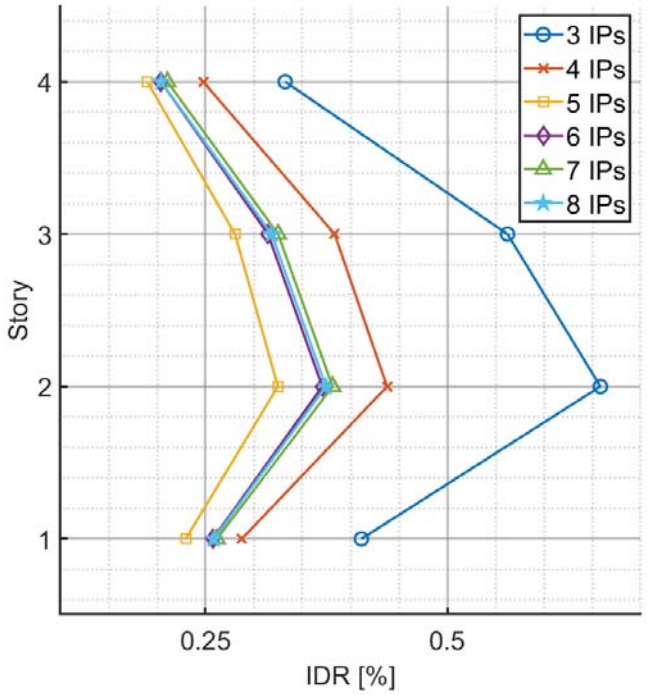


**Figure F.2:** IDRs for the FB model response to the Superstition Hills ground motions.

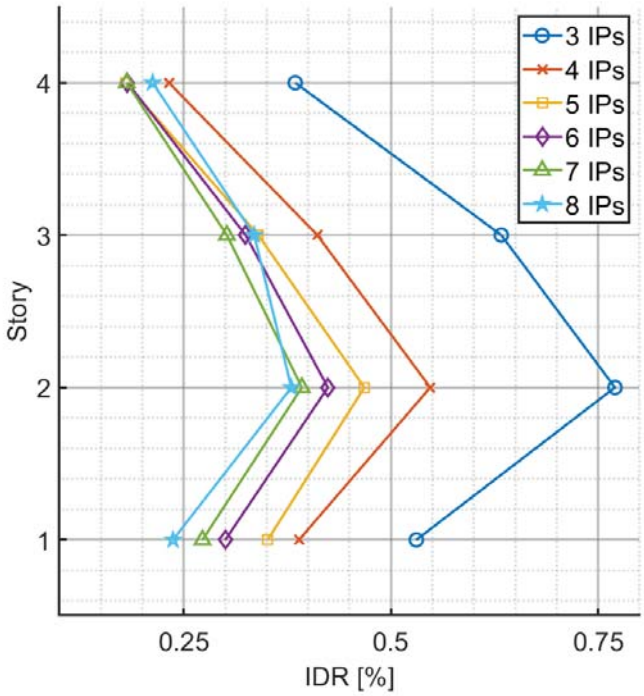


**Figure F.3:** IDRs for the FB model response to the Northridge ground motions.

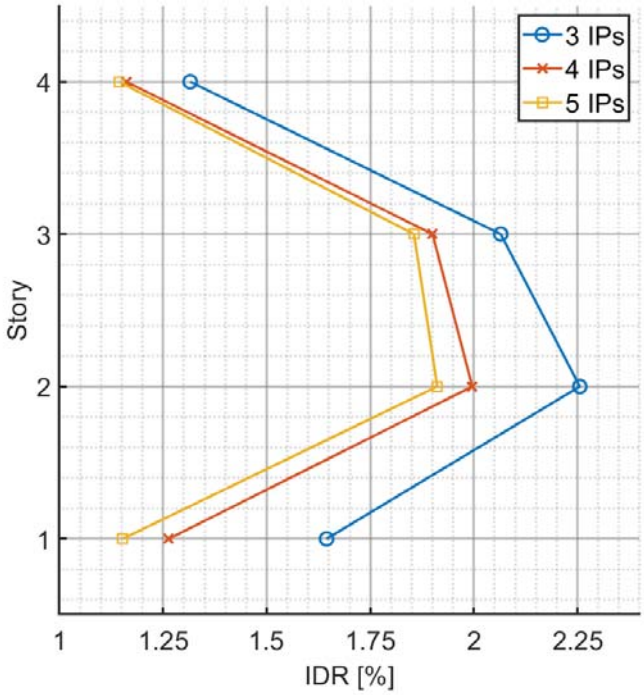


**Figure F.4:** IDRs for the FB model response to the Kobe ground motions.

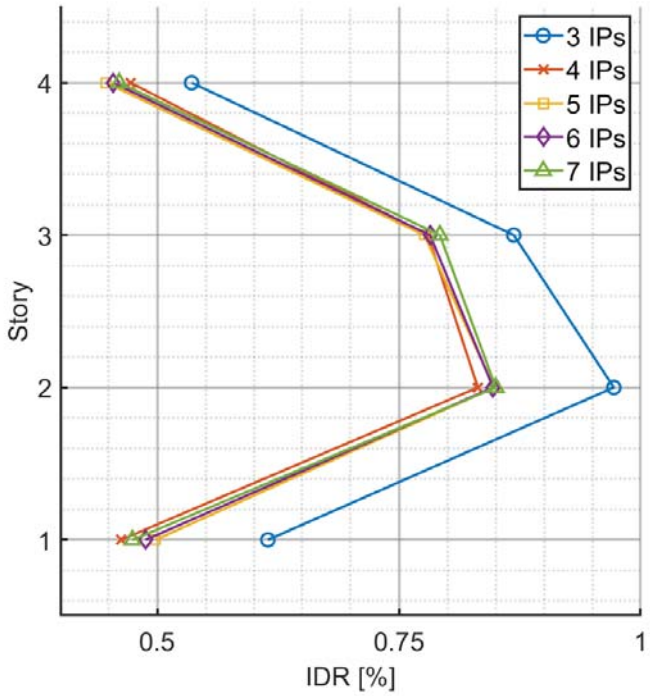


**Figure F.5:** IDRs for the FB model response to the Chuetsu-Oki ground motions.

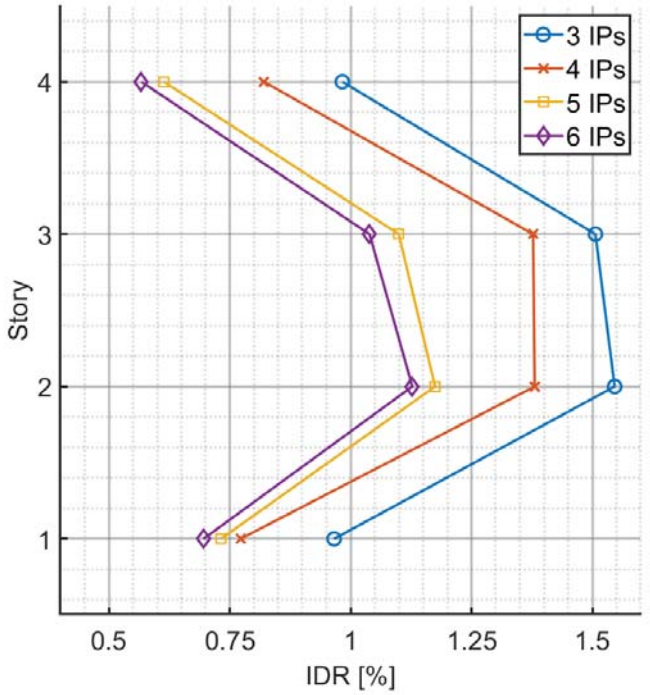


**Figure F.6:** IDRs for the FB model response to the Iwate ground motions.

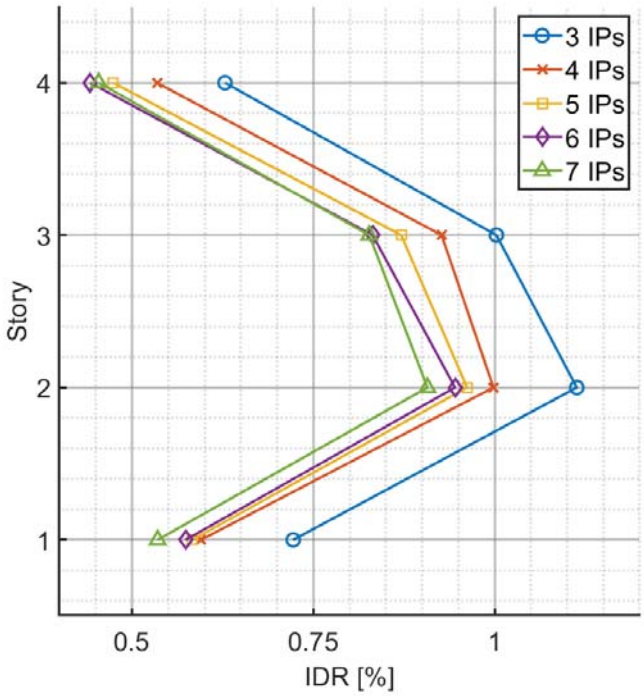


**Figure F.7:** IDRs for the FB model response to the Darfield ground motions.

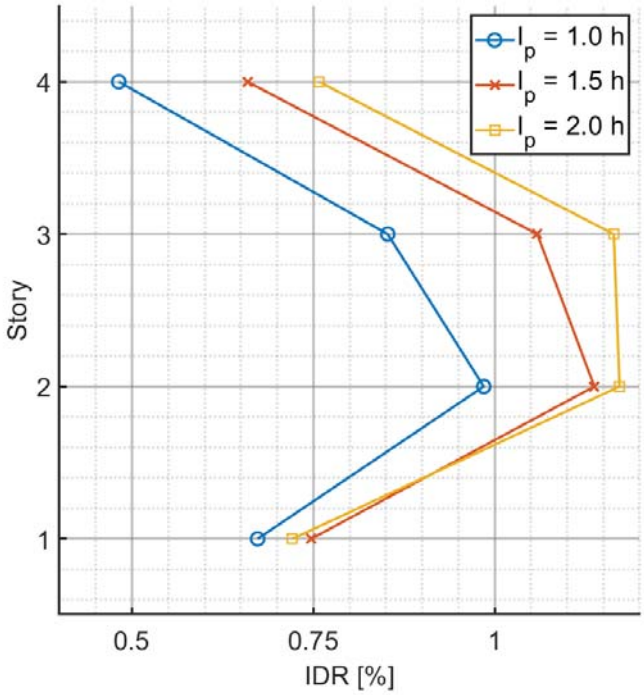


**Figure F.8:** IDRs for the response of the BwH model using the elastic interior to the Trinidad ground motions.

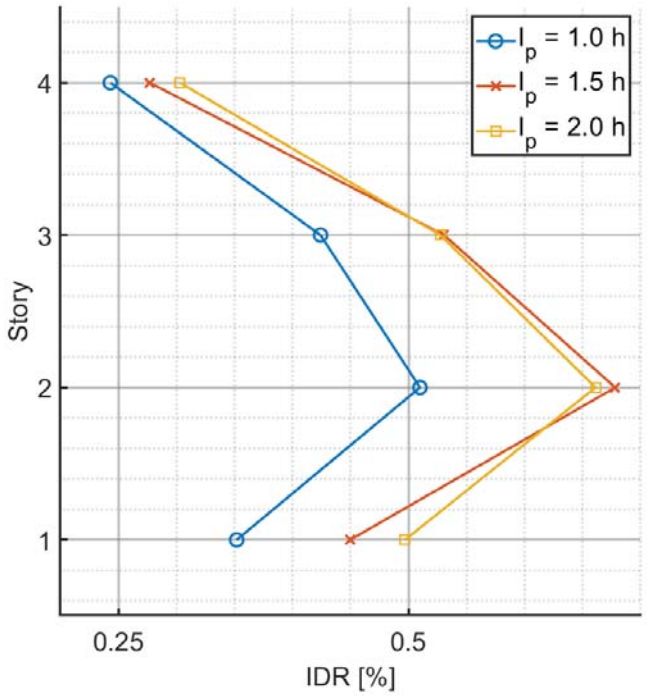


**Figure F.9:** IDRs for the response of the BwH model using the elastic interior to the Superstition Hills ground motions.

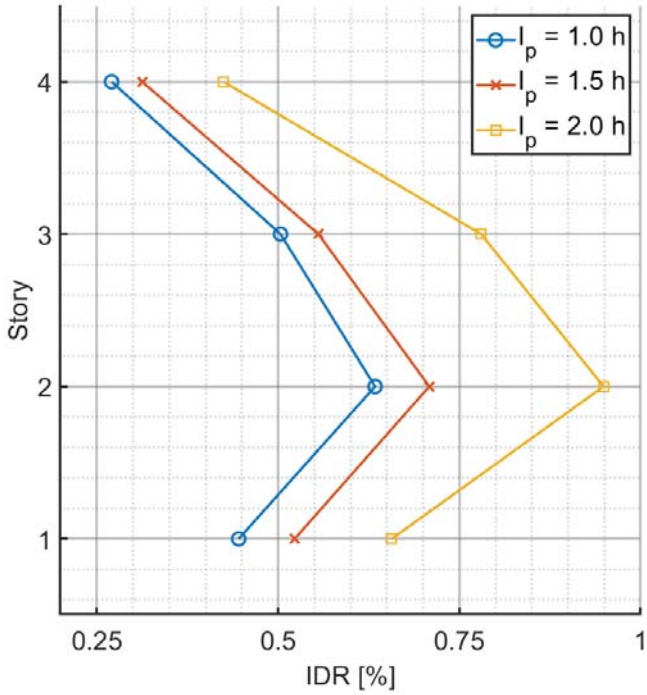


**Figure F.10:** IDRs for the response of the BwH model using the elastic interior to the Northridge ground motions.

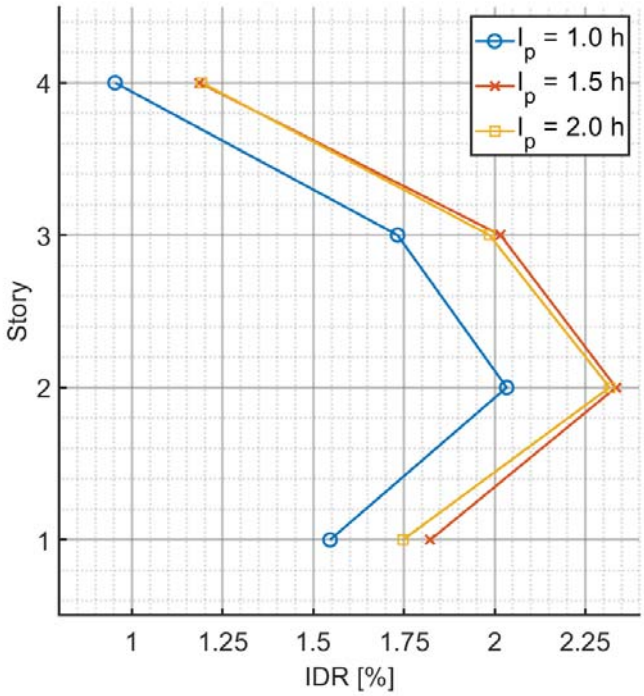


**Figure F.11:** IDRs for the response of the BwH model using the elastic interior to the Kobe ground motions.

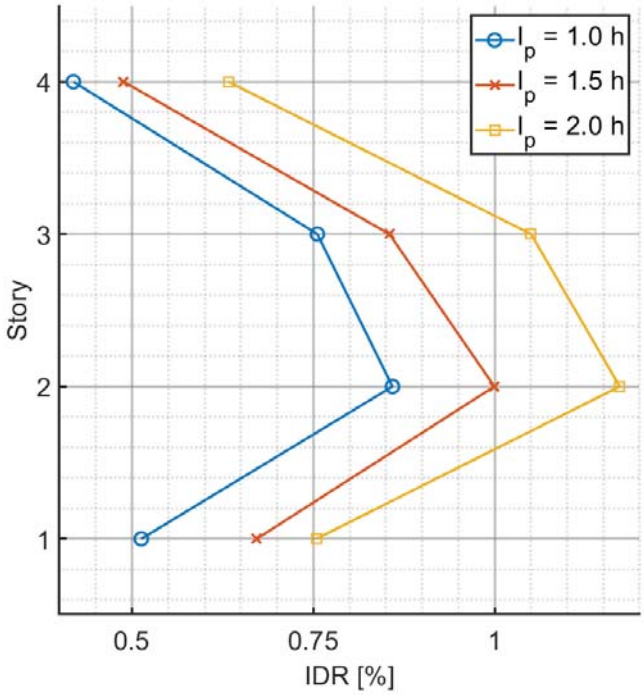


**Figure F.12:** IDRs for the response of the BwH model using the elastic interior to the Chuetsu-Oki ground motions.

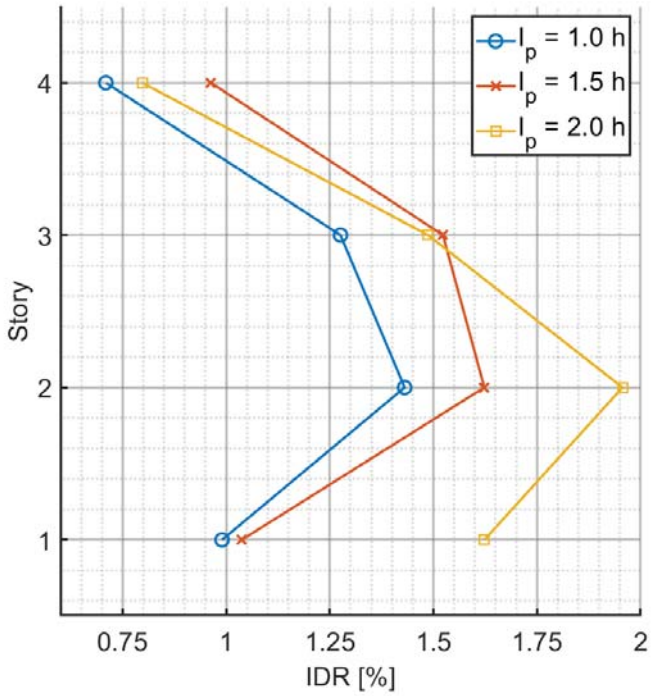


**Figure F.13:** IDRs for the response of the BwH model using the elastic interior to the Iwate ground motions.

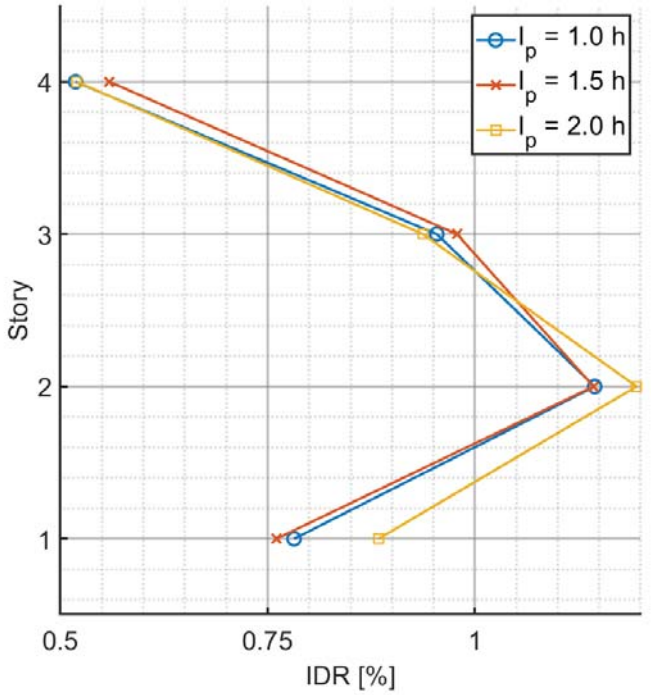


**Figure F.14:** IDRs for the response of the BwH model using the elastic interior to the Darfield ground motions.

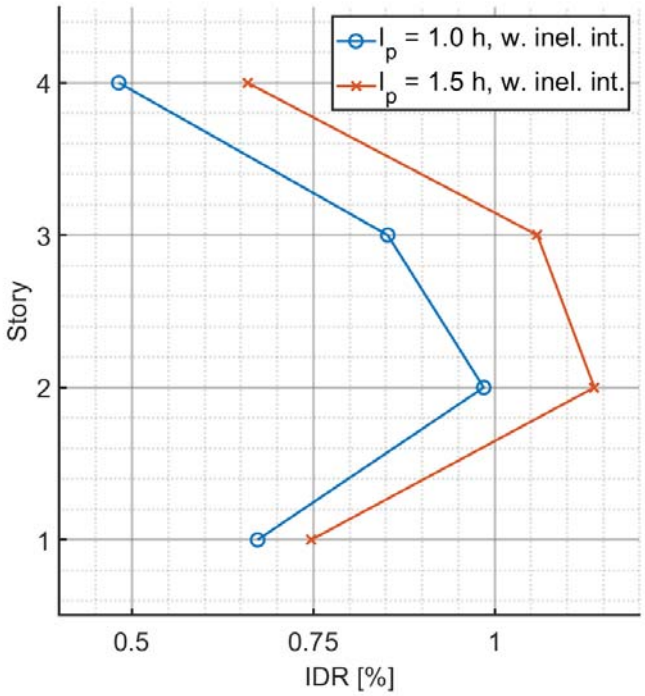


**Figure F.15:** IDRs for the response of the BwH model using the inelastic interior to the Trinidad ground motions.

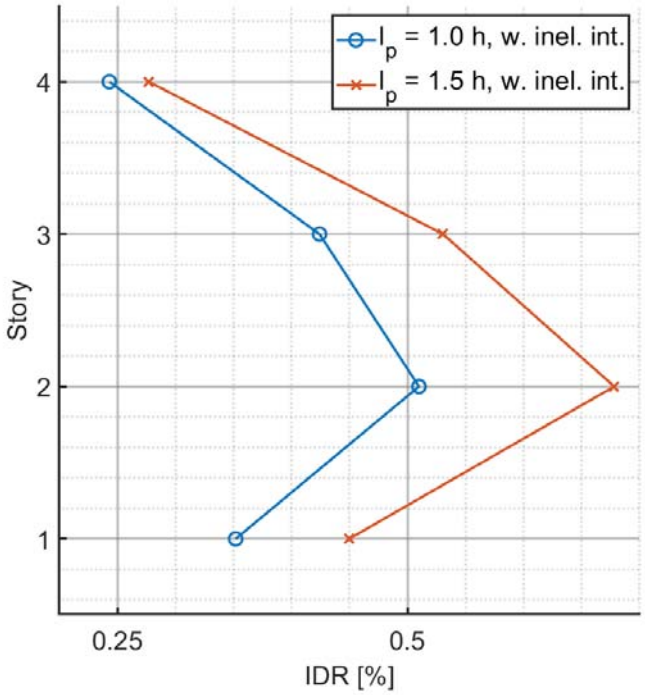


**Figure F.16:** IDRs for the response of the BwH model using the inelastic interior to the Superstition Hills ground motions.

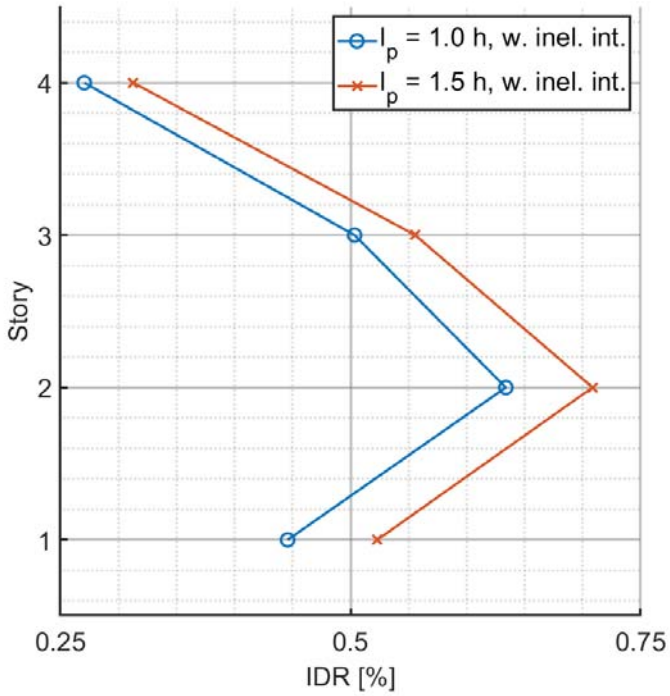


**Figure F.17:** IDRs for the response of the BwH model using the inelastic interior to the Northridge ground motions.

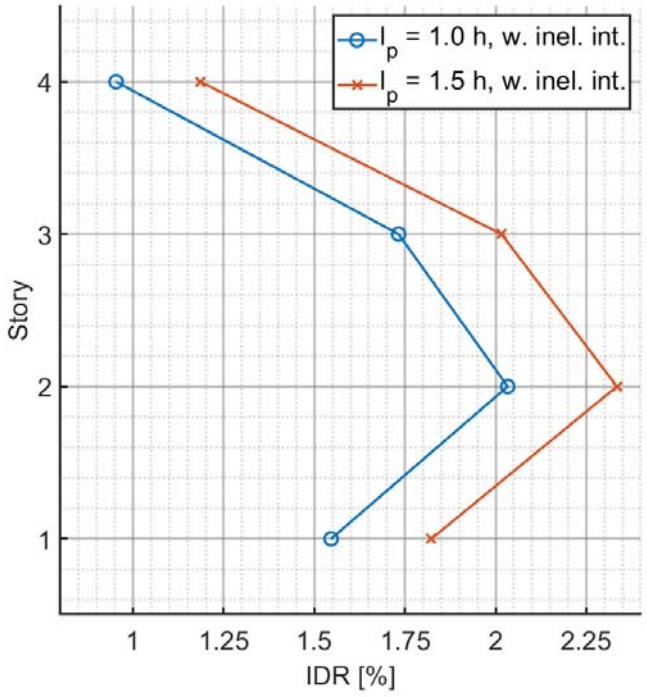


**Figure F.18:** IDRs for the response of the BwH model using the inelastic interior to the Kobe ground motions.

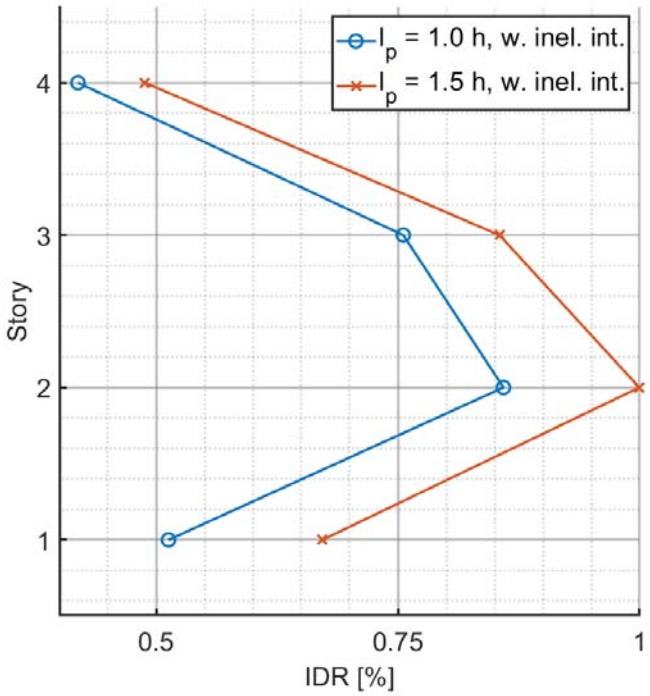


**Figure F.19:** IDRs for the response of the BwH model using the inelastic interior to the Chuetsu-Oki ground motions.

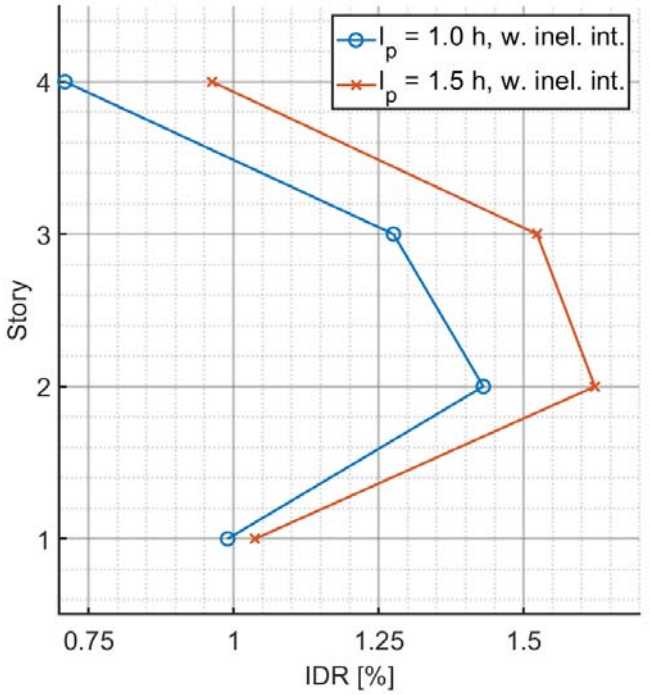


**Figure F.20:** IDRs for the response of the BwH model using the inelastic interior to the Iwate ground motions.

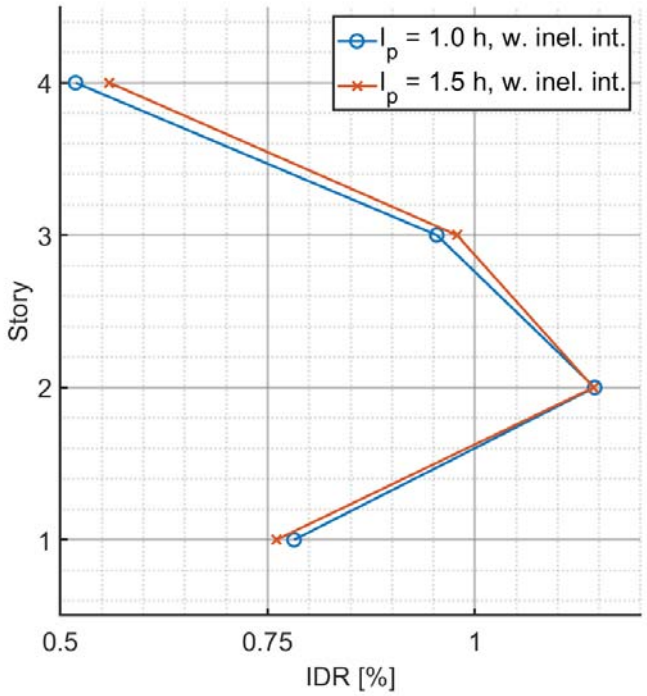


**Figure F.21:** IDRs for the response of the BwH model using the inelastic interior to the Darfield ground motions.

# Appendix G

# Scaling in Matlab

In this appendix, the script used to import, make and scale response spectra in Matlab is presented.

```
clc
close all
clear all

%% Load data

    TRIN_0282_H1_A_temp1 = dlmread('RSN282_TRINIDAD.B_B-RDW000.AT2');       TRIN_0282_H1_A_temp2 = transpose↙
(TRIN_0282_H1_A_temp1); TRIN_0282_H1_A = 9.81*(TRIN_0282_H1_A_temp2(:)); clearvars TRIN_0282_H1_A_temp1↙
TRIN_0282_H1_A_temp2
    TRIN_0282_H2_A_temp1 = dlmread('RSN282_TRINIDAD.B_B-RDW270.AT2');       TRIN_0282_H2_A_temp2 = transpose↙
(TRIN_0282_H2_A_temp1); TRIN_0282_H2_A = 9.81*(TRIN_0282_H2_A_temp2(:)); clearvars TRIN_0282_H2_A_temp1↙
TRIN_0282_H2_A_temp2
    TRIN_0282_UP_A_temp1 = dlmread('RSN282_TRINIDAD.B_B-RDW-UP.AT2');       TRIN_0282_UP_A_temp2 = transpose↙
(TRIN_0282_UP_A_temp1); TRIN_0282_UP_A = 9.81*(TRIN_0282_UP_A_temp2(:)); clearvars TRIN_0282_UP_A_temp1↙
TRIN_0282_UP_A_temp2

    SUPE_0720_H1_A_temp1 = dlmread('RSN720_SUPER.B_B-CAL225.AT2');          SUPE_0720_H1_A_temp2 = transpose↙
(SUPE_0720_H1_A_temp1); SUPE_0720_H1_A = 9.81*(SUPE_0720_H1_A_temp2(:)); clearvars SUPE_0720_H1_A_temp1↙
SUPE_0720_H1_A_temp2
    SUPE_0720_H2_A_temp1 = dlmread('RSN720_SUPER.B_B-CAL315.AT2');          SUPE_0720_H2_A_temp2 = transpose↙
(SUPE_0720_H2_A_temp1); SUPE_0720_H2_A = 9.81*(SUPE_0720_H2_A_temp2(:)); clearvars SUPE_0720_H2_A_temp1↙
SUPE_0720_H2_A_temp2

    NORT_1003_H1_A_temp1 = dlmread('RSN1003_NORTHR_STN020.AT2');            NORT_1003_H1_A_temp2 = transpose↙
(NORT_1003_H1_A_temp1); NORT_1003_H1_A = 9.81*(NORT_1003_H1_A_temp2(:)); clearvars NORT_1003_H1_A_temp1↙
NORT_1003_H1_A_temp2
    NORT_1003_H2_A_temp1 = dlmread('RSN1003_NORTHR_STN110.AT2');            NORT_1003_H2_A_temp2 = transpose↙
(NORT_1003_H2_A_temp1); NORT_1003_H2_A = 9.81*(NORT_1003_H2_A_temp2(:)); clearvars NORT_1003_H2_A_temp1↙
NORT_1003_H2_A_temp2
    NORT_1003_UP_A_temp1 = dlmread('RSN1003_NORTHR_STN-UP.AT2');            NORT_1003_UP_A_temp2 = transpose↙
(NORT_1003_UP_A_temp1); NORT_1003_UP_A = 9.81*(NORT_1003_UP_A_temp2(:)); clearvars NORT_1003_UP_A_temp1↙
NORT_1003_UP_A_temp2

    KOBE_1110_H1_A_temp1 = dlmread('RSN1110_KOBE_MRG000.AT2');              KOBE_1110_H1_A_temp2 = transpose↙
```

```
(KOBE_1110_H1_A_temp1); KOBE_1110_H1_A = 9.81*(KOBE_1110_H1_A_temp2(:)); clearvars KOBE_1110_H1_A_temp1↙
KOBE_1110_H1_A_temp2
    KOBE_1110_H2_A_temp1 = dlmread('RSN1110_KOBE_MRG090.AT2');              KOBE_1110_H2_A_temp2 = transpose↙
(KOBE_1110_H2_A_temp1); KOBE_1110_H2_A = 9.81*(KOBE_1110_H2_A_temp2(:)); clearvars KOBE_1110_H2_A_temp1↙
KOBE_1110_H2_A_temp2
    KOBE_1110_UP_A_temp1 = dlmread('RSN1110_KOBE_MRG-UP.AT2');              KOBE_1110_UP_A_temp2 = transpose↙
(KOBE_1110_UP_A_temp1); KOBE_1110_UP_A = 9.81*(KOBE_1110_UP_A_temp2(:)); clearvars KOBE_1110_UP_A_temp1↙
KOBE_1110_UP_A_temp2

    CHUE_4889_H1_A_temp1 = dlmread('RSN4889_CHUETSU_6E1C1EW.AT2');          CHUE_4889_H1_A_temp2 = transpose↙
(CHUE_4889_H1_A_temp1); CHUE_4889_H1_A = 9.81*(CHUE_4889_H1_A_temp2(:)); clearvars CHUE_4889_H1_A_temp1↙
CHUE_4889_H1_A_temp2
    CHUE_4889_H2_A_temp1 = dlmread('RSN4889_CHUETSU_6E1C1NS.AT2');          CHUE_4889_H2_A_temp2 = transpose↙
(CHUE_4889_H2_A_temp1); CHUE_4889_H2_A = 9.81*(CHUE_4889_H2_A_temp2(:)); clearvars CHUE_4889_H2_A_temp1↙
CHUE_4889_H2_A_temp2
    CHUE_4889_UP_A_temp1 = dlmread('RSN4889_CHUETSU_6E1C1UD.AT2');          CHUE_4889_UP_A_temp2 = transpose↙
(CHUE_4889_UP_A_temp1); CHUE_4889_UP_A = 9.81*(CHUE_4889_UP_A_temp2(:)); clearvars CHUE_4889_UP_A_temp1↙
CHUE_4889_UP_A_temp2

    IWAT_5814_H1_A_temp1 = dlmread('RSN5814_IWATE_44B91EW.AT2');        IWAT_5814_H1_A_temp2 = transpose↙
(IWAT_5814_H1_A_temp1); IWAT_5814_H1_A = 9.81*(IWAT_5814_H1_A_temp2(:)); clearvars IWAT_5814_H1_A_temp1↙
IWAT_5814_H1_A_temp2
    IWAT_5814_H2_A_temp1 = dlmread('RSN5814_IWATE_44B91NS.AT2');        IWAT_5814_H2_A_temp2 = transpose↙
(IWAT_5814_H2_A_temp1); IWAT_5814_H2_A = 9.81*(IWAT_5814_H2_A_temp2(:)); clearvars IWAT_5814_H2_A_temp1↙
IWAT_5814_H2_A_temp2
    IWAT_5814_UP_A_temp1 = dlmread('RSN5814_IWATE_44B91UD.AT2');        IWAT_5814_UP_A_temp2 = transpose↙
(IWAT_5814_UP_A_temp1); IWAT_5814_UP_A = 9.81*(IWAT_5814_UP_A_temp2(:)); clearvars IWAT_5814_UP_A_temp1↙
IWAT_5814_UP_A_temp2

    DARF_6923_H1_A_temp1 = dlmread('RSN6923_DARFIELD_KPOCN15E.AT2');        DARF_6923_H1_A_temp2 = transpose↙
(DARF_6923_H1_A_temp1); DARF_6923_H1_A = 9.81*(DARF_6923_H1_A_temp2(:)); clearvars DARF_6923_H1_A_temp1↙
DARF_6923_H1_A_temp2
    DARF_6923_H2_A_temp1 = dlmread('RSN6923_DARFIELD_KPOCS75E.AT2');        DARF_6923_H2_A_temp2 = transpose↙
(DARF_6923_H2_A_temp1); DARF_6923_H2_A = 9.81*(DARF_6923_H2_A_temp2(:)); clearvars DARF_6923_H2_A_temp1↙
```

```
DARF_6923_H2_A_temp2
    DARF_6923_UP_A_temp1 = dlmread('RSN6923_DARFIELD_KPOCUP.AT2');          DARF_6923_UP_A_temp2 = transpose↙
(DARF_6923_UP_A_temp1); DARF_6923_UP_A = 9.81*(DARF_6923_UP_A_temp2(:)); clearvars DARF_6923_UP_A_temp1↙
DARF_6923_UP_A_temp2

%% Defining cellArray for accelerations
    % record gives names, dT and then acceleration records in m/s^2

    Arecords = {'TRINIDAD RSN0282'               0.005 TRIN_0282_H1_A TRIN_0282_H2_A TRIN_0282_UP_A;...
                'SUPERSTITION HILLS-02 RNS0720' 0.010 SUPE_0720_H1_A SUPE_0720_H2_A {};...
                'NORTHRIDGE-01 RSN1003'          0.010 NORT_1003_H1_A NORT_1003_H2_A NORT_1003_UP_A;...
                'KOBE RSN1110'                   0.010 KOBE_1110_H1_A KOBE_1110_H2_A KOBE_1110_UP_A;...
                'CHUETSU-OKI RSN4889'            0.010 CHUE_4889_H1_A CHUE_4889_H2_A CHUE_4889_UP_A;...
                'IWATE RSN5814'                  0.010 IWAT_5814_H1_A IWAT_5814_H2_A IWAT_5814_UP_A;...
                'DARFIELD RSN6923'               0.005 DARF_6923_H1_A DARF_6923_H2_A DARF_6923_UP_A};

clearvars('-except', 'Arecords');

%% Formating

    % Finding maximum absolute values and length of recording

        facts_Arecords_H1{size(Arecords,1), 2}= [];
        for i = 1:size(Arecords,1)
            facts_Arecords_H1{i,1} = max(abs(Arecords{i,3}));
            facts_Arecords_H1{i,2} = length(Arecords{i,3});
        end; clearvars i

    % Finding maximum ground motion length for all records

        longestLength = max([facts_Arecords_H1{:,2}]);

    % Create time arrays over the longestLength with the respective time steps
    time_Arecords_H1{size(Arecords,1), 1} = [];
```

```
    nn = zeros(1,size(Arecords,1));
    for i = 1:size(Arecords,1)
        nn(i) = longestLength/[Arecords{i,2}];
        time_Arecords_H1{i,1} = transpose(linspace(0,longestLength,nn(i)+1));
    end; clearvars i nn

%% Plot ground motions
    for i = 1:size(Arecords,1)
    figure('name',Arecords{i,1})
        aa = time_Arecords_H1{i,1};
        bb = Arecords{i,3};
        plot(aa(1:length(bb),1).',bb.','-','color',[0 0 0]);
        xlabel('Time [s]');
        ylabel('Acceleration [m/s^2]')

        legend(Arecords{i,1})
        ylimit = 1.05*max(abs(bb));
        ylim([-ylimit,ylimit])

        grid on
        grid minor

        ax = gca;
        ax.GridColor = [.5 .5 .5];
        ax.MinorGridColor = [.5 .5 .5];
%         ax.XTick = 0:0.25e-4:2.5e-4;
        ax.YTick = -5:1:5;
        ax.GridLineStyle = '-';
        ax.MinorGridLineStyle = ':';
        ax.GridAlpha = 0.5;
        ax.MinorGridAlpha = .25;
        ax.Layer = 'bot';
    end; clearvars i aa bb
```

```
%% Computation of reponse spectrum by
    %   - Newmarks linear method
    %   - Constant average acceleration method (gamma=1/2, beta=1/4)
    %   - Linear acceleration method (gamma=1/2, beta=1/6)

    % Procedure constants. Note: For a stable solution, 2betta > gamma > 0.5
    gamma = 0.5;
    beta = 1/6;

    m = 1;          % Mass is set equal to one and the stiffness is varied.
    psi = 0.05;     % Determine damping.
    Tmax = 4;       % Determine maxiumum period


        % Preallocations

    for i = 1:size(Arecords,1)
        Arecord = Arecords{i,3};

        dt = Arecords{i,2};
        u = zeros(size(Arecord));
        v = u;
        a = u;
        T(1,1) = 0;

            % Preallocations
            dT = Tmax/dt;
            omega = zeros(length(linspace(0, Tmax, dT+1)),1);
        for j = 1:dT
            omega(j,1) = 2*pi*(1/T(j,1));
            k = (omega(j))^2*m;
            c = 2*psi*omega(j)*m;
            a1 = (gamma/(beta*dt))*c+(1/(beta*dt^2))*m;
            a2 = (1/(beta*dt))*m+((gamma/beta)-1)*c;
```

```
        a3 = ((gamma/(2*beta))-1)*c*dt+((1/(2*beta))-1)*m;
        keff = k+a1;
        for k = 1:length(u)-1
            Ph = -Arecord(k+1)*m+a1*u(k,1)+a2*v(k,1)+a3*a(k,1);
            u(k+1,1) = Ph/keff;
            v(k+1,1) = (gamma/(beta*dt))*(u(k+1,1)-u(k,1))+(1-(gamma/beta))*v(k,1)+dt*(1-(gamma/(2*beta)))*a(k,1);
            a(k+1,1) = (1/(beta*dt^2))*(u(k+1,1)-u(k,1))-(1/(beta*dt))*v(k,1)-((1/(2*beta))-1)*a(k,1);
        end

        Sd(j,1) = max(abs(u));
        Sv(j,1) = max(abs(v));
        Sa(j,1) = Sd(j,1)*(omega(j))^2;

        T(j+1,1) = T(j)+dt;
    end; T(end) = [];

    % These manual values ensure continuty in the spectrum
    Sd(1:2,1) = 0;
    Sv(1:2,1) = 0;
    Sa(1:3,1) = max(abs(Arecord));

    PGA_EC8 = 3.5;
    PSA_EC8 = 10.06;

    Tn_location = find(abs(T-0.51) < 0.001); % OS 0.21

    Spectrums{i,3} = PGA_EC8/Sa(1,1);
    Spectrums{i,5} = PSA_EC8/Sa(Tn_location,1);
    PGA_Sa = Sa*(PGA_EC8/Sa(1,1));  % Scaled Response acceleration to PGA
    TS_Sa = Sa*(PSA_EC8/Sa(Tn_location,1)); % Scaled Response acceleration to T

    Spectrums{i,1} = T;
    Spectrums{i,2} = Sa;
    Spectrums{i,4} = PGA_Sa;
```

```
        Spectrums{i,6} = TS_Sa;
        Spectrums{i,7} = Sv;
        Spectrums{i,8} = Sd;




        clearvars a a1 a2 a3 c dt i j k keff omega ph T u v Sd Sv Sa dT TS_Sa PGA_Sa Arecord Tn_location
    end

%% Plotting

    figure('name','Unscaled response spectrums')
    hold on;
    legendInfo = {};
    for i = 1:size(Arecords,1)
        plot(Spectrums{i,1}, Spectrums{i,2});
        legendInfo{i} = [Arecords{i,1}];
    end

    legend(legendInfo)

    xlim([0,2])

    xlabel('Natural Period [s]','FontSize',10');
    ylabel('Response [m/s^2]','FontSize',10')

    grid on
    grid minor

    ax = gca;
    ax.GridColor = [.5 .5 .5];
    ax.MinorGridColor = [.5 .5 .5];
```

```
%     ax.XTick = 0:0.25e-4:2.5e-4;
%     ax.YTick = 0:50:750;
    ax.GridLineStyle = '-';
    ax.MinorGridLineStyle = ':';
    ax.GridAlpha = 0.5;
    ax.MinorGridAlpha = .25;
    ax.Layer = 'bot';

    figure('name','Scaled response spectrums, PGA')
    hold on;
    legendInfo = {};
    for i = 1:size(Arecords,1)
        plot(Spectrums{i,1}, Spectrums{i,4});
        legendInfo{i} = [Arecords{i,1}];
    end

    legend(legendInfo)

    xlim([0,2])

    xlabel('Natural Period [s]','FontSize',10');
    ylabel('Response [m/s^2]','FontSize',10')

    grid on
    grid minor

    ax = gca;
    ax.GridColor = [.5 .5 .5];
    ax.MinorGridColor = [.5 .5 .5];
%     ax.XTick = 0:0.25e-4:2.5e-4;
%     ax.YTick = 0:50:750;
    ax.GridLineStyle = '-';
    ax.MinorGridLineStyle = ':';
    ax.GridAlpha = 0.5;
```

```
ax.MinorGridAlpha = .25;
ax.Layer = 'bot';

figure('name','Scaled response spectrums, T_1')
    hold on;
    legendInfo = {};
    for i = 1:size(Arecords,1)
        plot(Spectrums{i,1}, Spectrums{i,6});
        legendInfo{i} = [Arecords{i,1}];
    end
        %Plotting the mean of all the spectrums !!!!!!!!!!!!!!!!!!
        %Cusum an must be changed if Arecords is changed

        Spectrum1temp = Spectrums{1,6}; Spectrums_formeans(:,1) = Spectrum1temp(1:2:end,1);
        Spectrum2temp = Spectrums{2,6}; Spectrums_formeans(:,2) = Spectrum2temp;
        Spectrum3temp = Spectrums{3,6}; Spectrums_formeans(:,3) = Spectrum3temp;
        Spectrum4temp = Spectrums{4,6}; Spectrums_formeans(:,4) = Spectrum4temp;
        Spectrum5temp = Spectrums{5,6}; Spectrums_formeans(:,5) = Spectrum5temp;
        Spectrum6temp = Spectrums{6,6}; Spectrums_formeans(:,6) = Spectrum6temp;
        Spectrum7temp = Spectrums{7,6}; Spectrums_formeans(:,7) = Spectrum7temp(1:2:end,1);

        clearvars Spectrum1temp Spectrum2temp Spectrum3temp Spectrum4temp Spectrum5temp Spectrum6temp Spectrum7temp

        p0 = plot (Spectrums{2,1}, mean(Spectrums_formeans,2), 'color',[0 0 0], 'linewidth', 1.5)
        legendInfo{end+1} = 'Mean';



       %% Ec spectras
    S = 1.15;
    a_g = 3.5;

    T_B = 0.2;
    T_C = 0.6;
```

```
T_D = 2.0;

q = 3.9;

beta = 0.2;

eta = 1.0;
% Design spectra
p1= fplot(@(T) a_g*S*((2/3)+(T./T_B)*(2.5/q - 2/3)),            [0   T_B]   ,'-.k'); hold on
p5= fplot(@(T) a_g*S*(1+(T./T_B*(eta*2.5-1))),            [0   T_B]   ,'--k'); hold on
    fplot(@(T) a_g*S*2.5/q,                                       [T_B T_C]   ,'-.k'); hold on
    fplot(@(T) max(a_g*S*(2.5/q)*(T_C./T), beta*a_g),             [T_C T_D]   ,'-.k'); hold on
    fplot(@(T) max(a_g*S*(2.5/q)*(T_C*T_D./T.^2), beta*a_g),      [T_D 4]     ,'-.k'); hold on

% Elastic spectra
%   p5= fplot(@(T) a_g*S*(1+(T./T_B*(eta*2.5-1))),            [0   T_B]   ,'--k'); hold on
    fplot(@(T) a_g*S*eta*2.5,                                 [T_B T_C]   ,'--k'); hold on
    fplot(@(T) a_g*S*eta*2.5*(T_C./T),                        [T_C T_D]   ,'--k'); hold on
    fplot(@(T) a_g*S*eta*2.5*(T_C*T_D./T.^2),                 [T_D 4]     ,'--k'); hold on


legendInfo{end+1} = 'Elastic response spectra';
legendInfo{end+1} = 'Design response spectra';

legend(legendInfo)

xlim([0 2])

xlabel('Natural Period [s]','FontSize',10');
ylabel('Response [m/s^2]','FontSize',10')

grid on
grid minor
```

```
        ax = gca;
        ax.GridColor = [.5 .5 .5];
        ax.MinorGridColor = [.5 .5 .5];
        ax.GridLineStyle = '-';
        ax.MinorGridLineStyle = ':';
        ax.GridAlpha = 0.5;
        ax.MinorGridAlpha = .25;
        ax.Layer = 'bot';

        clearvars S q p1 p0 p5 T_B T_C T_D eta a_g

    for i = 1:size(Arecords,1)
      figure('name',['Response spectrums, ' Arecords{i,1}])
        hold on;
        legendInfo = {};

        plot(Spectrums{i,1}, Spectrums{i,2});
        plot(Spectrums{i,1}, Spectrums{i,4});
        plot(Spectrums{i,1}, Spectrums{i,6});
        legend

        legend( 'Unscaled', ' Scaled, PGA', 'Scaled, T_1')

        xlim([0,2])

        xlabel('Natural Period [s]','FontSize',10');
        ylabel('Response [m/s^2]','FontSize',10')

        grid on
        grid minor

        ax = gca;
        ax.GridColor = [.5 .5 .5];
        ax.MinorGridColor = [.5 .5 .5];
```

```
%     ax.XTick = 0:0.25e-4:2.5e-4;
%     ax.YTick = 0:50:750;
    ax.GridLineStyle = '-';
    ax.MinorGridLineStyle = ':';
    ax.GridAlpha = 0.5;
    ax.MinorGridAlpha = .25;
    ax.Layer = 'bot';
end
clearvars m gamma beta psi Ph Tmax PGA_EC8 PSA_EC8 longestLength ax i ylimit legendInfo Spectrums_formeans
```

# Appendix H

# OpenSees - Defining DB elements

In this appendix, the OpenSees script used to define nodes and elements for the DB model is presented.

```
##Title:    Element definitions
#Author:    Jørgen Rosmo Roven
#Units:     Metric (mm, ton, N, sec)
#-------------------------------------------------------------------------------------------------

geomTransf Linear 1
geomTransf PDelta 2


# ta is given in the fomat (Beam=1/Col=2)(story)(columnrow)(numberofFiniteElement)

#Assembles internal beams
    # Runs for each story not including the uppermost story
        for {set nStory 2} {$nStory < $nZc} {incr nStory} {
            # Runs for all column rows exept the last - puts all finite elements on roof exept element number 0 and nFE
            for {set nColRow 1} {$nColRow < $nXc} {incr nColRow} {
                # Runs for all finite elements except last
                for {set deltax 1} {$deltax < $nFE-1} {incr deltax} {

                #   element dispBeamColumn $eleTag                      $nStory$nColRow$deltax  $nStory$nColRow[expr ↙
$deltax+1] $numIntgrPts $secTb30x50    1
                    element dispBeamColumn 1$nStory$nColRow$deltax          1$nStory$nColRow$deltax 1$nStory$nColRow[expr ↙
$deltax+1]    $numIntgrPts $secTb30x50    1
                }
                unset deltax
                set deltax 0
                # Puts first finite element number 0
                    element dispBeamColumn 1$nStory$nColRow$deltax          2$nStory$nColRow$deltax 1$nStory$nColRow[expr ↙
$deltax+1]    $numIntgrPts $secTb30x50    1
                unset deltax
            }
            unset nColRow

        # Runs for all column rows exept the last - puts all finite element nFE on roof for beams
```

```
            for {set nColRow 2} {$nColRow <= $nXc} {incr nColRow} {
                    set deltax [expr $nFE-1]
                    element dispBeamColumn 1$nStory[expr ${nColRow}-1]$deltax           1$nStory[expr ${nColRow}-1]$deltax ↙
2$nStory${nColRow}0 $numIntgrPts $secTb30x50    1
            }
            unset nColRow
        }
        unset nStory

# Assemble roof beams
    # Runs for all column rows exept the last - puts all finite elements on roof exept element number 0 and nFE
        for {set nColRow 1} {$nColRow < $nXc} {incr nColRow} {
            # Runs for all finite elements except last
            for {set deltax 1} {$deltax < $nFE-1} {incr deltax} {

            #   element dispBeamColumn $eleTag                      $nStory$nColRow$deltax  $nStory$nColRow[expr $deltax+1] ↙
$numIntgrPts $secTb30x50    1
                element dispBeamColumn 1$nZc$nColRow$deltax         1$nZc$nColRow$deltax    1$nZc$nColRow[expr $deltax+1] ↙
$numIntgrPts $secTb26x45    1
            }
            unset deltax
            set deltax 0
            # Puts first finite element number 0
            element dispBeamColumn 1$nZc$nColRow$deltax         2$nZc$nColRow$deltax    1$nZc$nColRow[expr $deltax+1] ↙
$numIntgrPts $secTb26x45    1
            unset deltax
        }
        unset nColRow

    # Runs for all column rows exept the last - puts all finite element nFE on roof for beams
        for {set nColRow 2} {$nColRow <= $nXc} {incr nColRow} {
                set deltax [expr $nFE-1]
                element dispBeamColumn 1$nZc[expr ${nColRow}-1]$deltax          1$nZc[expr ${nColRow}-1]$deltax ↙
2$nZc${nColRow}0    $numIntgrPts $secTb26x45    1
```

```
        }
        unset nColRow

# Runs for each column row exept the first and the last
    for {set nColRow 2} {$nColRow < $nXc} {incr nColRow} {

        # Runs for all z-coordinates but last (stories)
        for {set nStory 1} {$nStory < $nZc-1} {incr nStory} {

            # Runs for all finite elements except last
            for {set deltaz 0} {$deltaz < $nFE-1} {incr deltaz} {

            #   element dispBeamColumn 2$nStory$nColRow$deltaz              $node i                          $node j ↙
$numIntgrPts $secTag        geomTransf
                element dispBeamColumn 2$nStory$nColRow$deltaz              2$nStory$nColRow$deltaz ↙
2$nStory$nColRow[expr $deltaz+1]    $numIntgrPts $secTc50x50    2
            }
            unset deltaz
                element dispBeamColumn 2$nStory$nColRow[expr $nFE-1]        2$nStory$nColRow[expr $nFE-1]   2[expr ↙
$nStory+1]${nColRow}0        $numIntgrPts $secTc50x50    2
        }
        unset
        # Runs for last z-coordinate (story)
        for {set nStory [expr $nZc-1]} {$nStory < $nZc} {incr nStory} {

            # Runs for all finite elements except last
            for {set deltaz 0} {$deltaz < $nFE-1} {incr deltaz} {

            #   element dispBeamColumn 2$nStory$nColRow$deltaz              $node i                          $node j ↙
$numIntgrPts $secTag        geomTransf
                element dispBeamColumn 2$nStory$nColRow$deltaz              2$nStory$nColRow$deltaz ↙
2$nStory$nColRow[expr $deltaz+1]    $numIntgrPts $secTc50x50    2
            }
            unset deltaz
```

```
        }
        # Create uppermost column elements in last story
        unset nStory
        set nStory [expr $nZc-1]
        #   element dispBeamColumn 2$nStory$nColRow$deltaz                  $node i                          $node j ↙
$numIntgrPts $secTag        geomTransf
                element dispBeamColumn 2$nStory$nColRow[expr $nFE-1]        2$nStory$nColRow[expr $nFE-1]   2[expr ↙
$nStory+1]${nColRow}0        $numIntgrPts $secTc45x45    2
        unset nStory
    }
    unset nColRow

# Creates all colums in the first and the last column row

    # Runs for all z-coordinates (stories)
    for {set nStory 1} {$nStory < $nZc} {incr nStory} {
        # Runs for all finite elements except last
        for {set deltaz 0} {$deltaz < $nFE-1} {incr deltaz} {


        #   element dispBeamColumn $eleTag                      $node i                     $node j ↙
$numIntgrPts $secTag        geomTransf
            element dispBeamColumn 2${nStory}1${deltaz}         2${nStory}1${deltaz}        2${nStory}1[expr $deltaz+1] ↙
$numIntgrPts $secTc45x45    2
            element dispBeamColumn 2${nStory}${nXc}${deltaz}    2${nStory}${nXc}${deltaz}   2${nStory}${nXc}[expr ↙
$deltaz+1]    $numIntgrPts $secTc45x45    2
        }



        # Creates elements last for-loop could not create
        #   element dispBeamColumn $eleTag                      $node i                     $node j ↙
$numIntgrPts $secTag        geomTransf
```

```
            element dispBeamColumn 2${nStory}1${deltaz}         2${nStory}1${deltaz}        2[expr ${nStory}+1]10 ↙
$numIntgrPts $secTc45x45    2
            element dispBeamColumn 2${nStory}${nXc}${deltaz}    2${nStory}${nXc}${deltaz}   2[expr ${nStory}+1]${nXc}0 ↙
$numIntgrPts $secTc45x45    2
    }
    unset nStory


puts "...Elements defined"
puts "      Each member is subdevided into $nFE finite elements."

##Title:    Node and nodal masses - 2D model of 4 storey 5 bay RC frame
#Author:    Jørgen Rosmo Roven
#Units:     Metric (mm, ton, N, sec)
#############################################################################################

############################################## Prog ##################################################

set nXc [llength $Xcoord]
set nZc [llength $Zcoord]

puts "Xcoord = $Xcoord has nXc = $nXc values"
puts "Zcoord = $Zcoord has nZc = $nZc values"
#puts ""

#set nodeTag $nStory$nColRow$nFE
#set eleTag $nStory$nColRow$nFE$eleType; # eleType is 1 or 2 indicating beam or column respectively

# Runs for each story
    for {set a 1} {$a < $nZc} {incr a} {
        set z [lindex $Zcoord $a]
        set nStory 1[expr $a+1]

        # Defines Beams from i=0 to i=end(Xcoord)
```

```
        for {set i 0} {$i < $nXc-1} {incr i} {
            set nColRow [expr $i+1]

            # Defines first node and internal nodes for a column spanning z_j to z_j+1
            for {set deltax 1} {$deltax < $nFE} {incr deltax} {

                set x [expr ([lindex $Xcoord $i])+((1.0*$deltax)/$nFE)*([lindex $Xcoord [expr $i+1]]-[lindex $Xcoord $i])]

            #   node    $secTag                 x-coordinates   z-coordinates   -mass   mDof1   mDof2   mDof3
                node    $nStory$nColRow$deltax  $x              $z              -mass   0.001       0.0     0.0
            #   puts "$x , $z"
                unset x
            }
            unset nColRow
        }
        unset z
        unset nStory
    }

# Runs for each column row
    for {set b 0} {$b < $nXc} {incr b} {
        set x [lindex $Xcoord $b]
        set nColRow [expr $b+1]

        # Defines columns from j=0 to j=end(Zcoord)
        for {set j 0} {$j < $nZc-1} {incr j} {
            set nStory 2[expr $j+1]

            # Defines first node and internal nodes for a column spanning z_j to z_j+1
            for {set deltaz 0} {$deltaz < $nFE} {incr deltaz} {

                set z [expr ([lindex $Zcoord $j])+((1.0*$deltaz)/$nFE)*([lindex $Zcoord [expr $j+1]]-[lindex $Zcoord $j])]

            #   node    $secTag                 x-coordinates   z-coordinates   -mass   mDof1   mDof2   mDof3
```

```
                node    $nStory$nColRow$deltaz  $x             $z             -mass   0.001       0.0     0.0

            #puts "$x , $z"
            unset z
            }
            unset nStory
        }
        # Defines last node that the loop can't produce
        set z [lindex $Zcoord $nZc-1]
        set nStory 2$nZc
        #   node    $secTag                 x-coordinates   z-coordinates   -mass   mDof1   mDof2   mDof3
            node    $nStory${nColRow}0      $x              $z              -mass   0.001       0.0     0.0
        #puts "lastly $x, $z"

        unset x
        unset z
        unset nColRow
        unset nStory
    }

puts ""
puts "...Nodes defined"
puts "      all nodes are massless, have been defined along a grid defined by:"
puts "      z-coordinates $Zcoord"
puts "      x-coordinates $Xcoord"

#Constraints
    fix 2110 1 1 1
    fix 2120 1 1 1
    fix 2130 1 1 1
    fix 2140 1 1 1
    fix 2150 1 1 1
    fix 2160 1 1 1
```

```
puts "...Constraints defined"

##Title:    Node and nodal masses - 2D model of 4 storey 5 bay RC frame
#Author:    Jørgen Rosmo Roven
#Units:     Metric (mm, ton, N, sec)
#############################################################################################

# Input
set Xcoord {0 6000 12000 16500 22500 28500 }; # mm x-coordinates defining x-axis grid lines
set Zcoord {0 3400 6400 9400 12400}; # mm
# The coordinates listed above must be defined as single variables (I think you only need the z1)

set x1 0;       #mm
set x2 6000;    #mm
set x3 12000;   #mm
set x4 16500;   #mm
set x5 22500;   #mm
set x6 28500;   #mm

set z1 0;       #mm
set z2 3400;    #mm
set z3 6400;    #mm
set z4 9400;    #mm
set z5 12400;   #mm

#set nFE 4; # Number of finite elements per member must include .0 but can only be whole numbers

# Script defining nodes
source elementDefinitions/dispBeamCol/dispBeamCol_Nodes.tcl

# Redefining nodes which needs to be assigned mass

set m1tot [expr ((33+25*0.3*0.35)*28500+25*(2*0.45*0.45+4*0.5*0.5)*2700+2*25*0.26*0.3*5016+4*25*0.3*0.35*4966)/9.81/1000];
set m2tot [expr ((33+25*0.3*0.35)*28500+25*(2*0.45*0.45+4*0.5*0.5)*2500+2*25*0.26*0.3*5016+4*25*0.3*0.35*4966)/9.81/1000];
```

```
set m3tot [expr ((33+25*0.3*0.35)*28500+25*(8*0.45*0.45+4*0.5*0.5)*2500/2+2*25*0.26*0.3*5016+4*25*0.3*0.35*4966)/9.↙
81/1000];
set mrooftot [expr ((28.9+25*0.26*0.3)*28500+25*6*0.45*0.45*2500/2+6*25*0.26*0.3*5016)/9.81/1000];

puts "";
puts "Total mass for each storey"; puts "";
puts "Roof level: $mrooftot ton"
puts "3rd storey: $m3tot ton"
puts "2nd storey: $m2tot ton"
puts "1st storey: $m1tot ton";
puts "Total mass: [expr $m1tot+$m2tot+$m3tot+$mrooftot] ton"; puts "";

#   remove node $nodeTag    |   #node   $nodeTag    (ndm $coords)   <-mass  (ndf $MassValues)>
    remove node 2230        ;   node    2230        $x3 $z2         -mass   $m1tot              0.0     0.0
    remove node 2330        ;   node    2330        $x3 $z3         -mass   $m2tot              0.0     0.0
    remove node 2430        ;   node    2430        $x3 $z4         -mass   $m3tot              0.0     0.0
    remove node 2530        ;   node    2530        $x3 $z5         -mass   $mrooftot           0.0     0.0

# Script defining elements
source elementDefinitions/dispBeamCol/dispBeamCol_Elements.tcl
```